Physics Based Iterative Reconstruction for MRI: Compensating and Estimating Field Inhomogeneity and T_2^* Relaxation

by

Bradley P. Sutton

A dissertation submitted in partial fulfillment
of the requirements for the degree of
Doctor of Philosophy
(Biomedical Engineering)
in The University of Michigan
2003

Doctoral Committee:

Assoc. Professor Jeffrey A. Fessler, Co-Chair
Assoc. Professor Douglas C. Noll, Co-Chair
Professor Thomas L. Chenevert
Asst. Professor Thomas E. Nichols

For Mandy

ACKNOWLEDGEMENTS

This thesis is a result of the ideas, hard work, and support of many people. I thank God that He put me in this place at this time with this group of people, the success of this project can be attributed to that alone. First I would like to thank my two advisors. Doug Noll and Jeff Fessler have provided the guidance, wisdom, and practical ideas that drove this project forward and kept me from getting discouraged by GE idiosyncrasies. I would like to thank my other committee members, Tom Nichols and Tom Chenevert for their valuable input on my projects. I would also like to thank the Whitaker Foundation for their support and the travel stipends that allowed me to attend many conferences that stimulated ideas.

I would like to thank the fMRI lab group: Eve Gochis and Keith Newnham who made sure that administration and scan time were never problems, Scott Peltier helped me get started with real data and paved the way for completion of the PhD, Alberto Vazquez who helped with real data, pulse sequences, and computer issues. Valur Olafsson and Sangwoo Lee with whom I had invaluable discussions on image reconstruction and implementation issues, Luis Hernandez who helped with the target application of functional MRI, everyone else at the fMRI lab who made a great working environment: Greg Lee, Kiran Pandey, Kelly Bratic, and Chunyuy Yip. I would also like to thank the members of Dr. Fessler's lab for their insights and for making me understand better so that I could explain it.

Finally, I would like to thank my family who encouraged me along the way. And

I would like to thank my wife, Amanda, for being patient and understanding and for helping me keep things in perspective.

TABLE OF CONTENTS

LIST OF TABLES

Table

LIST OF FIGURES

Figure

CHAPTER 1

Introduction to Image Reconstruction for MRI

1.1 Motivation

Over the last ten years, many advances in hardware, pulse sequence design, and post-processing methods have improved the image quality of magnetic resonance imaging (MRI) experiments. However, the predominant method for *reconstructing* MR images from the acquired measurements has remained relatively unchanged: conjugate phase or other conventional Fourier reconstruction techniques. The conjugate phase method is a modified inverse Fourier transform method that attempts to compensate for phase accrual due to inhomogeneities of the main magnetic field. This classical Fourier-based reconstruction method requires density compensation for non-uniform sampling trajectories and is limited to the case of smoothly-varying field inhomogeneities. Also, some important physical effects have been ignored, such as gradients in the local field intensity across a voxel and relaxation during the signal acquisition. In many applications of MRI, conjugate phase or even conventional Fourier reconstruction is adequate—artifacts caused by unmodeled physical effects are small or easily ignored by the radiologist. However, demand for faster scans and

higher SNR for fMRI and other applications has led to the use of stronger main magnetic fields, nonlinear k-space trajectories (such as spirals and rosettes), and long data readout times. These properties make the MR experiment more sensitive to physical effects from field inhomogeneities and relaxation.

The overall goal of this research is to develop, implement, analyze, and evaluate an iterative, inverse problem approach to the reconstruction of MR images from general types of MR acquisitions using accurate physical models, with the goal of ultimately producing higher quality images. The proposed iterative algorithms take into account T_2^* relaxation and field inhomogeneities, along with the effects of through-voxel gradients of the local magnetic field, leading to images with reduced susceptibility artifacts and reduced signal void regions. The focus is on fMRI applications where gradient-echo, single-shot acquisitions make the scans extremely sensitive to these effects.

In this opening chapter, I describe the basics of MR imaging and image reconstruction, including the effects of field inhomogeneity. In Chapter 2, I introduce our field-corrected iterative image reconstruction for MRI along with methods to speed its computation. Chapter 3 extends the iterative algorithm to include coil sensitivities and subsampled k-space trajectories, allowing for its application to the rapidly growing area of parallel imaging. In Chapter 4 we examine the stability of the iterative reconstruction over a time series of images. This stability is necessary for our target application of functional MRI studies. Chapter 5 gives an extension of the iterative algorithm to the simultaneous estimation of the image, field map,

and T_2^*-relaxation map from an extended (multi-echo) readout. Chapter 6 includes a discussion of the parameterization of the image reconstruction problem to include effects from gradients in the field inhomogeneity distribution across a voxel. Finally, Chapter 7 summarizes our contributions and gives ideas for areas of future work.

1.2 Signal Equation for MR

Atoms with either an odd number of protons or an odd number of neutrons have a nuclear spin angular momentum and can give rise to a measurable signal using MR. For the most part, proton imaging is used because the body contains large amounts of water. In the absence of an applied magnetic field, the spin angular momentum of a proton is randomly oriented. However, when an external magnetic field is applied, a small portion of them tend to align with the magnetic field giving rise to a net magnetic moment, M_o, that is aligned with the applied magnetic field. The equilibrium magnetic moment is determined by a Boltzmann distribution and for protons it is given by (Equation 6.11 in [1]):

$$M_o = \frac{1}{4}\rho_o \frac{\gamma^2 \hbar^2}{kT} B_o, \tag{1.1}$$

where ρ_o is the proton density, γ is the gyromagnetic ratio specific to the nucleus being imaged, $\hbar$ is Planck's constant divided by 2π, k is Boltzmann's constant, T is the absolute temperature, and B_o is the applied magnetic field strength. Values of γ for various nuclei that are typically imaged can be found in Table 1.1. Thus the magnetization is proportional to the field strength and proton density, but inversely proportional to temperature. In an imaging experiment, we are typically trying to

Nucleus	γ **(MHz/T)**	**Abundance in Body**
^{1}H	42.58	88M
^{23}Na	11.27	80mM
^{31}P	17.25	75mM
^{17}O	-5.77	16mM
^{19}F	40.08	4μM

Table 1.1: Gyromagnetic ratios for various nuclei, from Haacke, *et al.* [1].

measure some function of the magnetization of a collection of protons, such as their relative density in a tissue of interest.

1.2.1 One-Dimensional Imaging

If the net magnetization vector is tipped away from the applied field direction into the transverse plane, the magnetization begins to precess around the field at the Larmor frequency, ω_o, given by:

$$\omega_o = \gamma B_o. \tag{1.2}$$

This gives us a basis for imaging proton distributions present in the sample of interest. By applying a spatially dependent magnetic field, the spatial position of protons can be determined from the frequency content of the resulting signal. This is illustrated in Figure 1.1. The simulation object that we will use for this example is shown in panel a. This image shows the density of protons in an object of interest. The applied magnetic field strength is B_o, but a gradient is applied across the one dimension over which we will be imaging, as shown in panel b. of Figure 1.1. This results in a variation of the Larmor frequency corresponding to spatial position. Specifically, if the applied gradient strength is G with units of Tesla/cm and if the applied magnetic field is B_o, then the Larmor frequency of a proton depends on its spatial position as

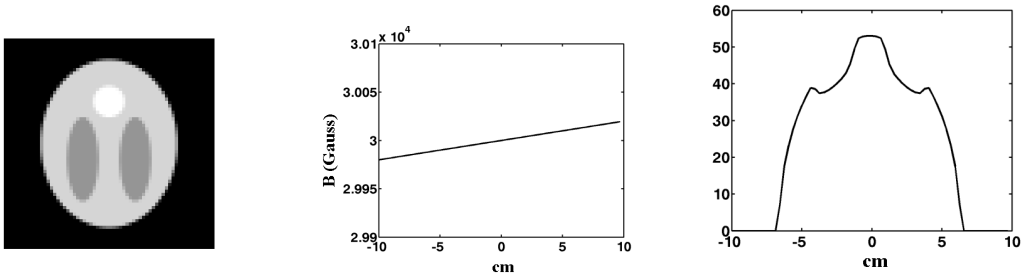

a b c

Figure 1.1: Imaging in MR. a.) Simulation object. b.) Spatially dependent magnetic field. c.) Fourier transform of basebanded signal.

follows:

$$\omega_L(x) = \gamma(B_o + Gx) = \omega_o + \gamma Gx. \tag{1.3}$$

Note that 1 Tesla $= 10^4$Gauss. If we collect samples of the signal over a short period of time, demodulate the signal by ω_o (called basebanding), and take the Fourier Transform to determine the frequency information from the signal, we get the one-dimensional "image" in panel c. of Figure 1.1. A mapping exists between the frequency and the spatial position. If we make $\Delta\omega$ the resulting frequency offset from ω_o, then we can convert to spatial position using (1.3),

$$x = \frac{\Delta\omega}{\gamma G}. \tag{1.4}$$

1.2.2 K-space

For the transition to imaging in two- and three-dimensions, we defer to the concept of k-space. In the previous section, Section 1.2.1, we saw the Fourier transform relationship between the signal and the image in one-dimension. Using k as the Fourier domain variable, the basebanded signal, $s(k)$, is given by,

$$s(k) = \int \rho(x) e^{-i2\pi kx} dx, \tag{1.5}$$

for some position, k, in the frequency domain and some density of protons at position x, $\rho(x)$. Alternatively, we can look at the basebanded phase, $\phi(x)$, of a proton at position x precessing in the transverse plane at a certain time, t, that has been subjected to a time-varying gradient $G(t)$. Integrating Equation (1.3) over time, we get:

$$\phi(t,x) = \gamma \int_0^t G(\tau) x d\tau. \tag{1.6}$$

If we look at the signal resulting from all protons with phase that has accumulated under time-varying gradients, we get,

$$s(t) = \int \rho(x) e^{\gamma \int_0^t G(\tau) x d\tau} dx. \tag{1.7}$$

We can see by comparing Equations (1.5) and (1.7) that,

$$k(t) = \frac{\gamma}{2\pi} \int_0^t G(\tau) d\tau. \tag{1.8}$$

This variable, $k(t)$, can be interpreted as the sampling trajectory in the frequency domain or k-space. For the one-dimensional example of Figure 1.1, the trajectory is simply a straight line with samples spaced by $\frac{\gamma}{2\pi} G \Delta t$, where Δt is our sampling time.

1.2.3 Two- and Three-Dimensional Imaging

In two- and three-dimensional MRI experiments, the basebanded phase of a proton at a position (x, y, z) at time t is given by the addition of the phases due to the gradients in the three principle directions,

$$\begin{aligned} \phi(t,x,y,z) &= \gamma \int_0^t \left(G_x(\tau) x + G_y(\tau) y + G_z(\tau) z \right) d\tau \\ &= \gamma \int_0^t \boldsymbol{G}(\tau) \cdot \boldsymbol{r} d\tau, \end{aligned} \tag{1.9}$$

where $\boldsymbol{G}(t) = (G_x(t), G_y(t), G_z(t))$, *i.e.* gradients of the main magnetic field in the three principle directions, and $\boldsymbol{r} = (x, y, z)$. Therefore, similar to the one-dimensional example in the previous section, samples of the spatial frequency information of the object of interest are obtained by moving around in two- or three-dimensional k-space through the application of gradients. The k-space coordinates, $\boldsymbol{k}(t) = [k_x(t), k_y(t), k_z(t)]$, are given by:

$$k_x(t) = \frac{\gamma}{2\pi}\int_0^t G_x(\tau)d\tau, \quad k_y(t) = \frac{\gamma}{2\pi}\int_0^t G_y(\tau)d\tau, \quad k_z(t) = \frac{\gamma}{2\pi}\int_0^t G_z(\tau)d\tau. \quad (1.10)$$

The complex basebanded signal is given by,

$$s(t) = \int \rho(\boldsymbol{r})e^{-i2\pi\boldsymbol{k}(t)\cdot\boldsymbol{r}}d\boldsymbol{r}. \quad (1.11)$$

There are many options and considerations when designing the k-space trajectory. In a general two-dimensional acquisition called spin-warp, a readout gradient, such as a constant G_x gradient, follows a blipped phase encode gradient, such as a short pulse of G_y. Data acquisition occurs during the application of the readout gradient tracing out a line of constant k_y. By varying the value of k_y during subsequent acquisitions, a rectilinear or Cartesian trajectory is followed in k-space and this trajectory is shown in Figure 1.2a. A train of readout gradients can be separated by small blips in the phase encode direction to decrease the amount of time required to acquire a complete k-space. This is called echo-planar imaging (EPI) and it uses a k-space trajectory similar to that of spin-warp. Other trajectories for acquiring k-space quickly are spirals and rosettes [3], shown in Figure 1.2 in panels b. and c., respectively. These trajectories acquire data while both the time-varying $G_x(t)$ and $G_y(t)$ gradients are

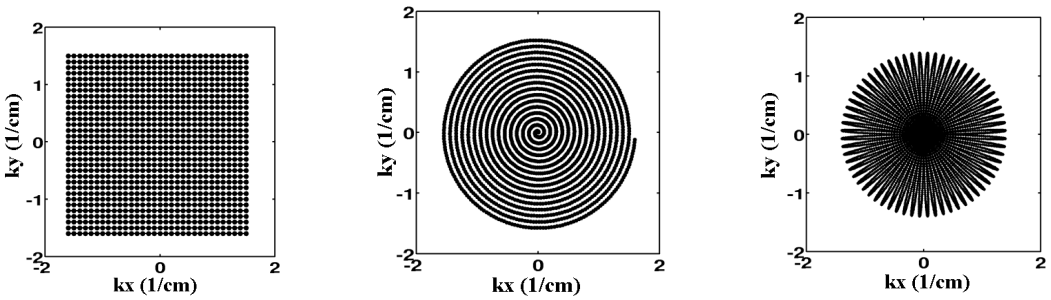

a b c

Figure 1.2: K-space trajectories for two-dimensional imaging. a.) Rectilinear or Cartesian. b.) Spiral. c.) Rosette.

on. Spiral trajectories are often used in functional MRI experiments as they provide a quick and efficient coverage of k-space and are robust to motion and flow effects. The main focus of this work will be for spiral k-space trajectories although the methods developed are applicable to any arbitrary trajectory.

1.3 Fourier Reconstruction

As was the case for the one-dimensional imaging problem, the two- (or three-) dimensional data in k-space are related to the image through a Fourier transform. If the k-space trajectory does not intersect itself, then there is a one-to-one mapping from t to $\boldsymbol{k}$, so that $s(t) = s(\boldsymbol{k}(t))$ and (1.11) becomes:

$$s(\boldsymbol{k}) = \int \rho(\boldsymbol{r}) e^{-i2\pi \boldsymbol{k}(t)\cdot \boldsymbol{r}} d\boldsymbol{r}. \tag{1.12}$$

This form shows the Fourier relation of the expected data to the image. If the k-space trajectory intersects itself, then the calculation of density compensation functions for Fourier reconstruction (described below) becomes more complicated. Note that the iterative methods presented in this thesis do not require density compensation and are able to handle intersecting k-space trajectories.

The Fourier transform relationship in Equation (1.12) is inverted for the image reconstruction problem,

$$\hat{\rho}(\boldsymbol{r}) = \int_K s(\boldsymbol{k}) e^{i2\pi \boldsymbol{k}\cdot\boldsymbol{r}} dA, \tag{1.13}$$

where K denotes that the integration is performed over all of k-space and dA is the differential area element around the point $\boldsymbol{k}$ [4]. If a Cartesian k-space trajectory is used, as shown in panel a. of Figure 1.2, then dA = constant = $d\boldsymbol{k}$ and the reconstruction becomes,

$$\hat{\rho}(\boldsymbol{r}) = \int_K s(\boldsymbol{k}) e^{i2\pi \boldsymbol{k}\cdot\boldsymbol{r}} d\boldsymbol{k}. \tag{1.14}$$

Discretizing this integral, we get:

$$\hat{\rho}(\boldsymbol{r}_n) = \sum_{m=1}^{M} s(\boldsymbol{k}_m) e^{i2\pi \boldsymbol{k}_m\cdot\boldsymbol{r}_n}. \tag{1.15}$$

This equation is evaluated quickly by a two-dimensional fast Fourier transform (FFT).

For the spiral and rosette trajectories shown in Figure 1.2, the sampling density is much higher at the center of k-space than at the edges. If a non-Cartesian k-space trajectory is used, then a change of variables in Equation (1.13) is needed in order to transform the integration variable to a variable on a uniform grid [4]. This will give proper compensation for changes in the sampling density during k-space acquisition. Let (u, v) be variables on a uniform grid representing the acquisition scheme and let T be a transformation such that $(k_x, k_y) = T(u, v) = T(\boldsymbol{u})$. Then using the change of variables, Equation (1.13) is given by:

$$\hat{\rho}(\boldsymbol{r}) = \int_{T^{-1}(K)} s(k_x(\boldsymbol{u}), k_y(\boldsymbol{u})) e^{i2\pi(k_x(\boldsymbol{u})x + k_y(\boldsymbol{u})y)} \left| \frac{\partial(k_x, k_y)}{\partial(u, v)} \right| dudv, \tag{1.16}$$

so that the differential area is given by,

$$dA = \left| \frac{\partial(k_x, k_y)}{\partial(u, v)} \right| dudv. \tag{1.17}$$

The determinant of the Jacobian of the transformation T, $|\partial(k_x, k_y)/\partial(u, v)|$, is proportional to the differential area element in the original coordinates around points which are uniformly spaced in the transformed coordinates, (u, v). This means that the determinant of the Jacobian of the transformation is inversely proportional to the sampling density in the original coordinates. Discretizing Equation (1.16), we get the Fourier-based reconstruction for arbitrary k-space as,

$$\hat{\rho}(\boldsymbol{r}_n) = \sum_{m=1}^{M} w_m s(\boldsymbol{k}(t_m)) e^{i2\pi \boldsymbol{k}(t_m)\cdot \boldsymbol{r}_n}, \tag{1.18}$$

where w_m is the density compensation function evaluated at the sampling points t_m.

1.3.1 Density Compensation

From this point on, the determinant of the Jacobian in Equation (1.17) will be referred to as part of a family of density compensation functions. There is still some discussion on quickly computing optimal density compensation functions for arbitrary k-space trajectories [4–12]. Note that for the iterative image reconstruction method presented in later chapters, this sample density weighting is not needed [13].

Jackson, *et al.* defined an area density function which was the convolution of delta functions at the k-space trajectory locations with a convolution function [5]. In [4], the Jacobian of the determinant between the spiral and Cartesian coordinates is given as,

$$W(t) = \left| \frac{\partial(k_x, k_y)}{\partial(t, \beta)} \right| = \frac{\gamma}{2\pi} \|\boldsymbol{k}(t)\| \|\boldsymbol{G}(t)\| \|\cos(\boldsymbol{G}(t), \boldsymbol{k}(t))\|, \tag{1.19}$$

where β is the parameterization of shot number for multi-shot spiral acquisitions. Meyer *et al.* offer a similar expression in [11].

Pipe and Menon in [8] form an iterative procedure to find the weighting functions by noticing in Equation (1.22) that the image reconstructed from the sampled data will be blurred by convolution with the Fourier Transform of the weighting function. So the iterative update of the weighting function tries to enforce a delta point spread function inside the field of view (FOV) for the Fourier transform of the weighting function. If $\phi(x, y)$ is a function that is non-zero inside the FOV and zero outside it, $\Phi(u, v)$ is its Fourier Transform, and $w(x, y)$ is the Fourier Transform of the weighting coefficients, then we want to esure that,

$$w(x, y)\phi(x, y) = \delta(x, y). \tag{1.20}$$

Convolving both sides of Equation (1.20) with w and expressing in k-space gives their update rule (Equation 14 in [8]),

$$W_{i+1} = \frac{W_i}{W_i \otimes \Phi}, \tag{1.21}$$

where $\otimes$ denotes convolution.

Qian, *et al.* equate the point spread functions (psf) of the images reconstructed from data acquired on a Cartesian grid with the weighted data acquired on an arbitrary grid. They solve for the unknown weights using an iterative method. They term the weights as "same-image weights."

Sedarat and Nishimura in [6] attempt to formulate both gridding reconstruction (described in Section 1.3.2) and a least-squares interpolation (similar to URS described Section 1.3.3) in similar forms. They can then examine the error between

these two methods. Note that least-squares interpolation does not require density compensation functions, but is an iterative and computationally-intensive procedure. The gridding reconstruction does include a density compensation weighting. The optimal weighting coefficients for the gridding reconstruction are determined by minimizing the error between these two methods.

In [12], density compensation functions for arbitrary k-space trajectories are found by dividing up the total area of k-space into Voronoi cells around each sample location. The density compensation factors are then just the inverse of the area of the Voronoi cells. This method is very accurate and simple to apply to arbitrary trajectories. Unless otherwise noted, this weighting is used for all gridding and conjugate phase reconstructions in this thesis.

1.3.2 The Gridding Algorithm

When k-space is sampled on a uniform grid, an FFT can be used to quickly reconstruct the image as noted after Equation (1.15). The computational advantage of the FFT can be used for non-Cartesian k-space trajectories if we first interpolate or grid the data onto a uniform grid and then apply the FFT. Despite low accuracy, simply using bilinear interpolation of the density-compensated data and then applying the FFT gives a reconstruction of the image. Other interpolation schemes have been examined in computerized tomography applications [14–16].

A more accurate and widely used method in MRI is referred to as the gridding algorithm [5, 11]. I will discuss the steps used in the gridding algorithm, but the

entire method is summarized by the following equation [5]:

$$M_c = \{[(M{\cdot}S \cdot W) \otimes C] \cdot R\} \otimes^{-1} C \tag{1.22}$$

where M_c is the data in k-space gridded onto a Cartesian grid, $M{\cdot}S$ is the sampled data on the k-space trajectory, W is the density compensation function, C is the convolution function used for gridding the data, R denotes the Cartesian grid sampling function, and $\otimes$ denotes convolution. There are four main steps to gridding:

1. Multiply the data that is sampled on the k-space trajectory, $M{\cdot}S$ with a density compensation function, W, to account for the unequal sampling of k-space.

2. Convolve the weighted data with a chosen convolution function, C, and resample on a Cartesian grid, R.

3. Apply the two-dimensional FFT to reconstruct an image.

4. Perform deapodization to remove the effect of the convolution function by dividing the result by the Fourier Transform of the convolution function, this is denoted by $\otimes^{-1}C$ in (1.22).

There are a few practical considerations that result in a greatly increased accuracy of the gridding algorithm. When choosing a convolution function, two criteria have been used to evaluate performance, sidelobe energy and roll-off of the interpolator within the field-of-view (FOV). According to Fourier theory, sampling in k-space results in replication of the object in the image domain. By convolving the k-space samples with a convolution function, the resulting image replicates are multiplied

by the FT of the convolution function. If the FT of the convolution function has significant energy that exists outside the FOV, then this energy will be aliased back into the image from the replicates. The other criteria commonly considered is roll-off of the interpolator within the FOV. During the deapodization process, the image is divided by the FT of the convolution function. If the Fourier transform of the convolution function rolls off at the edges of the FOV, this will be compensated by deapodization at the expense of amplifying aliased sidelobe energy occurring at the edges of the FOV. A solution to this problem, as presented by Jackson, *et al.* [5], is to grid the k-space data onto a finer grid. If the grid size is reduced by a factor of two, then the resulting FOV of the image is doubled. This allows a wider frequency response of the convolution function, resulting in reduced sidelobes. This also allows the FT of the convolution function to be more uniform over the desired FOV, with the tapering off occurring mostly in the outer portion of the larger FOV which will be discarded to get back to the original FOV. Jackson, *et al.* also examine various convolution functions with respect to the two criteria mentioned above. They found that the Kaiser-Bessel kernel was simple to compute and worked very well. The optimal parameters for various sizes of the interpolation kernel are given in [5]. A higher accuracy is achieved using a larger kernel and larger oversampling factor, but it is at the expense of a higher computational burden - more samples involved in the convolution and a larger FFT, respectively.

Once the data has been resampled onto a Cartesian grid, we can take advantage of the computational efficiency of the FFT. To remove the effect of the fall-off of

image intensity near the edges of the image, we divide by the Fourier Transform of the convolution function, this is known as deapodization. After deapodization, the reconstructed image is found by truncating the result to the original FOV before upsampling to the finer k-space grid.

1.3.3 Other approaches

Other approaches exist to grid the data from arbitrary k-space trajectories onto a regular grid, notably Uniform ReSampling or URS [17]. URS proceeds by formulating the gridding interpolation problem as the forward problem $Ax = b$, where x is the value of the k-space data on a regular grid, b is the data on the arbitrary trajectory, and A is a matrix of interpolation coefficients, *i.e.* sinc interpolation coefficients. Given the interpolation matrix and the data at the arbitrary k-space locations, the inverse problem is solved by least-squares, *i.e.* computing the pseudo-inverse of A. Once the regularly spaced data, x, is determined, the image is formed by taking the two-dimensional FFT. No density compensation of the data or deapodization of the resulting image is necessary in this case. A variant of this algorithm called Block URS, or BURS, makes the solution more computationally feasible by truncating the interpolation in the rows of A to only the nearest neighbors of each sampling location corresponding to the entries in b.

1.4 Nonidealities in the Imaging Experiment

The relation between the received signal and the object expressed in Equation (1.12) is an ideal case. In reality, tissues possess a property called magnetic susceptibility which alters the effective magnitude of the magnetic field inside the

brain. Figure 5 in [18] shows the distribution of the magnetic field in the head due to susceptibility as calculated from a simulation performed by Truong, *et al.* [18]. As this figure shows, inhomogeneity due to susceptibility differences occurs in regions next to the paranasal sinuses, including the frontal and sphenoid sinuses, and the ear canals, inner ear and mastoid air cells, for example, in the orbital-frontal cortex and inferior temporal lobes. This field inhomogeneity disrupts the careful control of the resonant frequency relation to spatial position expressed in (1.3), which can now be written as,

$$\omega_L(x) = \omega_o + \gamma G x + \Delta\omega_o(x), \tag{1.23}$$

for the one-dimensional case, where $\Delta\omega_o(x)$ is the susceptibility-induced resonant frequency change. For simplicity, we will refer to this magnetic susceptibility or field inhomogeneity effect as $\omega(\boldsymbol{r})$ for the multi-dimensional case. Ignoring this effect in the image reconstruction process leads to geometric distortions (pixel shifts) when Cartesian k-space trajectories are used [19] and it leads to blurring of the image for spiral trajectories [20].

Another effect ignored in the idealized Equation (1.12) that occurs in the gradient echo acquisitions that are typical of functional MRI studies, is relaxation of the signal due to dephasing of the magnetic dipoles within a voxel. This effect is referred to as T_2^*. This decay is due to microscopic field inhomogeneities resulting in a dispersion of resonant frequencies within a voxel. Note that the T_2^*-decay mechanism is important to functional MRI. Changes in the T_2^* decay of a voxel can be related to changes in oxygenation of hemoglobin [21] and this is referred to as the Blood Oxygenation

Level Dependent, or BOLD, effect. Ignoring the effect of T_2^* during the reconstruction leads to broadening of the point spread function of the reconstruction algorithm.

A more accurate model of the complex baseband signal during and MRI experiment is given by [22],

$$\begin{aligned} y(t) &= s(t) + \varepsilon(t) \\ &= \int \tilde{f}(\boldsymbol{r}) c(\boldsymbol{r}) e^{-i\omega(\boldsymbol{r})(t+T_E)} e^{-R_2^*(\boldsymbol{r})(t+T_E)} e^{-i2\pi(\boldsymbol{k}(t)\cdot\boldsymbol{r})} d\boldsymbol{r} + \varepsilon(t), \end{aligned} \tag{1.24}$$

where $y(t)$ is the complex baseband signal at time t during the readout in the presence of noise $\varepsilon(t)$, T_E is the echo time, $\tilde{f}(\boldsymbol{r})$ is a continuous function of the object's transverse magnetization at location $\boldsymbol{r}$ immediately following the spin preparation step, $c(\boldsymbol{r})$ is the spatial sensitivity of the receiver coil, $\omega(\boldsymbol{r})$ is the field inhomogeneity present at $\boldsymbol{r}$, and $R_2^*(\boldsymbol{r})$ is the $1/T_2^*(\boldsymbol{r})$ relaxation. The noise, $\varepsilon(t)$, is mostly white Gaussian noise [1] along with physiological noise induced by respiration and cardiac cycles. Some post-processing methods exist to significantly reduce the physiological component from the noise [23]. If we absorb the coil sensitivity and the decay and field inhomogeneity effects at the echo time into the object to be reconstructed, *i.e.* $f(\boldsymbol{r}) = \tilde{f}(\boldsymbol{r}) c(\boldsymbol{r}) e^{-i\omega(\boldsymbol{r})T_E} e^{-R_2^*(\boldsymbol{r})T_E}$, we can express Equation (1.24) as,

$$y(t) = \int f(\boldsymbol{r}) e^{-i\omega(\boldsymbol{r})t} e^{-R_2^*(\boldsymbol{r})t} e^{-i2\pi(\boldsymbol{k}(t)\cdot\boldsymbol{r})} d\boldsymbol{r} + \varepsilon(t). \tag{1.25}$$

The goal in an imaging experiment is to reconstruct $f(\boldsymbol{r})$ from the noisy samples $y(t_m)$ for $m = 1, \ldots, M$, where M is the number of samples acquired. If we can accurately reconstruct $f(\boldsymbol{r})$, we could in principle recover $\tilde{f}(\boldsymbol{r})$ from knowledge of the coil sensitivity, field inhomogeneity, and T_2^* relaxation.

1.4.1 Standard Field-Corrected Reconstruction

When the magnetic field inhomogeneity term is included in Equation (1.25) and relaxation is ignored, we get,

$$s(t) = \int f(\boldsymbol{r}) e^{-i\omega(\boldsymbol{r})t} e^{-i2\pi(\boldsymbol{k}(t)\cdot\boldsymbol{r})} d\boldsymbol{r}. \tag{1.26}$$

Many image reconstruction methods have been proposed to correct for the image distortions caused by field inhomogeneities. If fast Cartesian trajectories, such as EPI, are used, a common and effective way to correct for the geometric distortions caused by field inhomogeneities is by a pixel-shift method [19, 24–26]. For this method, a map of the off-resonance frequencies due to field inhomogeneity is converted into a pixel shift map by dividing by the frequency content per pixel. This shift is then applied to the image in the phase encode direction. For EPI trajectories, the timing of the acquisition is much slower in the phase encode direction compared to the readout direction, so phase accumulation due to field inhomogeneity is dominant in this direction. The pixel-shift method works well for smoothly-varying field inhomogeneities such that the point spread function (psf) of neighboring pixels are not shifted enough to overlap. When non-Cartesian trajectories are used, there are three main field-inhomogeneity correction schemes: SPHERE, auto-focusing, and conjugate phase. As described in [27], Simulated PHase Evolution REwinding or SPHERE begins with a Fourier reconstruction of the data resulting in a distorted image. Using an estimate of the field inhomogeneity map that is also distorted, this distorted image is used to simulate k-space data using (1.26), except that the negative of the field map is used in order to rewind the phase accumulation due to field

inhomogeneities. This resulting k-space is reconstructed to give an estimate of the undistorted image. In the auto-focusing method of [28], an image is constructed by choosing the resonant frequency for each pixel based on a measure of blurriness of the reconstructed image. The sharpness of the image is chosen by minimizing a non-linear function of the imaginary component of the image after removing a low-pass filtered phase, according to,

$$\int\int |Imag\{I(x,y;\Delta\omega_E)\}|^{\alpha} dxdy = 0 \tag{1.27}$$

where $I(x,y;\Delta\omega_E)$ is the image reconstructed with an inhomogeneity offset frequency of $\Delta\omega_E$ and the integration is performed in a local neighborhood in the image. A method to speed up the algorithm and make it less vulnerable to noise is presented in [29]. In that paper, auto-focusing is done in two steps. The first step provides a coarse use of auto-focus over the whole image using large blocks as the local neighborhood. The second step limits the deviation of the off-resonant frequency of smaller sub-blocks of the image to a range around that estimated for the larger block. Finally, the most prevalent method for field-inhomogeneity correction for non-Cartesian trajectories is the conjugate phase method. The conjugate phase method seeks to compensate for the phase accrual at each time point due to the off-resonance [30–32]. The conjugate phase reconstruction is given by,

$$\hat{f}(\boldsymbol{r}_n) = \sum_{m=1}^{M} w_m s(t_m) e^{i\omega(\boldsymbol{r}_n)t_m} e^{i2\pi(\boldsymbol{k}(t_m)\cdot\boldsymbol{r}_n)}. \tag{1.28}$$

Time-segmented and frequency-segmented approximations exist for this method to allow it to utilize the computational speed of gridding reconstruction [30, 32]. This

method, like the other noniterative methods discussed here, relies on the assumption of a smoothly-varying field map and fails in regions where this assumption is violated [13, 30, 33].

Schomberg [31] provides a rigorous analysis of the family of conjugate-phase methods for off-resonance correction of MR images, and concludes that segmented conjugate-phase methods are preferable to SPHERE methods [27], at least for spiral imaging. Therefore, we focus on comparing our proposed iterative methods to the conjugate-phase method as the *de facto* standard for non-iterative off-resonance correction for non-Cartesian k-space trajectories.

Although field inhomogeneity was mentioned above along with methods to partially correct for it, this continues to be a significant problem in gradient echo MR experiments. Image distortions from field inhomogeneities are worse in high fields and with long readout times, common properties desired for good functional contrast and temporal resolution in fMRI. The corrections mentioned above are limited to smoothly varying field maps and are zeroth-order corrections. Distributions of resonant frequencies across a voxel, in-plane or through the slice, cause image distortions and dephasing (signal loss) in an MR experiment. Some work has been done on modifying conjugate phase reconstructions to account for the first-order effect of in-plane dephasing [34], but this eliminates some of the computational advantage of the noniterative method while still being limited to smoothly-varying field inhomogeneities.

1.4.2 Measuring the Field Map

The conjugate phase method relies on the accurate measurement of a field map, a map of the spatial distribution off-resonance frequency due to susceptibility-induced field inhomogeneities. Field inhomogeneity maps are typically obtained by acquiring a gradient-echo image at two slightly different echo times and dividing the phase difference in the reconstructed images by the difference in echo times [2]. This is illustrated graphically in Figure 1.3. The difference in phase of a pixel at echo time TE_1 vs TE_2 is attributed to off-resonance from field inhomogeneity. Dividing this phase difference by the difference in echo times gives an estimate of the field map. If $I_1(\boldsymbol{r})$ is the image at an echo time of $T_E + \tau$ and $I_2(\boldsymbol{r})$ is an image obtained at an echo time of T_E, then an estimate of the field inhomogeneity is given by,

$$\hat{\omega}(\boldsymbol{r}) = -\frac{\angle(I_1(\boldsymbol{r})) - \angle(I_2(\boldsymbol{r}))}{\tau}, \tag{1.29}$$

where $\hat{\omega}(\boldsymbol{r})$ is given in rad/sec and $\angle I(\boldsymbol{r})$ indicates the phase angle of the complex image $I(\boldsymbol{r})$. To avoid problems with 2π phase wraps introduced during the subtraction of the phases, in practice we first compute an intermediate image,

$$I_c(\boldsymbol{r}) = I_1(\boldsymbol{r}) I_2^*(\boldsymbol{r}), \tag{1.30}$$

where * indicates that the complex conjugate of the image $I_2(\boldsymbol{r})$ is used. Then the field map estimate is formed by,

$$\hat{\omega}(\boldsymbol{r}) = -\frac{\angle I_c(\boldsymbol{r})}{\tau}. \tag{1.31}$$

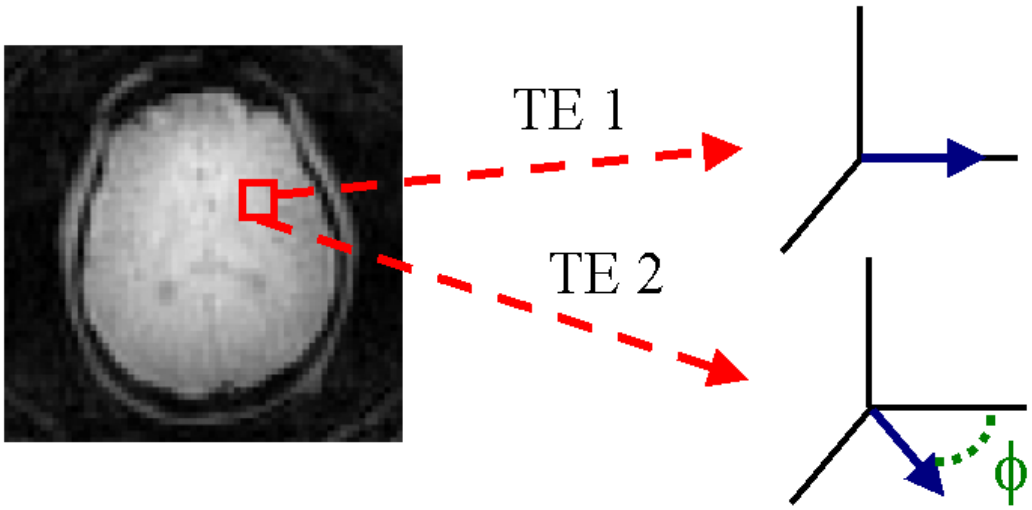

Figure 1.3: Standard field map estimation using the method of [2] proceeds by acquiring two images at two slightly different echo times and examining the extra phase accrual due to the field inhomogeneity.

1.5 Application to functional imaging

Functional MRI (fMRI) relies on encoding task information from regions of the brain in modulations of the magnitude of reconstructed, T_2^*-weighted images [21]. The contrast is developed due to the BOLD response, *i.e.* changes in blood oxygenation levels lead to changes in T_2^*. Long acquisition scans at high field strengths are more sensitive to the effects of changes in T_2^*, but these scan parameters make the acquisitions more sensitive to artifacts from field inhomogeneity. In functional brain imaging, considerable scientific effort is devoted to study design, data acquisition, and statistical data analysis. The image formation step is equally important to the success of an fMRI study. Since contemporary fMRI studies are often investigating high-level cognitive tasks with very low signal levels, physical effects that are

left uncorrected by the conventional Fourier-based reconstruction methods may be particularly important to address. The methods developed here have been mainly applied to fMRI scans using spiral trajectories, but the results should extend to many other acquisition schemes and applications.

CHAPTER 2

Iterative Image Reconstruction[1]

As discussed in the previous chapter, non-iterative, Fourier-based methods exist to compensate for field inhomogeneity artifacts but they are limited to smoothly-varying field inhomogeneities. Regions of the brain near air/tissue interfaces, such as those above the frontal sinuses, have field distributions that violate this assumption. A natural alternative to Fourier-based reconstruction is to pose the reconstruction problem as a statistical estimation inverse problem, where the object's transverse magnetization is represented as a (large) parameter vector of unknown voxel values, and the goal is to find the voxel values that "best fit" the acquired measurements (the MR signal values). Here, "best" is determined by both a physical model and a statistical model. The statistics of MR measurements are well described by (complex) additive white Gaussian noise so a **least-squares** criterion is appropriate (in the maximum likelihood sense) as the measure of best fit. In fMRI one also observes "physiological noise" that is not white, but methods to remove these effects in k-space, *i.e.* before image reconstruction begins, are given in the literature, for an example see [23]. For the physical model, we can return to the fundamental equation

[1] This chapter based primarily on work found in [13, 35]

of MR and the signal equation and include all physical effects that are relevant to the particular imaging situation, including field inhomogeneities and relaxation effects. The primary disadvantage of a physics-based reconstruction method is that generally an **iterative algorithm** is required to find the best fit image, and each iteration requires more computation than just an FFT or gridding. Unlike standard reconstruction schemes that directly map the k-space data to a reconstructed image, (we will call this a back-projector), most iterative reconstruction methods require a forward-projector (given an estimate of the object and field map, form k-space data) as well as the adjoint of the forward projector. Model-based iterative reconstruction methods have the potential to account for field inhomogeneities that violate the smoothly-varying assumption and do not require the use of a density compensation function.

There are a few occurances of iterative reconstruction in the literature. Munger *et al.* [36] reported that iterative conjugate-gradient methods based on Fourier reconstructed echo-planar images outperform the conjugate-phase approach. Their sparsified system model is specific to Cartesian trajectories like echo-planar, whereas the conjugate gradient (CG) approach considered here is applicable to any trajectory. Man *et al.* [37] described an iterative algorithm to remove the residual blur left over after conjugate phase reconstruction in regions with rapidly varying inhomogeneity. The iterative reconstruction algorithm proposed by Harshbarger and Twieg [33] was shown to provide significant improvements in image quality over noniterative methods even for field maps with discontinuities. Their method also can be used in an

extended form to estimate more accurate field maps.

Interest in iterative reconstruction methods has increased recently due to its utility in multiple coil non-Cartesian k-space sensitivity encoding (SENSE) problems [38]. Due to the complex aliasing pattern associated with undersampling k-space trajectories such as spirals, iterative methods that include coil sensitivity patterns in the projectors are necessary to reconstruct artifact-free images in practice [38]. In [39], a method was presented to speed iterative SENSE reconstruction. This method, however, was not analyzed for accuracy and lacked field inhomogeneity correction. We discuss the application of our method to SENSE in Chapter 3.

In this chapter, I will begin with a short background of iterative methods giving some references for the main machinery used in this work. Then, I will discuss my implementation of the iterative reconstruction algorithm in Section 2.2. Then I will discuss methods to speedup the iterative image reconstruction algorithm. In Section 2.3.1, I will discuss some implementation issues related to initialization of the algorithm and preconditioning. In Section 2.3.2 and 2.3.3, I will give the derivation and results for two methods we developed to significantly speedup the iterative image reconstruction process, the non-uniform fast Fourier Transform [35] and a min-max optimal temporal interpolation scheme [13], respectively.

2.1 Iterative methods

Iterative methods are used in linear algebra applications for finding the minimum of a function. For the image reconstruction problem, we are usually trying to find the discrete image $\boldsymbol{x}$ that best fits the sampled data $\boldsymbol{y}$. If the data is linearly related

to the image or object, then the equation relating the two can be written as

$$\boldsymbol{y} = \boldsymbol{A}\boldsymbol{x}, \tag{2.1}$$

where $\boldsymbol{A}$ is the system matrix containing information about the signal formation process. Since $\boldsymbol{A}^{\star}\boldsymbol{A}$ is Hermitian symmetric and positive definite, where * denotes complex conjugate transpose, minimization of the following quadratic form yields the solution to Equation (2.1),

$$\Phi(\boldsymbol{x}) = \|\boldsymbol{y} - \boldsymbol{A}\boldsymbol{x}\|^2. \tag{2.2}$$

Actually the equation corresponding to this quadratic form is given by [40],

$$\boldsymbol{A}^{\star}\boldsymbol{y} = \boldsymbol{A}^{\star}\boldsymbol{A}\boldsymbol{x}. \tag{2.3}$$

Minimization could proceed by finding the gradient of the function with respect to the unknown $\boldsymbol{x}$ at the n^{th} iterative step of the estimate of $\boldsymbol{x}$, $\boldsymbol{x}_n$. The estimate of $\boldsymbol{x}$ is updated to $\boldsymbol{x}_{n+1}$ by stepping a certain distance along this gradient. This method is referred to as a gradient descent. If a search for the minimum is performed along the line passing through the current estimate, $\boldsymbol{x}_n$, along the direction of the gradient, then the method is called steepest descent. The conjugate gradient method ensures that the step size taken in a certain step direction is large enough such that the algorithm will never have to step in that direction again. To perform such a feat, we must ensure that the error in our estimate is orthogonal to the step direction after the step has been taken. Since we do not know the true solution and hence do not know the error in our estimate, we instead enforce the error and the step direction be $\boldsymbol{A}$-orthogonal, or conjugate through the system matrix $\boldsymbol{A}$. For a problem of size

N, the conjugate gradient method converges in N steps, although a much smaller number of steps is usually performed. The conjugate gradient method is a powerful minimization routine for linear problems and is used extensively in this work. For the nonlinear estimation problems, such as the joint estimation of image and field map in Chapter 5, a steepest descent method is employed. Faster convergence rates may be possible using truncated Newton's methods [41], other Quasi-Newton methods, or linearization of the problem. A couple of good references on the steepest descent and conjugate gradient algorithms and their implementations are [40, 42].

2.2 Iterative Reconstruction Algorithm for MRI

In MRI, ignoring relaxation effects, the signal equation is given by Equation (1.26) and repeated here,

$$s(t) = \int f(\boldsymbol{r}) e^{-i\omega(\boldsymbol{r})t} e^{-i2\pi(\boldsymbol{k}(t)\cdot\boldsymbol{r})} d\boldsymbol{r}. \tag{2.4}$$

Recall that in an MR experiment, the measurements are noisy samples of this signal,

$$y_i = s(t_i) + \varepsilon_i, \quad i = 1, \ldots, M. \tag{2.5}$$

The image reconstruction problem is to reconstruct $f(\boldsymbol{r})$ from these noisy samples.

The combination of Equations (2.4) and (2.5) form a continuous-to-discrete (CD) mapping. This is clearly an ill-posed problem since there is an infinite collection of solutions, $f(\boldsymbol{r})$, that exactly match the data $\boldsymbol{y} = (y_1, \ldots, y_M)$. In [43], the pseudoinverse of this CD mapping was investigated for minimum-norm least-squares image reconstruction without field-correction. Although their approach was computationally intensive, the pseudoinverse calculation was object-independent and could be

performed once for a given trajectory. However, in the case of field-corrected imaging, the CD mapping is object-dependent because of the specific field map of the slice of interest. This prohibits precalculation of the SVD of the CD operator, so we seek more practical methods.

Instead of finding the pseudoinverse of the CD mapping, we restrict the number of unknowns to be estimated by parameterizing the object and field map in terms of basis functions, $\phi(r)$, assuming that

$$\begin{aligned} f(\boldsymbol{r}) &\approx \sum_{n=0}^{N-1} f_n \phi_1(\boldsymbol{r} - \boldsymbol{r}_n) \\ \omega(\boldsymbol{r}) &\approx \sum_{n=0}^{N-1} \omega_n \phi_2(\boldsymbol{r} - \boldsymbol{r}_n). \end{aligned} \tag{2.6}$$

For this section, we will use the voxel indicator function

$\phi_1(\boldsymbol{r}) = \phi_2(\boldsymbol{r}) = \text{rect}(r_1/\Delta_1) \cdots \text{rect}(r_P/\Delta_P)$ for the P-dimensional problem. This choice is somewhat natural for display devices that use square areas of nearly constant luminance. However, this parameterization does not model within-voxel field gradients. Triangle basis functions would allow us to model first order gradients of the field map and voxel intensities, which could help reduce within-voxel susceptibility effects. Regardless of what basis one chooses, Equation (2.6) is only an approximation and we explore other choices in Chapter 6. Substituting Equation (2.6) in Equation (2.4) yields

$$s(t) \approx \Phi(\boldsymbol{k}(t)) \sum_{n=0}^{N-1} f_n e^{-i\omega_n t} e^{-i2\pi(\boldsymbol{k}(t)\cdot\boldsymbol{r}_n)}, \tag{2.7}$$

where $\Phi(\boldsymbol{u})$ denotes the Fourier Transform of $\phi(\boldsymbol{r})$, *i.e.* $\Phi(\boldsymbol{u}) = \text{sinc}(u_1) \cdots \text{sinc}(u_p)$.

We express the noisy measured samples of this signal in matrix-vector form as follows

$$\boldsymbol{y} = \boldsymbol{A}\boldsymbol{f} + \boldsymbol{\varepsilon}, \tag{2.8}$$

where $\boldsymbol{f} = (f_0, \ldots, f_{N-1})$ and the elements of the $M \times N$ matrix $\boldsymbol{A}$ are

$$a_{i,j} = \Phi(\boldsymbol{k}(t_i))e^{-i\omega_j t_i}e^{-i2\pi\boldsymbol{k}(t_i)\cdot\boldsymbol{r}_j}. \tag{2.9}$$

In the discrete-to-discrete formulation Equation (2.8), our goal is to estimate the image $\boldsymbol{f}$ from the k-space data $\boldsymbol{y}$, accounting for the statistics of the noise $\boldsymbol{\varepsilon}$. This will still be an ill-posed problem if $N > M$, and is usually ill-conditioned even if $N \leq M$ for non-Cartesian trajectories.

Since the dominant noise in MRI is white Gaussian [1], we estimate $\boldsymbol{f}$ by minimizing the following penalized least-squares cost function,

$$\begin{aligned} \Psi(\boldsymbol{f}) &= \frac{1}{2}\|\boldsymbol{y} - \boldsymbol{A}\boldsymbol{f}\|^2 + \beta R(\boldsymbol{f}) \qquad \text{so that,} \\ \hat{\boldsymbol{f}} &= \arg\min_{\boldsymbol{f}} \Psi(\boldsymbol{f}). \end{aligned} \tag{2.10}$$

The second term in the equation for $\Psi(\boldsymbol{f})$ is a regularization function, $R(\boldsymbol{f})$, that penalizes the roughness of the estimated image. This regularization can decrease the condition number of the image reconstruction problem and, therefore, speed convergence. We choose the parameter β by examining the point spread function of the reconstructed image [44], preferably by choosing β small enough to not significantly degrade the spatial resolution relative to the natural resolution associated with the k-space trajectory.

The least-squares cost function used here is appropriate for Gaussian measurement noise. If non-Gaussian error "spikes" are present, then one could use a non-

quadratic cost function to provide robustness to those outliers [45], at the expense of increased computation. Alternatively, one could use other methods to detect those spikes, *e.g.*, [46], then exclude the corresponding measurement samples from the iterative reconstruction process; no "interpolation" of samples is needed.

We apply the iterative conjugate gradient (CG) algorithm for minimization of Equation (2.10). The algorithm is given below for reference. For simplicity, we have used quadratic regularization: $R(\boldsymbol{f}) = \frac{1}{2}\|\boldsymbol{C}\boldsymbol{f}\|^2$ for a matrix $\boldsymbol{C}$ that takes differences between neighboring pixels. The algorithm may also include a data weighting matrix $\boldsymbol{W}$ for performing weighted least squares, *i.e.* replace $\|\cdot\|^2$ with $\|\cdot\|^2_{\boldsymbol{W}}$ in Equation (2.10). One can also include a preconditioning matrix $\boldsymbol{M}$ to speed convergence of the CG algorithm. Section 2.3.1 discusses the weighting and preconditioner matrices in more detail. In the algorithm below, $\boldsymbol{g}_{new}$ denotes the negative gradient of $\Psi(\boldsymbol{f})$ from Equation (2.10), $\boldsymbol{r}$ is the residual, $\boldsymbol{d}$ denotes the step direction, and α denotes the step size. The algorithm is started with an initial estimate of the image, $\boldsymbol{f} = \boldsymbol{f}_0$. Section 2.3.1 discusses the choice of this initial estimate.

CG Algorithm

Initialize

$$\boldsymbol{r} = \boldsymbol{y} - \boldsymbol{A}\boldsymbol{f}_0 \qquad \text{(residual)}$$

Iteration Steps

$$\begin{aligned}
\boldsymbol{g}_{new} &= \boldsymbol{A}^\star \boldsymbol{W}\boldsymbol{r} - \beta \boldsymbol{C}^\star \boldsymbol{C}\boldsymbol{f}_n \\
\gamma &= \begin{cases} 0 & \text{1st iteration} \\ \frac{\boldsymbol{g}_{new}{}^\star \boldsymbol{M}\boldsymbol{g}_{new}}{\boldsymbol{g}_{old}{}^\star \boldsymbol{M}\boldsymbol{g}_{old}} & \text{else} \end{cases} \\
\boldsymbol{d} &:= \boldsymbol{M}\boldsymbol{g}_{new} + \gamma \boldsymbol{d} \\
\boldsymbol{q} &= \boldsymbol{A}\boldsymbol{d} \\
\alpha &= \frac{\boldsymbol{d}^\star \boldsymbol{g}_{new}}{\boldsymbol{q}^\star \boldsymbol{W}\boldsymbol{q} + \beta \boldsymbol{d}^\star \boldsymbol{C}^\star \boldsymbol{C}\boldsymbol{d}} \\
\boldsymbol{f}_{n+1} &= \boldsymbol{f}_n + \alpha \boldsymbol{d} \qquad \text{(update image)} \\
\boldsymbol{r} &:= \boldsymbol{r} - \alpha \boldsymbol{q} \qquad \text{(update residual)} \\
\boldsymbol{g}_{old} &= \boldsymbol{g}_{new}
\end{aligned}$$

The dominant computation in each iteration of the CG algorithm is computing $\boldsymbol{A}\boldsymbol{d}$ and $\boldsymbol{A}^\star \boldsymbol{r}$, where the superscript * denotes complex conjugate transpose. Computing $\boldsymbol{A}\boldsymbol{f}$ corresponds to evaluating Equation (2.7). For Cartesian k-space trajectories, one can evaluate Equation (2.7) quickly via the Fast Fourier Transform (FFT) if the field inhomogeneity is ignored. However, for non-Cartesian k-space trajectories (spirals, etc.) direct evaluation of Equation (2.7) is very time consuming. When field inhomogeneity is ignored, a non-uniform fast Fourier Transform (NUFFT) can be used to rapidly and accurately evaluate the discrete signal equation (2.7) even for

non-Cartesian trajectories. Our development of the NUFFT will be described in Section 2.3.2. However, the NUFFT method is not directly applicable when the field inhomogeneity is included because Equation (2.4) is not a Fourier transform integral. We circumvent this problem by approximating Equation (2.4) by a time segmented version, similar to [30], and derive a min-max optimal temporal interpolator. This allows the use of the NUFFT to compute Equation (2.7) rapidly and accurately.

2.3 Speedups

The principal drawback of iterative reconstruction methods has been computation time, with reported values of computation time per iteration ranging up to eight minutes [33]. Along with an efficient implementation, we have developed two methods to speed computation of the iterative image reconstruction algorithm, the non-uniform fast Fourier Transform (NUFFT) and a min-max optimal interpolator for time segmentation.

2.3.1 Speeding Convergence of the CG Algorithm

It has been suggested that a weighted-least squares approach be used to speed convergence of the CG algorithm for iterative MR image reconstruction and that the weights be the coefficients of the sampling density compensation function [39]. However, there has been some discussion on how to calculate optimal density compensation factors [6–10] and the iterative image reconstruction algorithm does not require and is not dependent upon these weights if an unweighted (*i.e.* weighting is unity) least squares approach is used instead. Also, assuming the noise in MRI is white Gaussian, using *nonuniform* weighting would be suboptimal statistically ac-

cording to the Gauss-Markov Theorem. Using nonuniform weighting may appear to provide faster convergence in the initial steps of the algorithm for some choices of initial image, but would prevent convergence to the minimum variance solution. Although, Pruessmann *et al.* [39] state that the SNR penalty is negligible when the density compensation function is used as the weights, we will next discuss how to benefit from this approach without risking any SNR.

Consider the CG algorithm in (2.11) when an initial estimate of the image of zeros is used: $\boldsymbol{f}_0 = \mathbf{0}$. Then the first iteration gives,

$$\boldsymbol{f}_1 = \alpha \boldsymbol{A}^\star \boldsymbol{W} \boldsymbol{y}. \tag{2.11}$$

If the data weighting matrix $\boldsymbol{W}$ were just the identity matrix, then this first iteration would simply give the conjugate phase reconstruction without density compensation. If $\boldsymbol{W}$ were instead equal to the density compensation factors, then the first iteration yields a density-compensated conjugate phase reconstruction. Therefore, rather than using an inappropriately weighted CG algorithm, we use the conjugate phase image (reconstructed via a fast, density-compensated, time-segmented approach) as the initial estimate, $\boldsymbol{f}_0$. As noted in [47], initializing with a good density-compensated conjugate phase image ensures that subsequent iterations will improve on this initial guess.

Convergence of iterative algorithms can be accelerated by the use of an appropriate preconditioner, *e.g.*, $\boldsymbol{M}$ in (2.11). Circulant preconditioners have been shown to be effective in shift-invariant problems in tomographic imaging [48]. These preconditioners attempt to undo the blurring induced by applying the forward projec-

tor and its adjoint. A circulant preconditioner should be particularly helpful for MR reconstruction with small off-resonance effects, where the point spread function (PSF) is nearly shift invariant, but may also be of some benefit in regions of higher off-resonance effects. Our results to date with circulant preconditioners have been inconclusive. Preconditioners have also been designed for shift-variant problems [49] and such methods will be investigated for MRI in our future work.

2.3.2 Non-Uniform Fast Fourier Transform (NUFFT)

For Cartesian k-space trajectories, one can evaluate Equation (2.7) quickly via the Fast Fourier Transform (FFT) if the field inhomogeneity and T_2^* relaxation are ignored. However, for non-Cartesian k-space trajectories (spirals, etc.) direct evaluation of Equation (2.7) is very time consuming. When field inhomogeneity is ignored, a family of fast, interpolation methods have been presented to perform the Fourier Transform of nonequally spaced data [50–58]. These methods are called non-uniform Fast Fourier Transforms (NUFFT) and have been applied to MRI data with spiral k-space trajectories [59, 60].

The MR reconstruction problem is closely related to the problem of reconstructing a band-limited signal from nonuniform samples. Strohmer argued compellingly for using trigonometric polynomials (complex exponentials) for finite-dimensional approximations in such problems, and proposed to use an iterative conjugate gradient reconstruction method with the NUFFT approach of [52] at its core [61, 62]. In the MR context, this is essentially equivalent to the finite basis expansion we use in Equation (2.6). In [39], an NUFFT-like algorithm, referred to as 'reverse gridding,'

was applied in combination with the CG algorithm to speed up SENSE image reconstructions. In [59, 60], NUFFT methods were applied to iterative reconstruction of spiral MRI acquisitions. These NUFFT methods have reduced the computation time per iteration to that of noniterative reconstruction methods.

Derivation of the NUFFT

We developed a min-max optimal interpolation for the N-dimensional NUFFT which has a tradeoff between computation time and accuracy [35,60,63]. Our method is easily generalized to N-dimensions, but I will give an overview of the 1D derivation here. The Fourier Transform (FT) of a set of equally spaced signal samples, x_n, possibly weighted by scaling factors s_n, at a set of frequency locations, ω_m, is given by

$$X(\omega_m) = \sum_{n=0}^{N-1} s_n x_n e^{-i\omega_m n}, \quad m = 1, \ldots, M. \tag{2.12}$$

For now we will use unity scaling factors, *i.e.* $s_n = 1, n = 0, \ldots, N-1$. Later in this section we will look at using spatially-varying scaling factors to reduce the interpolation error. If the ω_m's are equally spaced, then Equation (2.12) can be evaluated using an FFT. The NUFFT methods proceed by first calculating an upsampled FFT and then interpolating to find the values of the FT at the nonuniform frequency locations. The upsampled FFT of $\boldsymbol{x}$, $\boldsymbol{Y}$, is given by,

$$Y_k = \sum_{n=0}^{N-1} x_n e^{-i\gamma kn}, \quad k = 0, \ldots, K-1, \tag{2.13}$$

where $\gamma = 2\pi/K$ is the fundamental frequency of the K-point discrete Fourier transform and $K > N$, usually $K = 2N$ or $K = 3N$. The approximation of the FT values

at the nonuniform frequency locations occurs by interpolation over Y_k,

$$\hat{X}(\omega_m) = \sum_{k=0}^{K-1} v_{m,k}^* Y_k, \tag{2.14}$$

where the $v_{m,k}$'s denote the interpolation coefficients, "*" denotes complex conjugate. The problem remains to choose the $\boldsymbol{v}_m = (v_{m,1}, \ldots, v_{m,K})$. In order to reduce computation over the slow evaluation of the FT, we restrict the number of coefficients of the interpolation to that of the J nearest neighbors on the oversampled grid to the nonuniform sampling location. The integer offset, k_m, is used to index the first sample of the J nearest neighbors and is given by:

$$k_m = \begin{cases} (\arg\min_{k\in\mathbb{Z}} \|\omega - \gamma k\|) - \frac{J+1}{2}, & J \text{ odd} \\ (\max\{k\in\mathbb{Z} : \omega \geq \gamma k\}) - \frac{J}{2}, & J \text{ even.} \end{cases} \tag{2.15}$$

Let $u_j(\omega_m)$, for $j = 1, \ldots, J$, be the J possibly nonzero entries of $\boldsymbol{v}_m$. Then the interpolation in Equation (2.14) becomes,

$$\hat{X}(\omega_m) = \sum_{j=1}^{J} Y_{k_m+j} u_j^*(\omega_m). \tag{2.16}$$

We use a min-max criteria to find the optimal interpolation coefficients, $\boldsymbol{u}(\omega_m) = u_1(\omega_m), \ldots, u_J(\omega_m)$. In this framework, we find the interpolation coefficients that minimize the maximum error over all signals $\boldsymbol{x}$ of unit norm, *i.e.*

$$\min_{\boldsymbol{u}(\omega)\in\mathbb{C}^J} \max_{\boldsymbol{x}\in\mathbb{C}^N:\|\boldsymbol{x}\|=1} |\hat{X}(\omega) - X(\omega)|. \tag{2.17}$$

Looking at the error,

$$\begin{aligned} |\hat{X}(\omega) - X(\omega)| &= \left| \sum_{j=1}^{J} Y_{k_m+j} u_j^*(\omega_m) - X(\omega_m) \right| \\ &= \sum_{j=1}^{J} u_j^*(\omega_m) \left[\sum_{n=0}^{N-1} x_n e^{-i\gamma(k_m+j)n} \right] - \sum_{n=0}^{N-1} x_n e^{-i\omega_m n} \\ &= \langle \boldsymbol{x}, \boldsymbol{g}(\omega_m) \rangle, \end{aligned} \tag{2.18}$$

where $\boldsymbol{g}$ is given by,

$$\begin{aligned} g_n(\omega_m) &= \left[\sum_{j=1}^{J} e^{i\gamma(k_m+j)n} u_j^*(\omega_m)\right] - e^{i\omega_m n}, \qquad \text{for } n = 0, \ldots, N-1, \text{ or,} \\ \boldsymbol{g} &= \boldsymbol{H}(\omega_m)\boldsymbol{W}\boldsymbol{u}(\omega_m) - \boldsymbol{b}(\omega_m), \end{aligned} \tag{2.19}$$

where the diagonal matrix $H_{n,n}(\omega_m) = e^{i\gamma k_m n}$, $W_{n,j} = e^{i\gamma nj}$, and $b_n(\omega_m) = e^{i\omega_m n}$. In this form, the min-max problem becomes,

$$\min_{\boldsymbol{u}(\omega)\in\mathbb{C}^J} \max_{\boldsymbol{x}\in\mathbb{C}^N:\|\boldsymbol{x}\|=1} |\langle \boldsymbol{x}, \boldsymbol{g}(\omega_m)\rangle|. \tag{2.20}$$

Using the Cauchy-Schwarz inequality, the worst case signal is $\boldsymbol{x} = \boldsymbol{g}^*(\omega)/\|\boldsymbol{g}(\omega)\|$ and the min-max problem is reduced to a least squares with the following solution:

$$\boldsymbol{u}(\omega_m) = (\boldsymbol{W}^\star\boldsymbol{W})^{-1}\boldsymbol{W}^\star\boldsymbol{H}^\star(\omega_m)\boldsymbol{b}(\omega_m). \tag{2.21}$$

Remarkably, the calculation of Equation (2.21) is assisted by closed-form expressions for two components,

$$\begin{aligned} \left[\boldsymbol{W}^\star\boldsymbol{W}\right]_{l,j} &= \kappa(j-l) \\ \left[\boldsymbol{W}^\star\boldsymbol{H}^\star(\omega_m)\boldsymbol{b}(\omega_m)\right]_n &= \kappa(\omega_m/\gamma - k_m - n) \end{aligned} \tag{2.22}$$

with $\kappa(t) \triangleq e^{-i\pi t/K}\sin(\pi tN/K)/\sin(\pi t/K)$. As can be seen in Equation (2.21), calculation of the interpolator involves inverting the $J \times J$ matrix $(\boldsymbol{W}^\star\boldsymbol{W})$ that does not depend on the specific position of the nonuniform sampling location.

The shape of the min-max interpolator is shown in Figure 2.1 for various values of ω/γ for both even and odd values of J. For even J, the min-max interpolator is not differentiable at integer arguments. For odd J, the interpolator is not continuous at integer arguments due to the neighborhood changing at that point, see Equation (2.15). The sinc interpolator is shown for reference in these figures.

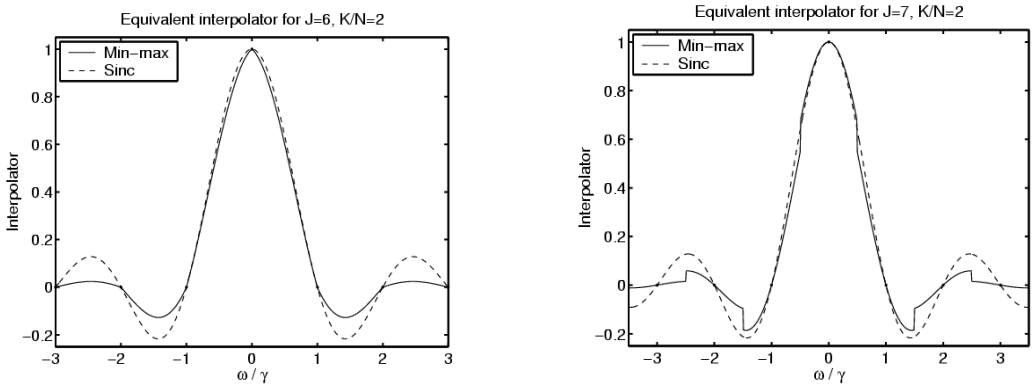

a b

Figure 2.1: Min-max interpolator corresponding to Equation (2.21) for $N = 128, K/N = 2$ for a.) $J = 6$ and b.) $J = 7$.

The accuracy of this NUFFT is greatly increased through the use of spatially varying scaling factors in Equation (2.13). These scaling factors are analogous to the deapodization function in the gridding algorithm, but are applied as a precompensation instead of a postcompensation because we are performing the reverse of the gridding operation. The purpose of the scaling factors is to partially precompensate for errors in the interpolation. Two approaches were examined for determining appropriate scaling factors: numerical optimization and Fourier inversion of the resulting interpolation function (analogous to the gridding case). For numerical optimization, the scaling factors were expanded in terms of a truncated Fourier series as,

$$s_n = \sum_{t=-L}^{L} \alpha_t e^{i\gamma\beta(n-\eta_o)}, \tag{2.23}$$

where $\eta_o = (N-1)/2$ and the natural fundamental frequency corresponds to $\beta = K/N$, but β could also be an optimization parameter. By restricting the α_t's to be Hermitian symmetric, optimization over the scaling factors is reduced to optimization over $L+1$ coefficients. Lacking an analytical solution, this optimization was

performed by a brute force global search and was possible only for small values of L.

Results

Figure 2.2 shows the resulting error of the NUFFT method versus an optimized Kaiser-Bessel and Gaussian interpolators. The parameter L refers to the number of Fourier coefficients used in the FT of the scaling function. The NUFFT allowed a reduction in computation time for the FT from $O(N^2)$ to $O(K \log K)$, where K is typically $2N$ or $3N$ [35]. As shown in Figure 2.2, the optimized Kaiser-Bessel interpolator is nearly as accurate as the best min-max interpolator we found during an expensive search over scaling factors. Since the Kaiser-Bessel interpolator is easy to compute, we use this version of the NUFFT in our work. Then the scaling factors are found by an inverse transform of the Kaiser-Bessel interpolator.

2.3.3 Time Segmentation

The previous section gave our derivation of the min-max optimal NUFFT to allow for quick, accurate reconstruction of MRI data on arbitrary k-space trajectories. However, the standard NUFFT method by itself does not allow for the compensation of field inhomogeneity effects because the integral signal equation for MR is not a Fourier transform when field inhomogeneities are included. Inspired by the time-segmented conjugate-phase reconstruction approach [30], we propose a fast time-segmented forward projector, and its adjoint, that accounts for field effects and uses the NUFFT. The possibility of combining "conventionally used [time or frequency] segmentation approaches" with NUFFT-type methods to correct for field inhomogeneities was noted by Pruessman *et al.* [39]. However, as we show in this section,

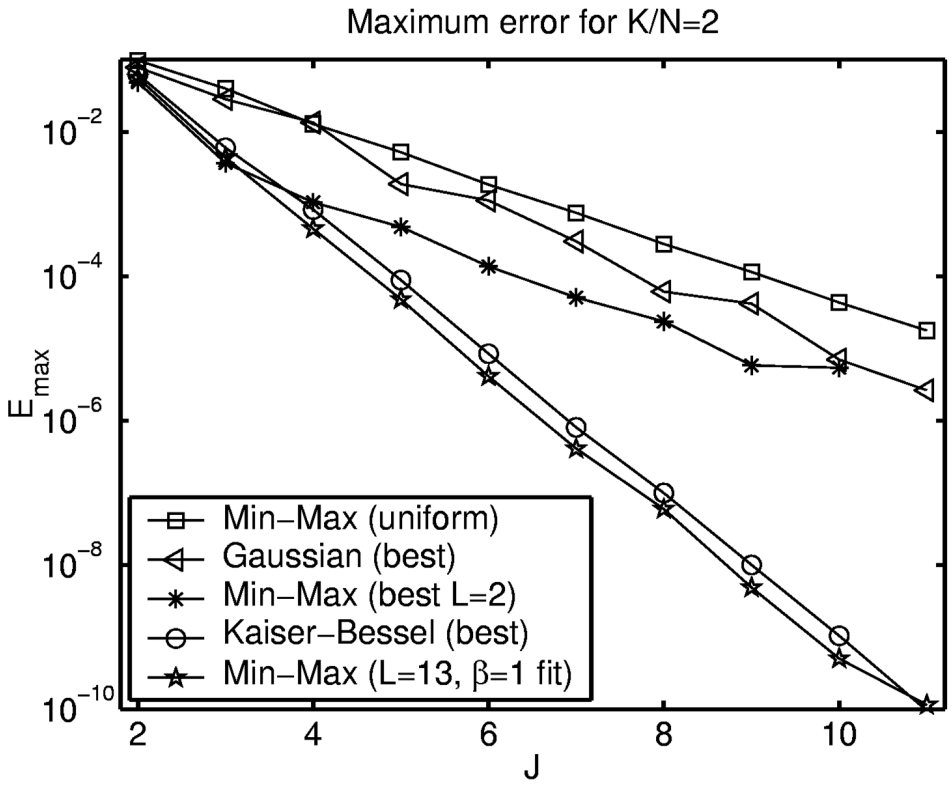

Figure 2.2: Maximum error for various interpolators with neighborhood size J. Interpolators shown are the min-max interpolator using uniform weights $s_n = 1$, an optimized Gaussian interpolator, the min-max interpolator with optimized weights and $L = 2$, an optimized Kaiser-Bessel interpolator with Fourier transform weights, and a min-max interpolator with optimized weights $L = 13$ and $\beta = 1$.

the conventional temporal interpolators (linear, Hanning, etc.) are signficantly sub-optimal since they fail to capture the oscillatory nature of phase modulations caused by off-resonance effects. Instead, in this section we present a temporal interpolation method that is optimal in the min-max sense of minimizing worst-case interpolation error, and compare its accuracy to the "conventional" temporal interpolators. We show that accurate temporal interpolation combined with the NUFFT results in a fast, accurate iterative reconstruction algorithm for field-corrected imaging. We evaluate the accuracy of our time-segmentation interpolator by comparing it to the

result of the exact (but slow) evaluation of the signal equation.

Derivation of Min-Max Temporal Interpolator

In Equation (2.7), the computational problem arises in the term $e^{-i\omega_n t}$, where t is not a constant. If t were a constant, then the term $e^{-i\omega_n t}$ could be absorbed into f_n and (2.7) could be evaluated quickly by the NUFFT. The idea of "time segmentation" is to use small time segments over which t is approximately constant [30]. For a time-segmented approximation of the term $e^{-i\omega_n t}$, we partition the acquisition window into L time segments of width τ and compute the term at the $L+1$ break points. We then interpolate between these break points to evaluate an approximation at intermediate time points as follows:

$$e^{-i\omega_n t} \approx \sum_{l=0}^{L} a_l(t) e^{-i\omega_n \tau l}, \tag{2.24}$$

where $a_l(t)$ is the interpolation coefficient for the lth break point for time t. Replacing the term $e^{-i\omega_n t}$ in Equation (2.7) with its time-segmented approximation Equation (2.24) gives:

$$\hat{s}(t) \;=\; \Phi(\boldsymbol{k}(t)) \sum_{l=0}^{L} a_l(t) \sum_{n=0}^{N-1} \left[f_n e^{-i\omega_n \tau l} \right] e^{-i2\pi(\boldsymbol{k}(t)\cdot \boldsymbol{r}_n)}. \tag{2.25}$$

The key property of Equation (2.25) is that it is a weighted sum of discrete-space Fourier transforms of the term in brackets, weighted by the coefficients $\boldsymbol{a}(t) = (a_0(t), \ldots, a_L(t))'$. We can perform these inner FT's quickly and accurately using an NUFFT. Our goal here is to choose the $\boldsymbol{a}(t)$ to minimize the error of approximation Equation (2.25). In the spirit of [35, 63] and Section 2.3.2, we propose to adopt a min-max criterion to optimize the temporal interpolation coefficients, $\boldsymbol{a}(t_i)$

for $i = 1, \ldots, M$, *i.e.*, for every point in the k-space readout. For any time t, we choose the coefficients $\boldsymbol{a}(t)$ using the following criterion:

$$\min_{\boldsymbol{a}(t)} \max_{\boldsymbol{f} \in \mathbb{C}^N : \|\boldsymbol{f}\|=1} \left| \frac{\hat{s}(t) - s(t)}{\Phi(\boldsymbol{k}(t))} \right|. \tag{2.26}$$

That is, we seek the interpolation coefficients $\boldsymbol{a}(t)$ that will minimize (min) the interpolation error for the object vector, $\boldsymbol{f}$, that causes the largest (max) error of all possible signals. Note that if $\Phi(\boldsymbol{k}(t)) = 0$, then the error in the approximation (2.25) would be zero regardless of the interpolator.

The error in the approximation (2.25) can be expressed as,

$$\begin{aligned} \frac{\hat{s}(t) - s(t)}{\Phi(\boldsymbol{k}(t))} &= \sum_{n=0}^{N-1} f_n e^{-i2\pi(\boldsymbol{k}(t)\cdot\boldsymbol{r}_n)} \left[\sum_{l=0}^{L} a_l(t) e^{-i\omega_n \tau l} - e^{-i\omega_n t} \right] \\ &= \sum_{n=0}^{N-1} g_n(t) f_n e^{-i2\pi(\boldsymbol{k}(t)\cdot\boldsymbol{r}_n)}, \\ &= \sqrt{N} \langle \boldsymbol{g}(t), \boldsymbol{h}(t) \rangle, \end{aligned} \tag{2.27}$$

where $\boldsymbol{g}(t) = (g_0, \ldots, g_{N-1})$, $\boldsymbol{h} = (h_0, \ldots, h_{N-1})$, and

$$\begin{aligned} g_n(t) &= \frac{1}{\sqrt{N}} \left[\sum_{l=0}^{L} a_l(t) e^{-i\omega_n \tau l} - e^{-i\omega_n t} \right] \\ h_n(t) &= {f_n}^{\star} e^{i2\pi(\boldsymbol{k}(t)\cdot\boldsymbol{r}_n)}. \end{aligned} \tag{2.28}$$

Define $b_n(t) = \left(1/\sqrt{N}\right) e^{-i\omega_n t}$, and let $\boldsymbol{G}$ be an N by $L+1$ matrix with $\boldsymbol{G}_{nl} = \left(1/\sqrt{N}\right) e^{-i\omega_n \tau l}$, then,

$$\boldsymbol{g}(t) = \boldsymbol{G}\boldsymbol{a}(t) - \boldsymbol{b}(t). \tag{2.29}$$

From Equation (2.28), $\|\boldsymbol{f}\| = \|\boldsymbol{h}(t)\|$ and $\|\boldsymbol{h}(t)\|$ is independent of time. Therefore, using Equation (2.27), we can rewrite our min-max estimation problem from (2.26)

as follows

$$\min_{\boldsymbol{a}(t)} \max_{\boldsymbol{h}\in\mathbb{C}^N:\|\boldsymbol{h}\|=1} \sqrt{N}|\langle \boldsymbol{g}(t), \boldsymbol{h}\rangle|. \tag{2.30}$$

By the Cauchy-Schwarz inequality, for a given time t, the worst-case $\boldsymbol{h}$ is $\boldsymbol{g}^\star(t)/\|\boldsymbol{g}(t)\|$, *i.e.*,

$$\max_{\boldsymbol{h}\in\mathbb{C}^N:\|\boldsymbol{h}\|=1} |\langle \boldsymbol{g}(t), \boldsymbol{h}\rangle| = \|\boldsymbol{g}(t)\|. \tag{2.31}$$

Note that this is the approximation error in Equation (2.24). Inserting this worst-case $\boldsymbol{h}$ into the min-max criterion (2.30) and applying Equation (2.29) reduces the min-max problem to,

$$\min_{\boldsymbol{a}(t)} \|\boldsymbol{G}\boldsymbol{a}(t) - \boldsymbol{b}(t)\|. \tag{2.32}$$

The solution to this least-squares problem yields the min-max interpolator:

$$\boldsymbol{a}(t) = (\boldsymbol{G}^\star\boldsymbol{G})^{-1}\boldsymbol{G}^\star\boldsymbol{b}(t), \tag{2.33}$$

where

$$\begin{aligned} [\boldsymbol{G}^\star\boldsymbol{G}]_{l,l'} &= \frac{1}{N}\sum_{n=0}^{N-1} e^{-i\omega_n\tau(l'-l)} \\ [\boldsymbol{G}^\star\boldsymbol{b}(t)]_l &= \frac{1}{N}\sum_{n=0}^{N-1} e^{-i\omega_n(t-\tau l)}, \end{aligned} \tag{2.34}$$

for $l, l' = 0, \ldots, L$. To compute the min-max interpolator, we form the $(L+1)\times(L+1)$ matrix $\boldsymbol{G}^\star\boldsymbol{G}$ and multiply its inverse by the $(L+1)\times 1$ vector $\boldsymbol{G}^\star\boldsymbol{b}(t)$. Typically $L \ll N$ so this is feasible.

Computing the Min-Max Interpolator

The interpolator in Equation (2.33) is object dependent since it is a function of the field map, $\boldsymbol{\omega} = (\omega_0, \ldots, \omega_{N-1})$, and therefore must be computed after an initial estimate of the field map is formed. To compute $\boldsymbol{G}^\star\boldsymbol{G}$ efficiently, first form the column sums of $\boldsymbol{G}$ as follows:

$$\gamma_l \triangleq \frac{1}{\sqrt{N}} \sum_{n=0}^{N-1} \boldsymbol{G}_{n,l}, \text{for } l = 0 \ldots, L. \tag{2.35}$$

Then using Equation (2.34), we evaluate the elements of $\boldsymbol{G}^\star\boldsymbol{G}$ as follows:

$$[\boldsymbol{G}^\star\boldsymbol{G}]_{l,l'} = \begin{cases} \gamma_{l'-l} & l' - l \geq 0 \\ \gamma^\star{}_{l-l'} & \text{otherwise.} \end{cases} \tag{2.36}$$

This is a very fast way to compute $\boldsymbol{G}^\star\boldsymbol{G}$ for the min-max interpolator.

The sums in Equation (2.34) do not depend on the spatial arrangement of the field map. This independence suggests that we could compute these sums using simply a histogram of the field map values. We have investigated approximating the computation of Equation (2.34) by forming the histogram of the field map using N_B equal-sized bins covering the range of offset frequencies induced by the field inhomogeneity. Let m_p be the number of field map values that fall into bin p with a center off-resonant frequency of f_p. Then we can approximate Equation (2.34) by

$$\begin{aligned} [\boldsymbol{G}^\star\boldsymbol{G}]_{l,l'} &\approx \frac{1}{N} \sum_{p=1}^{N_B} m_p e^{-i2\pi \mathrm{f}_p \tau (l'-l)}, \\ [\boldsymbol{G}^\star\boldsymbol{b}(t)]_l &\approx \frac{1}{N} \sum_{p=1}^{N_B} m_p e^{-i2\pi \mathrm{f}_p (t-\tau l)}. \end{aligned} \tag{2.37}$$

We compute Equation (2.37) efficiently via a FFT of m_p, since we use equally-spaced histogram bins. We call this approach the *histogram approximation* to the min-max

interpolator. This quantization of the field map into a histogram is somewhat akin to the frequency-segmentation method for reducing computation in the conjugate-phase approach for field inhomogeneity correction [64, 65].

The expression for this interpolator bears a striking resemblance to the "multi-frequency interpolator" proposed by Man *et al.* [32]. However, the use of the two interpolators is quite different. The multifrequency interpolator is applied to a set of images that have each been reconstructed by a constant demodulation approximation to the conjugate-phase approach for field inhomogeneity correction. In contrast, our min-max interpolator is applied to predicted k-space signals. The multifrequency interpolation approach inherits the fundamental limitations of the conjugate-phase approach (in particular the requirement of a spatially smooth field map) which are illustrated in the figures in Sections 2.3.3.

The min-max interpolator (2.33) depends on the field map and should be recomputed if the field map changes. To avoid recalculating the interpolator coefficients when a field map is updated, we also investigated the use of an object-independent histogram for the field map values. A generic histogram for field maps was used to calculate the interpolator coefficients in (2.37) and we will refer to this approach as the *generic histogram approximation*. Several shapes and ranges for generic histograms were examined.

METHODS

Three sets of studies were performed to evaluate the accuracy and utility of our min-max interpolated iterative reconstruction algorithm. All three studies used a

single-shot spiral k-space trajectory with a T_E of 25 ms, matrix size of 64×64, and FOV of 22 cm×22 cm, giving 3770 k-space points. The length of the readout interval was 18.9 ms, so 100 Hz off resonance causes 3.8π extra spin phase accrual during the readout.

Interpolator Accuracy We performed a simulation study to evaluate the maximum interpolation error, $\|\boldsymbol{g}(t)\|$ in Equation (2.31), over a finely sampled range of times, t, for several temporal interpolators. We used the field map $\boldsymbol{\omega}$ shown in Figure 2.3. We observed empirically that, for many field maps, the min-max optimal temporal interpolator could have a significant imaginary component, and this imaginary component contributes to the overall accuracy of the min-max interpolation method. Conventional temporal interpolators used in MRI have been real valued, so to simplify comparisons between the proposed min-max approach and the conventional approaches, we shifted the field map values to a range where the min-max interpolator had a very small imaginary component, as illustrated in Figure 2.5. We compared the following interpolation methods: linear interpolation of the two nearest endpoints to the time sample of interest, a Hanning window interpolation using only the two nearest endpoints (similar to that used in [30] for the back-projector problem), the ideal min-max interpolator (2.33), the histogram approximation to the min-max interpolator calculated using (2.37) with 1000 bins, and an interpolator using a generic histogram also calculated using (2.37). Various shapes (flat and triangular) and ranges were used for the generic histogram to determine the effect of accuracy of the histogram on the error of the interpolator.

Simulation Study We performed a series of simulation studies using the same field map and a simulation object shown in Figure 2.3. The simulation data was formed by constructing a simulation phantom at a matrix size of 256×256 and then applying (2.7) to compute the signal at the desired k-space locations. To avoid intravoxel effects from gradients of the field map inside our larger reconstructed voxels (matrix size of 64×64), we constructed the simulated field map at a size of 64×64 and zero-order-hold interpolated it up to 256×256 to create the simulation field map. (We also present one case that includes intravoxel dephasing for comparison.) Noise-free simulation studies were conducted to examine the effect of iteration on the interpolation error by computing the normalized root-mean-squared (NRMS) difference in the reconstructed image of the interpolated, time-segmented approach versus using the exact (slow) signal equation (2.7) at convergence.

For the rest of the simulation studies, zero-mean complex Gaussian noise was added to the k-space data to give an SNR of approximately 100, calculated as the ratio of the norms of the k-space data vector and the noise vector: $\|\boldsymbol{s}\|/\|\boldsymbol{\varepsilon}\|$. We examined the normalized root-mean-squared error (NRMSE) between the reconstructed image and the known simulation object. This measure was used to examine accuracy and convergence rate of our proposed iterative algorithm. In the simulation and human studies, the NUFFT was used with the following parameters: 2 times oversampling, a neighborhood size of 5×5, and an optimized Kaiser-Bessel window and scaling factors [35].

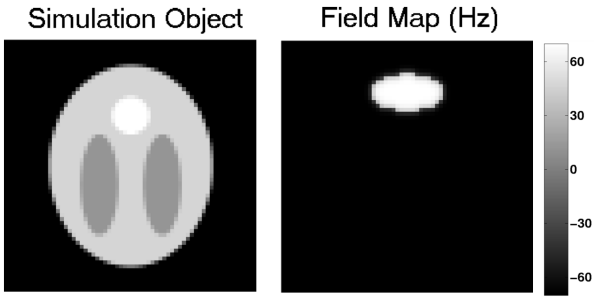

Figure 2.3: Simulation object and field map in Hz.

Human Study The time-segmented, NUFFT reconstruction scheme was applied to a human data set collected on a 3.0T GE Signa Scanner in accordance with the Institutional Review Board of the University of Michigan. For the human data, the field inhomogeneity map must be measured by acquiring 2 gradient echo images with slightly different echo times [2]. To minimize field inhomogeneity distortions in the images used to estimate the field map, we acquired a pair of 4-shot gradient echo images with T_E's of 5 and 7 ms. This field map was used to reconstruct field-corrected images of the same slices with single-shot spirals at a T_E of 25 ms. The proposed fast, iterative reconstruction scheme was compared to the conjugate phase method and an uncorrected gridding reconstruction. Since the exact object is not known in a human data set, we attempted to match the full conjugate phase and iterative reconstruction times and qualitatively compare the resulting images.

RESULTS

Interpolator Accuracy Figure 2.4 shows the maximum interpolation error for $L = 1$ through $L = 13$ time segments for the five interpolators described above in Section 2.3.3. The error given, $\max_t \|\boldsymbol{g}(t)\|$, is the maximum error in interpolation as

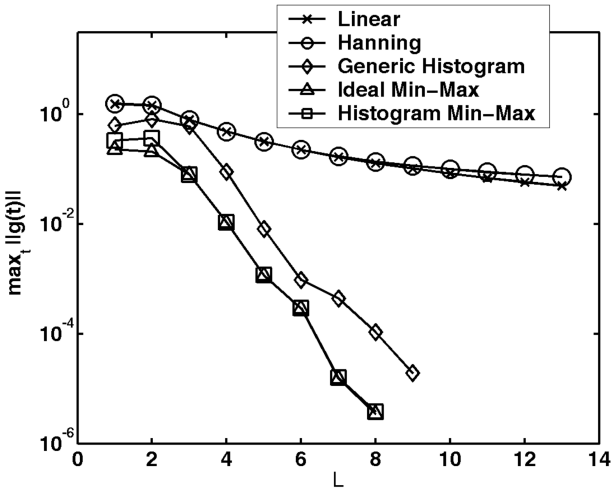

Figure 2.4: Maximum interpolation error over a range of time points for each interpolator for various numbers of time segments. Error given is the maximum error in interpolation over a range of times as given in (2.31).

given in (2.31) over a range of times t. The generic histogram used was flat over the range of [-75, 75] Hz. The min-max interpolators (ideal min-max, histogram min-max, and generic histogram min-max) have been plotted until the condition number of the $(\boldsymbol{G}^\star\boldsymbol{G})$ matrix becomes too large for inversion. For $L = 8$ the maximum error for the min-max and histogram interpolator is more than 4 orders of magnitude lower than that of the linear and Hanning "conventional" interpolators.

Figure 2.5 shows the Hanning and min-max interpolators for $L = 5$. The real and imaginary parts of the min-max interpolator are oscillatory, a property not found in the conventional interpolators. The histogram interpolators looked very similar to the ideal min-max interpolator, even though the generic histogram had a different range of off-resonance frequencies and different histogram shape (flat). Even though it was not explicitly required in our formulation, the min-max interpolators appear to sum to unity at every time point, a property expected of interpolators.

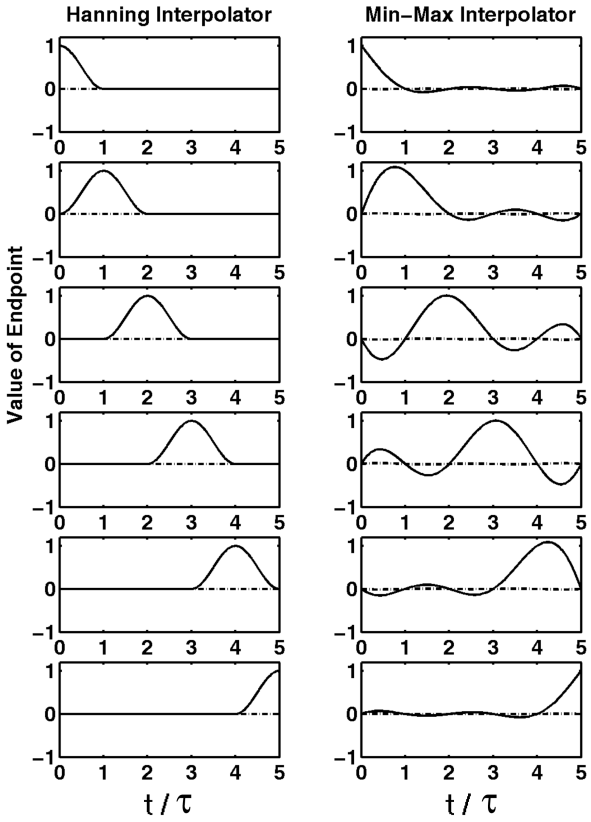

Figure 2.5: Real (solid lines) and imaginary (dashed lines) parts of interpolators using $L = 5$ for the Hanning and min-max interpolators for the field map given in Figure 2.3.

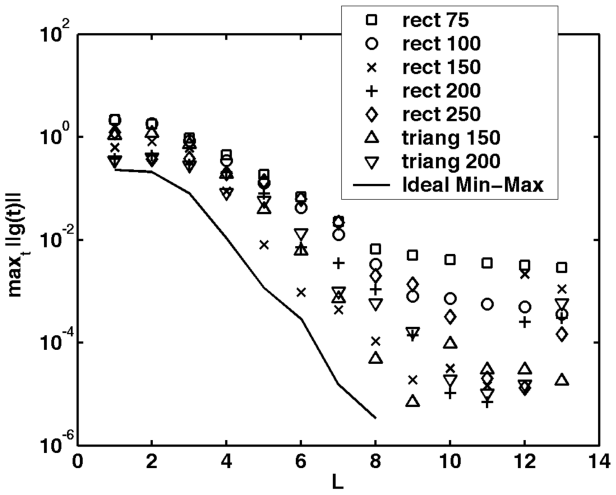

Figure 2.6: Comparison of maximum interpolation error of various generic histogram approximate min-max interpolators.

When a histogram of the field map is used that differs from the actual field map (generic histogram), the max error in Figure 2.4 showed a slightly higher level of error compared to the ideal min-max interpolator and required a larger number of time segments. We investigated several generic histograms, rectangular and triangular shapes, and several different ranges of off-resonance, 75, 100, 150, 200, and 250 Hz. All the generic histograms were centered around 0 Hz, to agree with the simulated field map. Figure 2.6 shows the maximum NRMSE for various numbers of time segments. As seen in this figure, the interpolator is relatively immune to moderate changes in the histogram of the field map. At values of L of 11 and 12, the rectangular histograms with ranges of 150, 200, and 250 Hz and triangular histograms with ranges of 150 and 200 Hz all provide maximum interpolation errors below 10^{-4}. Given the independence on spatial arrangement in the formulation of the ideal min-max interpolator, we need only have a range of off-resonance in our histogram that is similar to that of the exact field map.

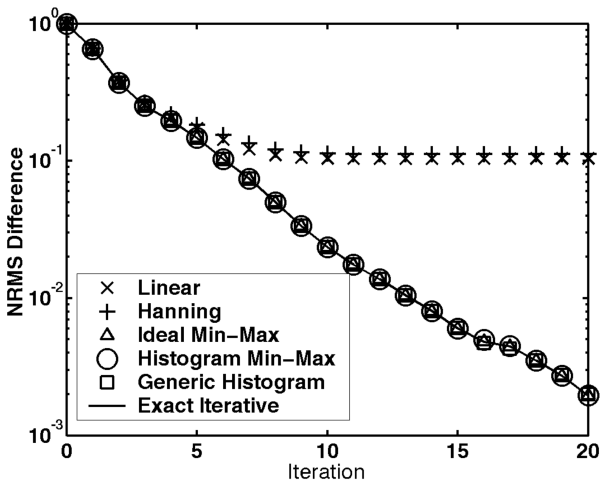

Figure 2.7: NRMS difference between $\boldsymbol{f}_k^{\text{approx}}$ and $\boldsymbol{f}_{100}^{\text{exact}}$ for $L = 6$ in simulation study.

Simulation Study As described in Section 2.3.1, we examined the convergence of the CG algorithm under various conditions using the simulation object and field map shown in Figure 2.3. Considering the max error in Figure 2.4, we selected $L = 6$ to give a low error for the min-max interpolator, and examined the error of time segmentation versus using the exact (slow) signal equation (2.7) over iteration to see how the error propagates through the iterative process. Figure 2.7 shows the NRMS difference between $\boldsymbol{f}_k^{\text{approx}}$ and $\boldsymbol{f}_{100}^{\text{exact}}$ where $\boldsymbol{f}_k^{\text{approx}}$ denotes the kth iteration of CG algorithm with the fast approximation (2.25) using various interpolators and $\boldsymbol{f}_{100}^{\text{exact}}$ denotes the 100th iteration (*i.e.* essentially at convergence) of CG using the exact (slow) signal equation (2.7). As shown in Figure 2.7, interpolation errors can cause the CG algorithm to converge to a different image. The linear and Hanning interpolated iterative methods converge to a final image that differs from the exact final image by more than 10% NRMS.

To choose a value for L that gives fast computation yet retains good reconstruc-

tion accuracy, we examined the NRMS difference between the interpolated and exact iterative methods for various values of L. Figure 2.8 shows the NRMS difference between $\boldsymbol{f}_{100}^{\text{exact}}$ and $\boldsymbol{f}_{k}^{\text{approx}}$ over 20 iterations using the ideal min-max interpolator for $L = 1, 3, 4, 5$. Computation time for the min-max interpolated iterative method is approximately proportional to $L + 1$. On a 2 GHz Xeon workstation using Matlab (The Mathworks, Natick MA), our implementation of the exact (slow) iterative method, using (2.7), took $\approx$12.7 s per iteration to evaluate. The min-max interpolation method, took approximately $(0.019 + 0.030(L + 1))$ s per iteration for values of $L = 1, \ldots, 13$. The linear interpolated method took approximately the same computation time as the min-max interpolated method and is shown for reference in Figure 2.8. Depending on the noise level expected in our reconstructed images, a value of $L = 4$ might be reasonable for the min-max interpolator. We chose to use $L = 5$ for the ideal min-max interpolator for our simulation and human data studies with a time per iteration of 0.2 sec., a speed-up of around 60 over the exact iterative method.

Next, given the exact field map, we ran a simulation study with noise to compare the errors in the reconstructed images under five different reconstruction schemes: no correction for field inhomogeneities, a conjugate-phase reconstruction with density compensation, a fast conjugate phase reconstruction using time segmentation according to [30], the exact (slow) evaluation of the signal equation used in combination with the CG algorithm (the slow iterative method), and the NUFFT with min-max temporal interpolation used in combination with the CG algorithm (the

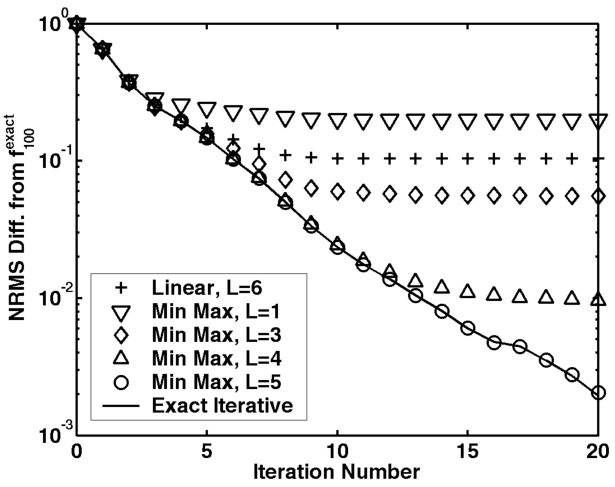

Figure 2.8: NRMS difference between $\boldsymbol{f}_k^{\text{approx}}$ using the ideal min-max interpolator for $L = 1, 3, 4, 5$ and $\boldsymbol{f}_{100}^{\text{exact}}$ over 20 iterations. The time to compute the exact iterative method, using (2.7), was ≈12.7 s per iteration while the time to compute the fast, interpolated iterative method, using (2.25), was $(0.019 + 0.030(L + 1))$ s per iteration.

fast iterative method, $L = 5$). The results of NRMSE and computation time are shown in Table 2.1. The NRMSE was calculated over a mask defined by the true object's support. Figure 2.9 shows the reconstructed images. The full iterative and fast iterative methods give virtually the same results with a NRMS difference between the two reconstructions of 0.07%, but the fast iterative method takes only 2.2 s for 10 iterations as compared to 128 s for the slow iterative method. The unsegmented, density-compensated conjugate-phase reconstruction takes 4 s and both conjugate phase reconstructions produce serious artifacts in regions where the field map is not smoothly varying, and these artifacts propagate to nearby regions.

To verify that interpolator accuracy is important in reconstructing field-corrected images, we compared reconstructions from the CG algorithm using NUFFT with linear, Hanning, and ideal min-max interpolators. Figure 2.10 shows the reconstructions

Reconstruction Method	**Time (s)**	**NRMSE** of complex	**NRMSE** of magnitude
No Correction	0.06	1.354	0.217
Full Conjugate Phase	4.07	0.306	0.185
Fast Conjugate Phase	0.33	0.319	0.190
Fast Iterative (10 iters)	2.20	0.0423	0.0392
Exact Iterative (10 iters)	128.16	0.0423	0.0393

Table 2.1: Computation time and NRMSE between $\hat{f}$ and f_{true} for simulation study

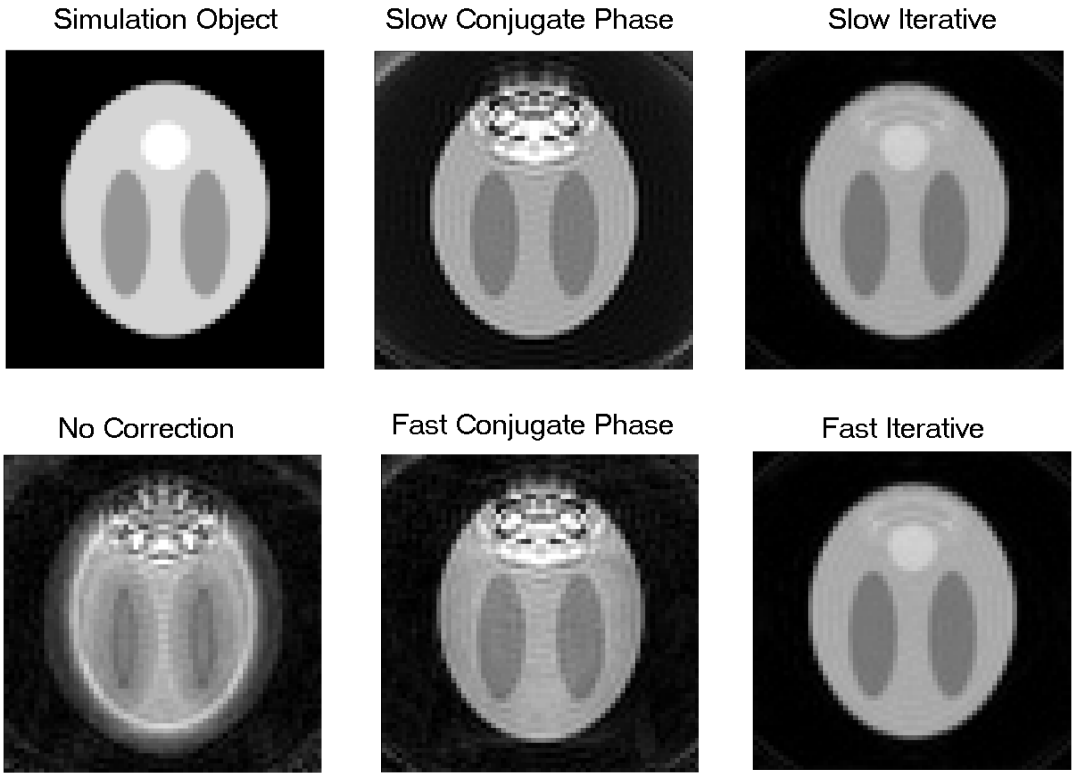

Figure 2.9: Reconstructed images from the simulation study.

using $L = 5$ and ten iterations of the CG algorithm. The standard interpolators are insufficiently accurate and the algorithm converges to a distorted image, whereas the min-max method yields a nearly undistorted image. This behavior agrees with the quantitative comparison shown in Figure 2.7.

As mentioned in Section 2.3.3, the simulated field map was purposefully constructed to avoid intravoxel dephasing due to within-voxel field inhomogeneities. To show the effects of such dephasing on the field-corrected reconstructions of Figure 2.9, we simulated a field map at a 256×256 matrix size that allowed gradients across the voxels when reconstructed at a matrix size of 64×64. Figure 2.11 shows the reconstructed images. As this figure shows, by assuming basis functions of rect($\boldsymbol{r}$), we are unable to model the field gradients across the voxel and the result is signal loss where the field gradient is high. In the iterative reconstruction, this degradation is localized primarily in the pixels where the high gradient occurs. In the conventional field correction, the artifacts are more widespread. We plan to implement triangular basis functions in our future work to model linear intravoxel susceptibility gradients, or to use over-sampled field maps.

Human Data As a final comparison, we reconstructed real data collected from a slice of the brain using both the proposed iterative method and a full conjugate phase method. Although the proposed iterative method can be used in an extended form to estimate an undistorted field map, in this case we focused on comparing computation time, so both reconstructions used a field map obtained in the standard way from two short T_E (5, 7 ms) 4-shot gradient echo images. For convenience in the iterative

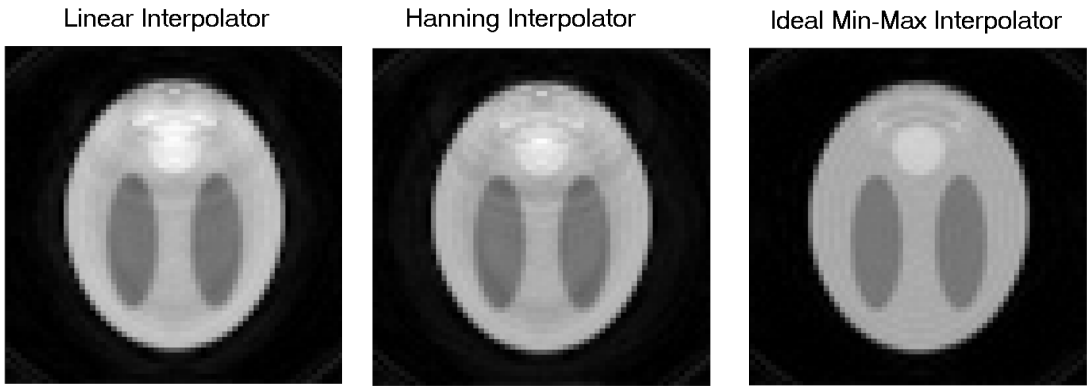

Figure 2.10: Effect of temporal interpolator on fast iterative reconstructions.

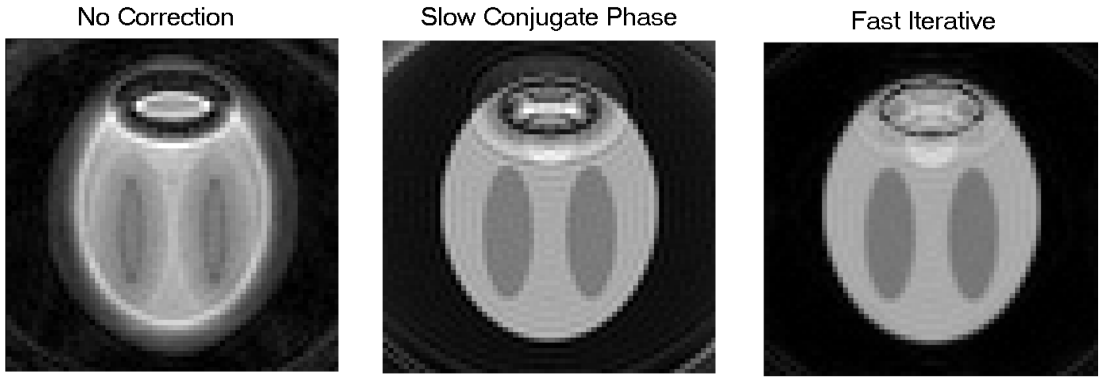

Figure 2.11: Reconstructed images from a simulation study with intravoxel field effects.

method, we used the generic histogram (flat, [0,150] Hz) since it does not depend on the specific field map and can be computed in advance for a given trajectory (depends only on number of time points and a chosen range of off-resonance frequencies). The range of the generic histogram, [0, 150] Hz, was chosen to agree with our routinely acquired field maps from the slice of interest. The NUFFT used the parameters given in Section 2.3.3 and the min-max interpolator used $L = 8$. The reconstruction time for the full conjugate phase was about 4 s, the time for ten iterations of the proposed fast iterative method was 3.6 s. Figure 2.12 shows the reconstructed images for 2 slices. Artifacts in regions of high off-resonance are reduced significantly by the iterative approach. The conjugate phase reconstruction suffers from ringing and piling-up artifacts near the region of field inhomogeneity. Residual signal loss in the iterative reconstruction could be due to a high in-plane gradient in the field map or may be due to through-plane susceptibility gradients. We plan to incorporate models of both phenomena in our future work. Also, the iterative method can be used to simultaneously estimate an undistorted field map and provide a better field-corrected image [33, 66].

DISCUSSION

We have presented a method that allows fast, iterative reconstruction of field-corrected MR images. By combining the NUFFT with time segmentation using a min-max temporal interpolator, a computation speed up of a factor of around 60 is achievable with NRMS error in the reconstructed image of 0.07%. We have also developed an approximation to the min-max interpolator that depends on the

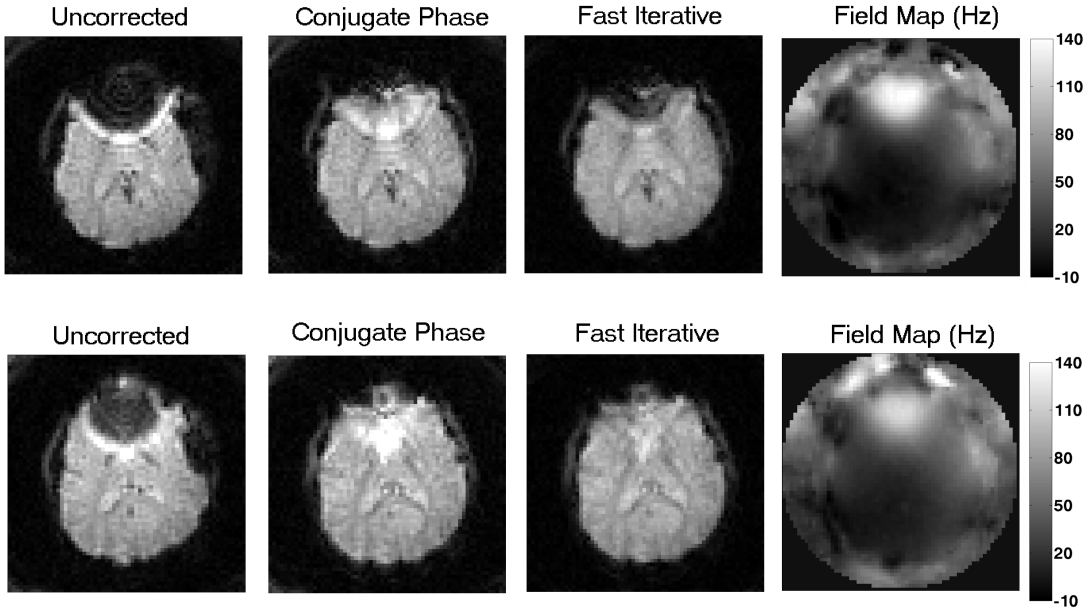

Figure 2.12: Distorted image, its field map, conjugate phase and iterative image reconstructions for 2 slices. The time for the field-corrected reconstructions were about 4 s each.

object-specific field map only through the range of off-resonant frequencies yet provides accuracies near those of the ideal min-max interpolator. For a given trajectory, this interpolator can be precomputed and stored. We have shown that this approximation is relatively robust to small changes in the shape or range of the histogram of the field map. This method should easily be adaptable to other forms of iterative reconstruction in MRI, including SENSE to allow fast, field-corrected SENSE reconstructions [67].

We envision the iterative reconstruction algorithm in the general case to proceed as follows: first, an initial field map is formed via a gridding reconstruction on data at two different echo times. This initial estimate of the field map is used to derive an interpolator for the min-max time interpolation. The estimate of the field map

is also used, via a fast conjugate phase reconstruction, to give an initial estimate to the iterative reconstruction. The iterative reconstruction is then run in extended mode with simultaneous estimation of field map and image either by explicit joint estimation [66] or by alternating updates [31,33]. After several loops of updating the image and field map, we are left with an undistorted estimate of the image and field map.

If the field map has a strong linear component, then it may be possible to adapt the method of Irarrazabal *et al.* [65] to reduce the number of segments required for a given accuracy.

The ability to accurately compensate for off-resonance effects as demonstrated here may increase the feasibility of using other acquisition methods with long readout times, such as echo-volume imaging [68].

Although this section has focused on MR image reconstruction in the presence of field inhomogeneities, the general approach is also applicable to image reconstruction with compensation for other sources of undesired (but known) spin phase accrual, such as eddy currents and concomitant gradient effects [69, 70]. An iterative method based on an explicit signal model like (2.4) should yield more accurate images compared to conventional approaches to compensating for such effects.

We have ignored spin-spin relaxation during the signal readout in our signal model (2.4). However, many aspects of the algorithms we have described are also applicable to problems where both spin density and spin relaxation are estimated from multi-echo measurements [71–74]. The framework for the min-max time interpolation

provided by (2.32) can be extended to include relaxation effects, such as R_2^*. The simplifications that resulted in (2.34) are not available in this case and computation of the interpolator may be more expensive. Preliminary testing shows that the high accuracy of the time segmentation method can still be achieved without knowing the exact field and R_2^* maps. This work will be explored further in Chapter 5.

CHAPTER 3

Sensitivity Encoding[1]

3.1 Introduction

If we neglect field inhomogeneity and relaxation in (1.25), the data is a Fourier encoding of the image. If the Nyquist sampling rate is satisfied, we have adequate information about the spatial frequencies of the image to reconstruct an unaliased version of the image. Looking at (1.24) we can see that the signal equation includes coil sensitivity information. We can combine the data from multiple coils, each with its own sensitivity into a larger system of equations as follows:

$$\begin{bmatrix} s_1(t) \\ s_2(t) \\ s_3(t) \\ s_4(t) \end{bmatrix} = \begin{bmatrix} \boldsymbol{A}D(\mathbf{c}_1) \\ \boldsymbol{A}D(\mathbf{c}_2) \\ \boldsymbol{A}D(\mathbf{c}_3) \\ \boldsymbol{A}D(\mathbf{c}_4) \end{bmatrix} \boldsymbol{f}, \tag{3.1}$$

where $s_l(t)$ is the signal received from coil l and $D(\mathbf{c}_l)$ is a diagonal matrix with the coil sensitivity values along the diagonal. If k-space is not adequately sampled, then reconstructing the signal received from the lth coil, $s_l(t)$, results in an aliased image of the object, $\boldsymbol{f}$, weighted by the sensitivity map of the coil, $\mathbf{c}_l$. If the coils have

[1] This chapter based primarily on work found in [67]

distinct sensitivity patterns, then that spatial sensitivity information can be used to help form an unaliased image from the undersampled data. In the traditional SENSitivity Encoding (SENSE) formulation [38], Cartesian k-space trajectories were the preferred sampling strategy because aliasing from undersampling resulted in a small number of overlapping pixels. Since unaliasing requires inversion of a matrix of size equal to the number of overlapping pixels, Cartesian trajectories allowed for fast SENSE reconstruction. For non-Cartesian trajectories all pixels in the reduced sampling image interact with the point spread functions of all other pixels in the image. Unaliasing these images requires inversion of a large matrix and, therefore, iterative methods are necessary for reconstruction. In the follow-up to their original SENSE paper, Pruessmann, *et al.* introduced a faster method to speed up computation when non-Cartesian trajectories were used [39]. They referred to their method as a reverse gridding operation and use it without analysis of accuracy. Our iterative method is easily applicable to a SENSE experiment and our computational speedups have been analyzed as seen in Section 2.3. Also, our iterative method can include field inhomogeneity and other nonidealities in the SENSE reconstruction [67].

The sensitivity encoding (SENSE) method compensates for aliasing due to undersampling by using spatial information of distinct receiver coils arranged around the object to be imaged [38, 39]. This undersampling results in shorter acquisition readout times and therefore reduces susceptibility distortions in the resulting images. This work seeks to demonstrate that including field inhomogeneity effects in the reconstruction is still beneficial for producing SENSE images that are free of field

inhomogeneity-induced distortions. We presented some preliminary results on this topic in [67] and we expand those results here.

3.2 Methods for the SENSE experiments

We used a set of four coils from Nova Medical (Boston, MA) for performing SENSE experiments. The desired full FOV and matrix size were 22 cm and 64×64, but a spiral pulse sequence with FOV of 11 cm and matrix size of 32×32 was used to acquire data with the coil array. An alternative acquisition scheme is one in which the full FOV and matrix size are specified, but a 2-shot spiral is used to collect the data. The data can then be reconstructed to a full, unaliased image for each shot. This method allows the coupling of a SENSE reconstruction with post-filtering methods, such as UNFOLD [75–77], to remove residual aliasing from the SENSE reconstructions since they would alternate with the shot. I will specifically distinguish between these two acquisition methods when necessary.

The sensitivity maps were measured by acquiring short echo time, 2-shot or 4-shot images with both the body coil and the SENSE coils. To get the sensitivity map for each coil, its full FOV coil image was divided by the magnitude of the body coil image resulting in a noisy sensitivity map. To reduce this noise and extend the sensitivity information beyond the object, a local 2-D polynomial fitting procedure was performed. For small blocks of pixels (6×6 with overlapping borders of 2) a second order polynomial was fit to regions inside a mask of the object. This polynomial was then evaluated at all points inside the 6×6 block. Only the magnitude was smoothed using this polynomial fitting procedure. The phase of the original

division was applied back to the smoothed magnitude. Although low-pass filtering the magnitude and phase images would be a simpler method, accurate SENSE reconstructions rely on the preservation of peak information in the sensitivity patterns and low-pass filtering rounds off peaks at object boundaries.

3.3 Results

3.3.1 Phantom Study

We acquired a 4-shot, short echo time data set with the body coil in order to get a relatively undistorted estimate of the field inhomogeneity map, shown in Figure 3.1. Then we acquired a 2-shot body-coil image and fully encoded surface coil images to calculate the sensitivity maps, shown in Figure 3.2. We performed a local 2-D polynomial fitting of second order in a block-wise fashion to the magnitude of the sensitivity maps, as described in Section 3.2. For the SENSE data set, we acquired a time series of 2-shot images and used the SENSE reconstruction to reconstruct an image at each shot. The aliased images from each coil can be seen in Figure 3.3. For purposes of comparison, Figure 3.4 shows images reconstructed from single-shot acquisitions with the body coil, a two-shot acquisition with the body coil, a SENSE reconstruction without field correction, and our proposed field-corrected SENSE image. Both the single-shot and two-shot reconstructions from the body coil were field-corrected iterative reconstructions. Panel a. of this figure shows the two-shot body coil image, which offers the least distorted image of all the reconstructions in this figure. The two-shot image has a short readout time, but requires two TR intervals to acquire a full image leading to reduced temporal resolution during

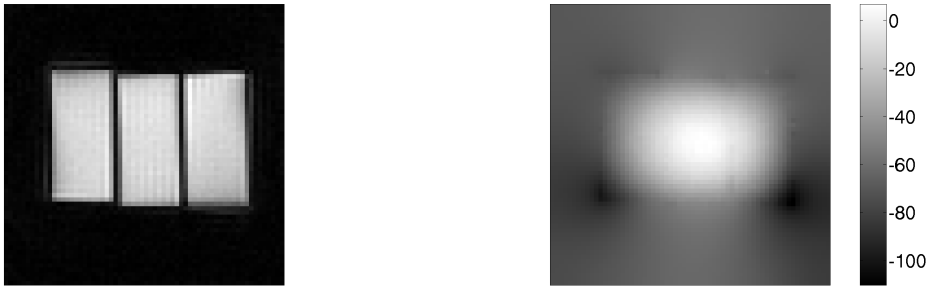

a. b.

Figure 3.1: Image and field map from 4-shot, short echo time acquisition. a.) 4-shot image. b.) 4-shot field map in Hz.

a time series. The SENSE reconstructions combine the reduced acquisition time of the two-shot sequence with the acquisition of an image in one TR interval similar to the single-shot acquisition. As shown in panels c. and d. in Figure 3.4, the SENSE reconstruction without field correction shows blurring around the edges, especially at the corners. This blurring is significantly reduced by including field-inhomogeneity terms in the SENSE reconstruction.

Figure 3.5 shows the magnitude time course for a pixel inside the object. There is an oscillation corresponding to the first-shot/ second-shot acquisition for the SENSE images, *i.e.* residual aliasing after the SENSE reconstruction that differs depending on which shot of the two-shot sequence was used. In order to reduce the variance of this oscillation, we employ methods suggested in [75–77] and apply a temporal filter to the resulting time course of images. Alternatively, we could have acquired a reduced FOV, reduced matrix size acquisition and reconstructed a full FOV and matrix size image using SENSE. The oscillation due to shot number would then be absent.

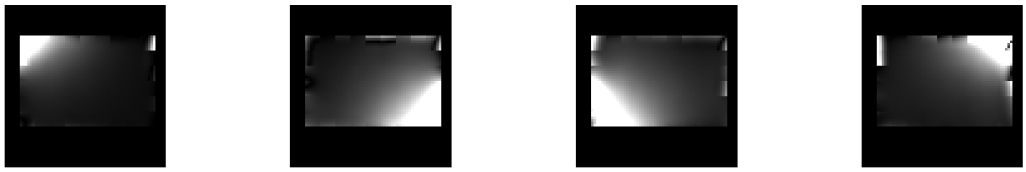

a. b. c. d.

Figure 3.2: Magnitude of the sensitivity maps from the four coils. Maps were determined by dividing coil image by body coil and local 2-D polynomial fitting. a.) Coil 1. b.) Coil 2. c.) Coil 3. d.) Coil4.

a. b. c. d.

Figure 3.3: Aliased coil images. a.) Coil 1. b.) Coil 2. c.) Coil 3. d.) Coil4.

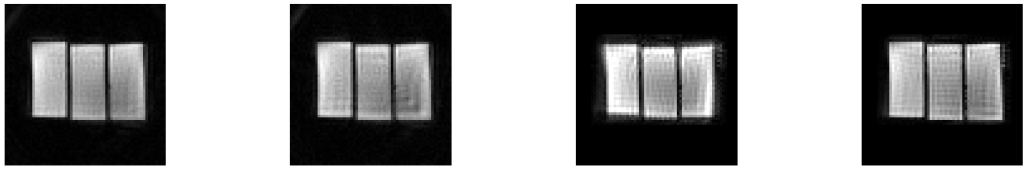

a. b. c. d.

Figure 3.4: Comparison Images. a.) Body coil 2-shot image. b.) Body coil 1-shot image. c.) SENSE reconstruction without field correction. d.) Our SENSE reconstruction with field inhomogeneity correction. SENSE reconstructions used 1-shot from a 2-shot acquisition.

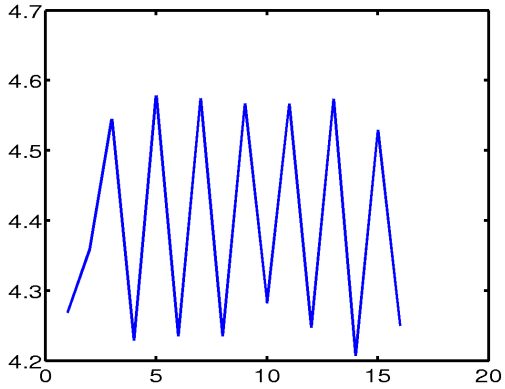

Figure 3.5: Magnitude of the time series of a point in the object. Note that the SENSE data was acquired by using a 2-shot sequence, so temporal filtering can be used eliminate this effect.

3.3.2 Human Study

The magnitude of the coil sensitivity maps for a human study are shown in Figure 3.6. The SENSE reconstructed image using our iterative method with field inhomogeneity correction is shown in Figure 3.7 along with the iterative reconstruction of a single-shot acquisition from the body coil. At the location indicated by the arrow, the single-shot image suffers from susceptibility-induced signal loss that is not present in the SENSE reconstructed image.

The acquisitions were taken as part of a bilateral finger-tapping functional study, 20 s on/ 20 s off with 4 repeats. The functional results are shown in Figure 3.8. The activation maps were formed by finding the correlation coefficient between a sinusoidal representation of the task waveform and the magnitude of the reconstructed voxel time courses. The correlation coefficient maps were thresholded at 0.6. As seen in this figure, the regions of activation in the motor cortex of the two maps are similar. The SENSE reconstruction shows residual aliasing of the task at points

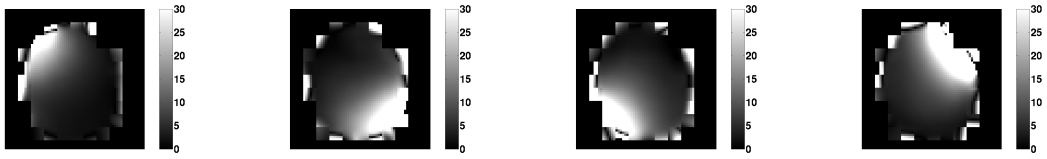

e. f. g. h.

Figure 3.6: Magnitude of the sensitivity maps for SENSE experiment. Sensitivity maps from a.) Coil 1, b.) Coil 2, c.) Coil 3, d.) Coil 4.

a. b.

Figure 3.7: a.) Single-shot image and b.) SENSE reconstruction with field inhomogeneity correction.

that are half a FOV away from the true activation. This is due to an incomplete unwrapping of the aliasing by the SENSE reconstruction, possibly from inaccurate sensitivity maps. More work needs to be done in obtaining accurate sensitivity maps.

3.4 Discussion

As shown in the phantom study in Figure 3.4, despite having shorter acquisition readouts, field inhomogeneity correction during reconstruction is still important for accurate reconstructions using SENSE. The SENSE reconstruction may be more sensitive to field inhomogeneity when Cartesian k-space trajectories are used. Recall that field inhomogeneities result in geometric distortions for Cartesian sampling of

a. b.

Figure 3.8: Functional activation maps overlayed on reconstructed images. Activation maps are from correlation coefficient map thresholded at 0.6. a.) Body coil, single-shot spiral and b.) SENSE reconstruction, half FOV and half matrix size acquisition.

k-space. This geometric distortion could interact with the undistorted coil sensitivity maps and result in additional artifact.

The human studies show that we retain high sensitivity to functional activations using SENSE acquisitions. The decrease in susceptibility-related artifacts from the shorter readouts may make it possible to study brain function in regions that are plagued with susceptibility artifacts, such as the orbital-frontal cortex and inferior temporal lobes. However, as shown in Figure 3.8, additional artifacts may appear in functional maps due to incomplete unwrapping of the aliasing pattern.

Additional work must be done to get reliable and accurate sensitivity maps. As stated in Section 3.2, we performed two-dimensional polynomial fitting on the magnitude of the sensitivity maps and did not smooth the phase. A better approach may be to formulate the sensitivity maps in a joint estimation framework using the body coil and SENSE coils data. This will be examined in our future work.

CHAPTER 4

Stability of Iterative Reconstruction

4.1 Introduction

Functional MRI (fMRI) using the blood oxygenation level dependent (BOLD) effect relies on encoding task information from regions of the brain in modulations of the amplitude of the reconstructed T_2^*-weighted images [21]. High field strengths and long readout times are desirable for functional contrast, but these same parameters make fMRI sensitive to inhomogeneities in the main magnetic field. The distortions in the images caused by the field inhomogeneities appear as geometric shifts when Cartesian k-space trajectories are used to acquire data. Blurring and signal voids result when non-Cartesian trajectories, such as spirals, are used.

Many methods have been presented to correct for field inhomogeneities when non-Cartesian trajectories are used [13, 27, 28, 30–33]. The predominant method to date has been the conjugate phase method which attempts to compensate for the phase accrual at each time point due to the field inhomogeneities. Recently, iterative reconstruction methods have been presented that provide effective field inhomogeneity correction even in regions where conjugate phase fails, *i.e.*, in regions where the field

inhomogeneity is not smoothly varying [13,33] and Chapter 2 of this thesis. In [13], the authors utilized the nonuniform fast Fourier transform (NUFFT) [35] and a min-max optimal temporal interpolation to significantly speedup reconstruction times for field-corrected iterative image reconstruction.

The conjugate phase and iterative reconstruction methods approach the image reconstruction problem in very different ways. Figure 4.1 provides a graphical depiction of the process used for both methods. In MRI, the equation for the complex baseband signal,$s(t)$, ignoring relaxation effects, is given by,

$$s(t) = \int f(\boldsymbol{r}) e^{-i\omega(\boldsymbol{r})t} e^{-i2\pi(\boldsymbol{k}(t)\cdot\boldsymbol{r})} d\boldsymbol{r}, \tag{4.1}$$

where $f(\boldsymbol{r})$ is a function of the object's transverse magnetization at location $\boldsymbol{r}$, $\omega(\boldsymbol{r})$ is the field inhomogeneity, and $\boldsymbol{k}(t)$ is the k-space trajectory. In an MR scan, the raw measurements are noisy samples of this signal,

$$y_m = s(t_m) + \varepsilon_m, \quad m = 1, \ldots, M. \tag{4.2}$$

The image reconstruction problem is to estimate the image, $f(\boldsymbol{r})$, from the noisy samples, $\mathbf{y} = y_1, ..., y_M$. For conjugate phase reconstruction, information about the field map, k-space trajectory, and sample density is used to construct an operator that acts linearly on the data to form an image. The conjugate phase reconstruction is given by,

$$\hat{f}(\boldsymbol{r}_n) = \sum_{m=0}^{M} w_m s(t_m) e^{i2\pi(\boldsymbol{k}(t_m)\cdot\boldsymbol{r}_n)}, \quad n = 1, \ldots, N, \tag{4.3}$$

where $\boldsymbol{r}_n$ are the locations where the reconstructed image is formed and w_m are the sample density coefficients, see [4,5,11] for a discussion of density compensation

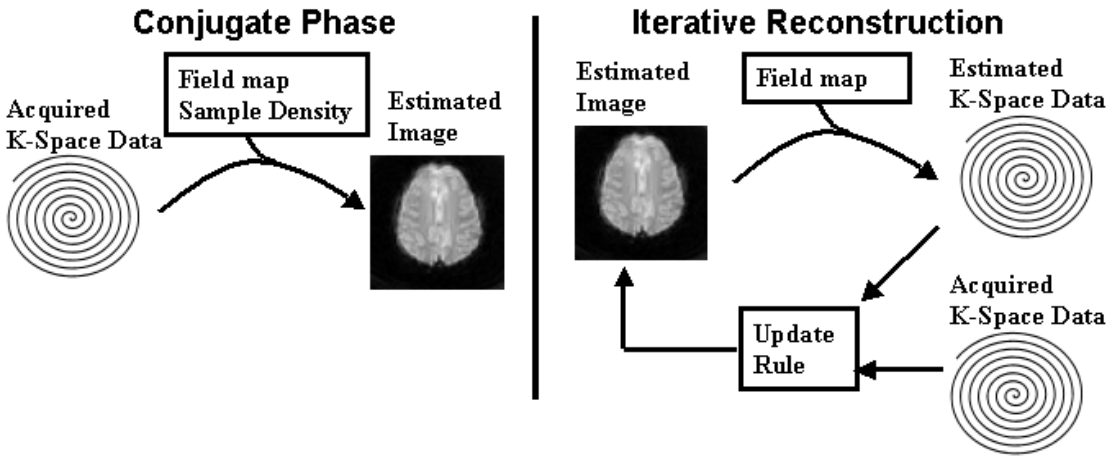

Figure 4.1: Graphical depiction of conjugate phase reconstruction vs. iterative reconstruction.

coefficients. For the iterative reconstruction, we use the signal equation for MR to simulate k-space data based on the current estimate of the image, as described in Chapter 2. This simulated data is compared with the acquired data and the estimate of the image is updated using the conjugate gradient method. Note that the iterative reconstruction method does not need sample density information.

Both the conjugate phase and iterative reconstruction methods rely on accurately measuring a field map, a map of the spatial distribution of the local off-resonant frequency. Typically, this map is estimated by acquiring two images with slightly different echo times and examining the phase differences between them [2]. The phase difference is divided by the difference in echo time to estimate the field map.

The conjugate phase reconstruction is used frequently in fMRI studies because it provides stable, field-corrected image reconstructions over the course of a time series. However, the conjugate phase method is limited by the smoothly-varying field

map assumption and relies on accurate density compensation. The iterative reconstruction method has been shown to provide accurate reconstructions even in the presence of non-smooth field maps. Yet the iterative method is a complex operation on the data and its stability properties for time series data have not been studied. In the current chapter, we show that the iterative method is stable and that the field correction algorithm does not introduce additional variance into the time series of fMRI studies. This indicates that iterative image reconstruction is both accurate and stable, making it beneficial in processing time series data from functional experiments. In Section 4.2 we describe the methods used in our analysis, including a discussion in Section 4.2.1 about matching the point spread functions of the image reconstruction methods. In Section 4.3 we give the results and Section 4.4 contains a brief discussion of these results.

4.2 Methods

A spiral out pulse sequence was used to acquire time series data for 24 slices on 6 subjects using a GE 3T Signa Scanner (GE Medical Systems, Milwaukee, WI) in accordance with the Institutional Review Board of the University of Michigan. The following parameters were used: TE/TR/FA = 30/2000 ms/90^o and field of view of 22 cm$\times$22 cm. The number of points per spiral was 3770, the matrix size was 64×64, and the first time point's echo time was delayed by an additional 2.5 ms to estimate the field map using the method presented in [2]. The field map estimate is usually smoothed to reduce noise. We performed a small amount of smoothing of the field map estimates within the object being imaged along with extending the

field map beyond the object using a penalized weighted least squares smoothing function [78]. A single field map was used for reconstructing the entire time series of images for each slice and the same field map was used for both the conjugate phase and iterative reconstructions. The subjects performed a motor task with 12 cycles of on/off bilateral finger tapping, each cycle lasting 36 sec, for a total of 216 time points acquired.

4.2.1 Normalizing and Matching Reconstruction Methods

The data was reconstructed using three methods: no field correction (a gridding reconstruction), conjugate phase reconstruction, and fast iterative reconstruction. For the fast iterative method, fifteen iterations of the conjugate gradient algorithm were performed using the NUFFT with 2 times oversampling and 6×6 neighbors and min-max optimal temporal interpolation with 8 time segments, see [13] for details. A simulation study was performed to examine if a scaling factor was needed to normalize the magnitudes of the reconstructed images. For our implementations of these algorithms, no such scaling factors were required (results not shown).

The conjugate phase method is a Fourier reconstruction and assumes that the object is band-limited, whereas the iterative reconstruction method models the continuous object with square voxels and includes quadratic spatial regularization. To eliminate differences due to the full-width at half-max (FWHM) and shape of the point spread functions from these two reconstructions, we smoothed all the reconstructed images with a Gaussian filter to 5 mm FWHM. We chose values for the regularization parameter of the iterative method, β, that resulted in a FWHM of the

PSF similar to that of the conjugate phase reconstruction before smoothing. The PSF was determined by simulating a Kronecker impulse in five locations inside the brain and adding it to the data for a slice from each subject. The reconstruction with the impulse was subtracted from the reconstruction without it and the FWHM was determined from this subtraction image [44]. A Gaussian filter was designed in the spatial-frequency domain for each reconstruction method so that the average FWHM over all six subjects at the five chosen locations was 5 mm.

4.2.2 Stability Analysis

After reconstruction and smoothing with a Gaussian filter in the spatial domain, a second order polynomial fit was removed from the time course of each pixel to compensate for any drifts in the data. A correlation coefficient for each voxel was determined by correlating the voxel's magnitude time course with a sinusoidal representation of the task waveform. The number of voxels with a normalized correlation coefficient above a threshold (activated voxels) was determined for each method for a range of thresholds.

For 5 slices containing voxels with significant correlation to the task, further processing was performed to examine the stability of the reconstructions. The task waveform was regressed out of the time course of each voxel. The variance of the task-removed time courses for all voxels inside the brain (as determined by intersecting the thresholded conjugate phase and iterative reconstructions) were averaged for each reconstruction. This was termed the residual mean variance (rmv). We performed comparisons of the rmv of the three reconstructions on all six subjects. There were

systematic differences in residual variance between subjects due to scaling differences in the magnitude images, physiological noise differences, or subject motion during the course of the study. To remove these between-subject effects from our comparison, the rmv values for each subject were normalized to that of the conjugate phase reconstruction. The other rmv values can then be seen as a fraction of the rmv value of the conjugate phase reconstruction. We also examined the mean values of the regression coefficients over activated regions for each reconstruction, using a correlation coefficient threshold of 0.5 for the activation maps. The mean regression values for the different reconstructions were normalized to that of the conjugate phase reconstruction for each subject. Using the residual mean variance and the mean regression values, we can formulate a ratio that captures the BOLD signal-to-noise ratio (SNR), as follows:

$$\texttt{BOLD SNR} = \frac{\texttt{mean regress.}}{\sqrt{\texttt{resid. mean var.}}} \tag{4.4}$$

This measure is calculated for each reconstruction for each subject. The mean and variance over all six subjects is used for the comparison of the overall performance of the reconstruction methods.

4.3 Results

The widths of the Gaussian filters in the spatial-frequency domain needed to give a 5 mm FWHM for each of the reconstruction methods is given in Table 4.1. Notice that we are using three different values of the regularization parameter β that give a FWHM of their PSF near that of the conjugate phase reconstruction.

Method	β	**Width, σ, (cm^{-1})**
No Correction	N/A	0.936
Conjugate Phase	N/A	0.937
Iterative	8	0.902
Iterative	10	0.951
Iterative	12	1.016

Table 4.1: Widths of the smoothing Gaussian filters in the spatial-frequency domain.

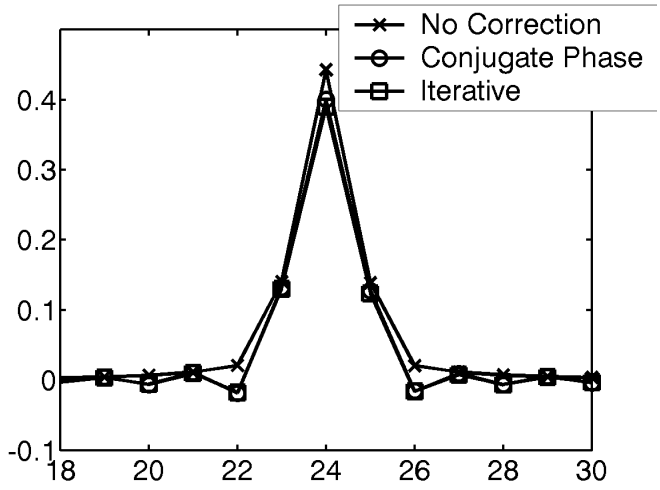

Figure 4.2: Point spread functions after smoothing with a Gaussian filter for one location in one subject. The iterative method is shown with β=10

This is seen by the fact that the widths of the filters used for the iterative methods surround the width used for conjugate phase. Figure 4.2 shows the PSF for the three reconstructions after smoothing for one location of the simulated impulse in one subject. The iterative reconstruction shown has β=10. The three reconstruction methods have similar point spread functions after smoothing.

An example image from each reconstruction method is shown in Figure 4.3 for one slice from one subject. As can be seen in this figure, the uncorrected image is blurred significantly around the edges of the brain. Both the conjugate phase and the iterative reconstruction (β=10 is shown) fix some of this distortion and result in

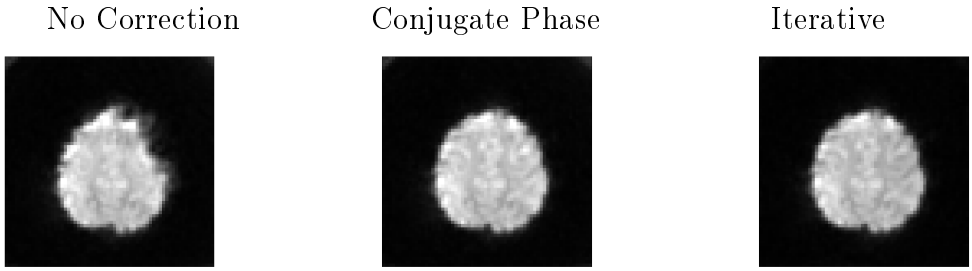

Figure 4.3: No correction, conjugate phase and iterative reconstructions from a typical slice from one subject.

similar reconstructions. The slice shown has a relatively smooth field map because it is high above the frontal sinus. Therefore, the conjugate phase and iterative reconstructions perform similarly here. If a lower slice were shown, the smoothly varying field map assumption of conjugate phase may be violated and significant improvements in field-inhomogeneity correction would result from using the iterative reconstruction, see [13,33] for examples of non-smooth field maps.

Correlation analysis was performed with the task waveform and Figure 4.4 shows functional images from one subject for the iterative reconstruction (β=10) for the 5 slices with significant numbers of task-correlated pixels. A correlation coefficient threshold of 0.6 was used for the functional overlay. The activated areas largely correspond with motor cortex. Figure 4.5 shows the number of voxels above threshold in the volume of 5 slices for a range of thresholds for each subject. The iterative and standard conjugate phase reconstructions give similar numbers of active voxels at each threshold.

In Table 4.2, we give the residual mean variance (rmv) for the three reconstructions for each of six subjects. In this table, the rmv values have been normalized by the rmv of the conjugate phase reconstruction. This table shows that the rmv of

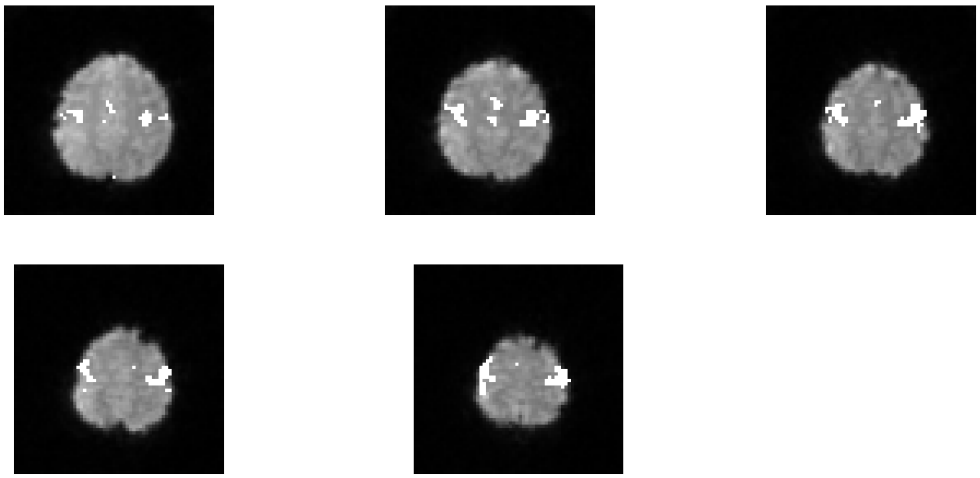

Figure 4.4: Images with functional overlay for the 5 slices examined in the study.

Method	Subj 1	Subj 2	Subj 3	Subj 4	Subj 5	Subj 6	mean	std. dev.
No Correction	0.967	0.979	0.985	0.992	0.996	0.985	0.984	0.010
Conjugate Phase	1.000	1.000	1.000	1.000	1.000	1.000	1.000	0.000
Iterative β=8	0.931	0.950	0.960	0.950	0.948	0.952	0.949	0.010
Iterative β=10	0.913	0.932	0.945	0.938	0.936	0.934	0.933	0.011
Iterative β=12	0.894	0.912	0.927	0.924	0.922	0.912	0.915	0.012

Table 4.2: Normalized residual mean variance for the three reconstruction schemes for each of six subjects.

the conjugate phase reconstruction is not significantly different from the uncorrected reconstruction. However, the iterative reconstruction is consistently below both of those reconstructions and is dependent on the regularization parameter, β. From the results in the table, one is tempted to increase the regularization parameter further. As the regularization parameter is increased beyond those used in this study, less Gaussian filtering would be needed to get a FWHM of 5 mm. This would result in a PSF whose shape differs from that of the smoothed conjugate phase, making rmv comparisons less meaningful.

Table 4.3 gives the mean value of the regression coefficients for pixels with cor-

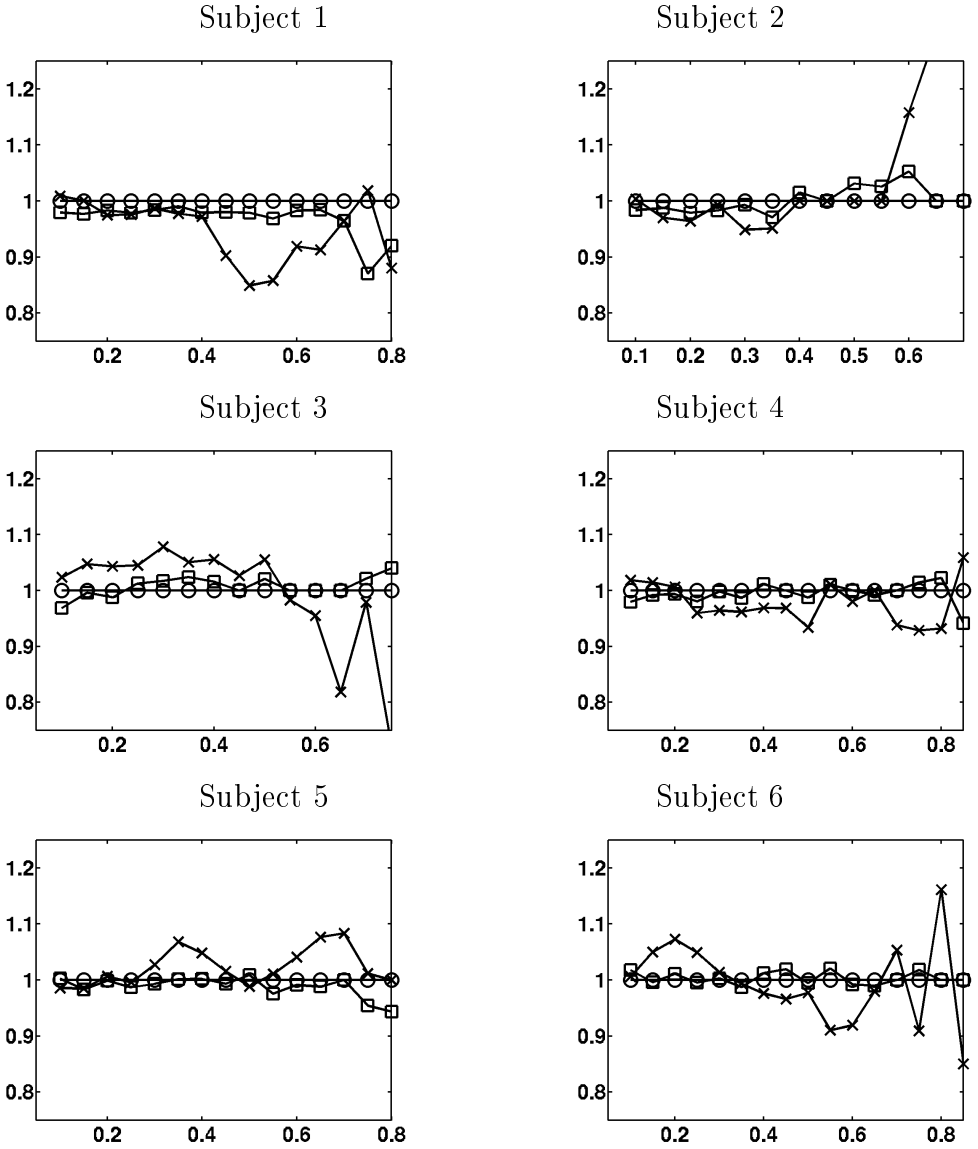

Figure 4.5: Maps of voxels above threshold vs correlation coefficient threshold for the three reconstruction methods for each of six subjects. The number of activated voxels are normalized by the number of activated voxels for the conjugate phase reconstruction. x is no field correction, circle is conjugate phase, and square is the iterative reconstruction.

Method	Subj 1	Subj 2	Subj 3	Subj 4	Subj 5	Subj 6	mean	std. dev.
No Correction	1.020	0.977	0.913	1.024	1.009	1.003	0.991	0.042
Conjugate Phase	1.000	1.000	1.000	1.000	1.000	1.000	1.000	0.000
Iterative β=8	0.954	0.947	0.980	0.978	0.971	0.970	0.967	0.013
Iterative β=10	0.941	0.934	0.964	0.973	0.961	0.963	0.956	0.015
Iterative β=12	0.934	0.918	0.967	0.963	0.956	0.932	0.945	0.020

Table 4.3: Regression coefficients vs the sinusoidal task waveform.

Method	Subj 1	Subj 2	Subj 3	Subj 4	Subj 5	Subj 6	mean	std. dev.
No Correction	1.037	0.988	0.920	1.028	1.011	1.011	0.999	0.042
Conjugate Phase	1.000	1.000	1.000	1.000	1.000	1.000	1.000	0.000
Iterative β=8	0.989	0.972	1.000	1.004	0.998	0.995	0.993	0.011
Iterative β=10	0.985	0.967	0.992	1.0004	0.994	0.996	0.990	0.013
Iterative β=12	0.988	0.962	1.004	1.002	0.996	0.976	0.988	0.017

Table 4.4: Ratios of mean of regression coefficients divided by the square root of the residual mean variance.

relation coefficients above 0.5. The regression coefficients for each subject have been normalized to that of the conjugate phase reconstruction. As can be seen in this table, the conjugate phase and uncorrected reconstructions give higher mean regression coefficients than the iterative methods.

Combining the results from Tables 4.2 and 4.3, we can get a measure of the sensitivity of each reconstruction to the BOLD signal changes as described in Section 4.2.2 and Equation (4.4). The ratio is given in Table 4.4 for each subject and the three reconstructions and the three values of β for the iterative reconstruction. All the reconstruction methods examined give very close values for this ratio, and no significant difference exists between the iterative reconstructions and the standard conjugate phase reconstruction.

4.4 Discussion

In this chapter, we have shown the stability of field-corrected iterative image reconstruction for fMRI. In our comparisons of the three reconstruction methods, care was taken to match the width and shape of the PSF for each reconstruction by using a Gaussian filter. Various values of β for the quadratic spatial regularization of the iterative method were investigated. Values were chosen such that the FWHM of the PSF of the iterative method was similar to that of the conjugate phase method. By smoothing these with a Gaussian filter, we were better able to match the shape and width of the PSF of the iterative method to that of the conjugate phase and uncorrected methods.

In Figure 4.5, the iterative reconstruction gave a similar number of activated voxels at all threshold levels when compared to the conjugate phase reconstruction. The residual mean variance values in Table 4.2 indicate that the iterative reconstruction is stable over a time series. The rmv values for the iterative method were significantly lower than those of both the conjugate phase and uncorrected reconstructions. However, the mean regression coefficients for the iterative reconstruction were lower than those from the standard reconstruction methods. Our measure of BOLD SNR showed no significant differences between the three reconstruction methods examined over the six subjects in this study.

In regions of the brain with significant non-smooth field inhomogeneity and functional correlation with the task, we expect that the iterative reconstruction will give better results than the conjugate phase method. The iterative reconstruction is

not limited by the smoothly-varying field inhomogeneity assumption and will produce more complete artifact correction in these cases, see [13, 33]. In the present study, the uncorrected reconstruction resulted in a BOLD SNR that was not significantly different from the field-inhomogeneity-corrected reconstructions. Therefore, the gains of field-inhomogeneity artifact removal may be more apparent when examining accuracy of localization of the task region, alignment of functional results to anatomical scans, or motion correction on the time series of images.

The field maps for this study were determined using a delayed echo acquisition at the beginning of the time series. This image along with the second image in the time series were used to form the estimate of the field map. Both of these images were distorted, similar to the uncorrected image shown in Figure 4.3. Therefore, the resulting field map is also distorted and the field-corrected images suffer from this error. Additional errors in the field map estimate can result from physiologically-induced phase variations between the reference scans and subject motion between the reference scans. These are the usual problems associated with the standard field map estimation technique. More accurate field maps will decrease the residual artifacts in field corrected image reconstruction for both the conjugate phase and iterative methods [72, 79].

4.5 Conclusion

We have shown that the iterative reconstruction algorithm presented in [13] gives an accurate and stable, field-corrected image reconstruction in the presence of field inhomogeneities. In this study, the iterative method resulted in a similar number

of activated voxels compared to the conjugate phase method over a range of thresholds of correlation maps. The iterative reconstruction and standard reconstruction methods resulted in similar measures of BOLD SNR. We conclude that the iterative reconstruction method is stable for fMRI studies.

CHAPTER 5

Joint Estimation of Image, Field Map, and T_2^* Relaxation[1]

Functional imaging using blood-oxygenation level dependent (BOLD) contrast is performed by acquiring T_2^*-weighted images using gradient-echo acquisitions during task and rest [21]. The gradient-echo acquisitions typically are fast, single-shot techniques such as EPI or spirals. Single-shot techniques allow high temporal resolution and avoid the mixing of respiratory phases or subject motion between the shots in a multi-shot acquisition. However, the long readout times of single-shot acquisitions make them sensitive to magnetic field inhomogeneities that can lead to severe distortions in the images. Magnetic field inhomogeneities exist around regions where materials with different magnetic susceptibility come into contact, for example at air/tissue interfaces. When uncorrected, these effects can cause geometric distortions when EPI scans are used and blurring with spiral acquisitions. The artifacts due to field inhomogeneity can cause problems when obtaining functional results from areas near air/tissue interfaces. Spatial distortions can also degrade the accuracy of registering images from different time points for motion correction and

[1] This chapter based primarily on work submitted to *Mag. Res. Med.* and found in [73, 79]

registering functional results to anatomical scans.

In this chapter we examine a joint estimation procedure whereby the undistorted image, field map, and T_2^*-relaxation map are simultaneously estimated from an extended readout acquisition. In Section 5.1 we discuss an implementation of our algorithm to the simultaneous estimation of the image and field map from a single spiral-in/ spiral-out acquisition. In Section 5.2, we extend this joint estimation algorithm to include T_2^*-relaxation and apply it to a multi-echo spiral-out acquisition.

5.1 Joint Estimation of Image and Field Map

Many image reconstruction methods have been proposed to correct for field distortions in spiral imaging, see Section 1.4.1. There are two steps involved in most field inhomogeneity correction schemes. The first is to measure the spatial variation of the magnetic field, this is referred to as estimating a field map. The second step is to use that field map to compensate for field inhomogeneities during the reconstruction. Some methods have been presented that by-pass the first step, for example Noll *et al.* [28] use an auto-focusing criteria based on the assumption that the phase is locally smoothly varying in a field-corrected image. However, most field correction methods rely on obtaining a good estimate of the field map.

Conventionally, the field map is measured by acquiring two images at slightly different echo times and dividing their phase difference by the difference in echo times [2], see Section 1.4.2. That method assumes implicitly that all of the off-resonance phase accrual occurs at the echo time, ignoring dephasing during the data readout which may be longer than the echo time. If the images used to measure

the field map are taken with the same acquisition parameters that are to be used in the imaging study, then they are distorted by field inhomogeneities and the resulting field map suffers from the image distortions. A multi-shot, short echo time scan can be used to obtain a less-distorted field map, but such field maps require extra acquisitions and may suffer from mixing of respiratory and cardiac phases [80].

For standard field map estimation, the echo time of the two reference images must be within a few milliseconds of each other to avoid ambiguity in the field map measurement that would result from 2π phase wraps. Given that the total acquisition time for an single-shot image is tens of milliseconds, one must use two separate acquisitions (TR intervals) to acquire two images with slightly different echo times, see panel a. of Figure 5.1. Respiration-induced phase variations in the two reference images, other physiological noise, or subject motion between the two scans can lead to errors in the standard field map estimate. For example, in our scans, the center frequency of an axial slice can vary by 1 Hz depending on the position in the respiratory cycle. This could result in a phase difference of as much as $(2\pi \mathrm{TE} \times 1$ Hz)radians between the two acquisitions even in the absence of additional field inhomogeneity. This phase difference divided by the difference in echo times would induce a 15 Hz error in the field map estimate for an echo time of 30 ms and a echo time delay of 2 ms. Using the spiral-in/ spiral-out sequence along with our proposed joint estimation algorithm, we are able to estimate the field map during one TR interval. The spiral-in sequence is followed by a short rest or gap of 1 ms before the spiral-out portion of the sequence is executed. Panel b. in Figure 5.1

shows the proposed spiral-in/ spiral-out trajectory. Section 5.1.3 gives an example showing that the standard field map estimation technique is not applicable to field map estimation using the spiral-in and spiral-out images within a single acquisition.

Field maps resulting from standard estimates are usually assumed to be static over the course of the functional study because an additional scan with a delayed echo time is required. This additional scan is usually performed at the beginning or the end of a functional study. This one measured field map is used for correcting the entire time series of images. Dynamic changes in the field map for a slice can occur during the course of a functional study. These changes can be due to respiratory-cycle induced phases, main field drift, and subject motion. When field-corrected image reconstruction algorithms are used, these dynamic changes can lead to further distortions in the images for a time series. Nayak *et al.* presented a method to form standard, dynamic estimates of a low-resolution field map by delaying echo times of subsequent shots in a multi-shot experiment [81, 82]. However, these estimates are sensitive to the differences in reference images discussed in the previous paragraph, whereas the method we propose here will estimate the field map within a single acquisition.

This section describes a new way to combine the two steps used for field inhomogeneity correction used in conjunction with a certain pulse sequence. We propose to reconstruct an undistorted image and its associated, dynamic, undistorted field map from a spiral-in/ spiral-out acquisition. This method retains the time resolution and other benefits of single-shot methods while correcting for distortions caused by

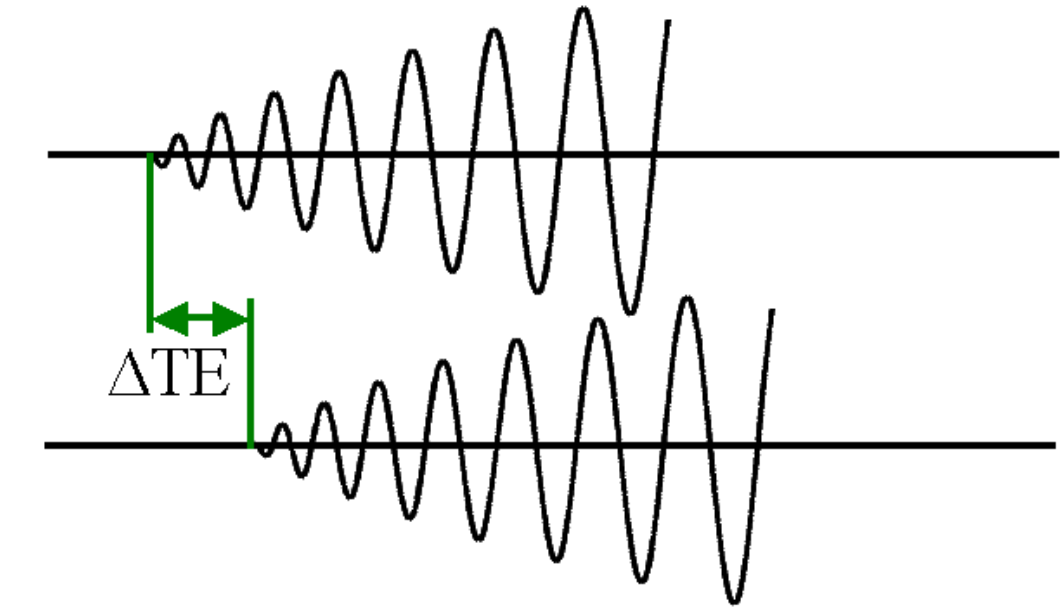

a.

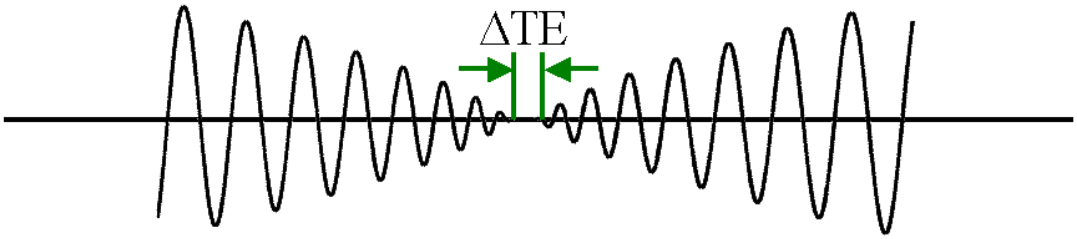

b.

Figure 5.1: Gradient Waveforms ($G_x(t)$) for the acquisition of a field map. a.) Standard field map acquisition requires two separate acquisitions to get a close spacing of echo times. b.) The spiral-in/ spiral-out sequence allows for a close sampling of echo times during a single acquisition.

the changing field map. The spiral-in/ spiral-out pulse sequence can acquire the same number of slices per TR as a spiral-out sequence [83] and therefore should not change the setup of current fMRI studies. Also, Glover and Law have reported that the presence of the spiral-in trajectory before the spiral-out trajectory does not significantly increase fluctuation noise due to motion sensitivity and no moment nulling was required [83].

In Section 5.1.1, we derive our nonlinear least-squares joint field map and image estimation algorithm and discuss some implementation issues. Our field-inhomogeneity-corrected image reconstruction method was discussed in [13] which included methods to speed computation: time segmentation and the Nonuniform Fast Fourier Transform (NUFFT) [35]. Both of those methods are used extensively in this work. Simulation, phantom, and human data experiments are described in Section 5.1.2 with the results given in Section 5.1.3.

5.1.1 Theory: Joint Estimation of Image and Field Map

We approach the simultaneous estimation problem by forming a cost function based on the signal equation for MRI and then minimizing it over the image and field map simultaneously. Section 5.1.1 presents our cost function based on the signal equation in terms of the unknown image and field map. Section 5.1.1 discusses our minimization process.

Nonlinear Least-Squares Joint Estimation

In MRI, the equation for the complex baseband signal, ignoring relaxation effects, is given by Equation (1.26), repeated here,

$$s(t) = \int f(\boldsymbol{r}) e^{-i\omega(\boldsymbol{r})t} e^{-i2\pi(\boldsymbol{k}(t)\cdot\boldsymbol{r})} d\boldsymbol{r}, \tag{5.1}$$

where $s(t)$ is the signal at time t during the readout, $f(\boldsymbol{r})$ is a function of the object's transverse magnetization at location $\boldsymbol{r}$, $\omega(\boldsymbol{r})$ is the field inhomogeneity, and $\boldsymbol{k}(t)$ is the k-space trajectory. In an MR scan, the raw measurements are noisy samples of this signal,

$$y_m = s(t_m) + \varepsilon_m, \quad m = 1, \ldots, M, \tag{5.2}$$

and from these samples we would like to simultaneously estimate the image, $f(\boldsymbol{r})$, and the field map, $\omega(\boldsymbol{r})$.

This is clearly an ill-posed problem since there is an infinite collection of solutions, $f(\boldsymbol{r})$ and $\omega(\boldsymbol{r})$, that closely match the data $\boldsymbol{y} = (y_1, \ldots, y_m)$. We proceed by parameterizing both the object and field map in terms of basis functions as follows:

$$\begin{aligned} f(\boldsymbol{r}) &\approx \sum_{n=0}^{N-1} f_n \phi_1(\boldsymbol{r} - \boldsymbol{r}_n) \\ \omega(\boldsymbol{r}) &\approx \sum_{n=0}^{N-1} \omega_n \phi_2(\boldsymbol{r} - \boldsymbol{r}_n). \end{aligned} \tag{5.3}$$

For the results presented in this chapter, we will use the voxel indicator function: $\phi_1(\boldsymbol{r}) = \phi_2(\boldsymbol{r}) = \mathrm{rect}(r_1/\Delta_{r_1}) \cdots \mathrm{rect}(r_P/\Delta_{r_P})$ for the P-dimensional problem. This choice is natural for the object, $f(\boldsymbol{r})$, since the display device will use square areas of nearly constant luminance, but better choices for the field map, $\omega(\boldsymbol{r})$, may exist

that would allow for the modeling of within-voxel nonuniformity of the magnetic field intensity. Alternative basis functions will be explored in Chapter 6. Substituting Eq. (5.3) in Eq. (5.1), yields

$$s(t) \approx \Phi(\boldsymbol{k}(t)) \sum_{n=0}^{N-1} f_n e^{-i\omega_n t} e^{-i2\pi(\boldsymbol{k}(t)\cdot\boldsymbol{r}_n)}, \tag{5.4}$$

where $\Phi(\boldsymbol{k}(t))$ results from the Fourier Transform of $\phi(\boldsymbol{r})$, *i.e.* $\mathrm{sinc}(k_1(t)\Delta_{r_1}) \cdots \mathrm{sinc}(k_P(t)\Delta_{r_P})$.

We approach the joint estimation of image and field map in a manner similar to the image reconstruction problem in Section 2.2. We parameterize the signal equation for MRI ignoring relaxation effects for now, Equation (2.4), with the voxel indicator basis functions used in Equation (2.6). We express the noisy measured samples of this signal in matrix-vector form as follows

$$\boldsymbol{y} = \boldsymbol{A}(\boldsymbol{\omega})\boldsymbol{f} + \boldsymbol{\varepsilon}, \tag{5.5}$$

where $\boldsymbol{f}$ is the parameterized image and $\boldsymbol{\omega}$ is the parameterized field map. The entries of the $M \times N$ matrix $\boldsymbol{A}(\boldsymbol{\omega})$ are written to reflect the fact that they depend on the current estimate of the field map,

$$a_{m,n}(\boldsymbol{\omega}) = \Phi(\boldsymbol{k}(t_m)) e^{-i\omega_n t_m} e^{-i2\pi\boldsymbol{k}(t_m)\cdot\boldsymbol{r}_n}. \tag{5.6}$$

Our goal is to estimate the image, $\boldsymbol{f}$, and the field map, $\boldsymbol{\omega}$, from the k-space data $\boldsymbol{y}$, accounting for the statistics of the noise $\boldsymbol{\varepsilon}$.

In Section 2.2 and [13], we used the formulation in Eq. (5.5) as part of an inverse problem approach to field-inhomogeneity corrected image reconstruction, *i.e.* estimate the image $\boldsymbol{f}$ given the field map, $\boldsymbol{\omega}$. We showed that in regions with large

field inhomogeneity, the iterative reconstruction method results in more accurate images than the standard conjugate phase approach. However, this accuracy may be limited by errors in the estimated field map. In [13], a static field map from an additional scan was used. Due to the size of the system matrix $\boldsymbol{A}$, directly calculating its inverse is impractical and it is usually ill-conditioned. Instead, we used the iterative method of conjugate gradients (CG). The main operations involved in the CG method are computing $\boldsymbol{Ax}$ and $\boldsymbol{A}^\star\boldsymbol{y}$, *i.e.* evaluating Eq. (5.4) and a complex conjugate transpose version of that equation. We used the fast and accurate approximations of the NUFFT and time segmentation to speed the computation of these two matrix-vector products. In this work, we propose to estimate both the image and the field map and we will use both of these speed-up methods extensively.

Since the dominant noise in MRI is white Gaussian [1], we can estimate $\boldsymbol{f}$ and $\boldsymbol{\omega}$ by minimizing the following penalized least-squares cost function,

$$\begin{aligned} \Psi(\boldsymbol{f},\boldsymbol{\omega}) &= \frac{1}{2}\|\boldsymbol{y}-\boldsymbol{A}(\boldsymbol{\omega})\boldsymbol{f}\|^2+\beta_1 R(\boldsymbol{f})+\beta_2 R(\boldsymbol{\omega}) \qquad \text{so that,} \\ \hat{\boldsymbol{f}},\hat{\boldsymbol{\omega}} &= \arg\min_{\boldsymbol{f},\boldsymbol{\omega}} \Psi(\boldsymbol{f},\boldsymbol{\omega}). \end{aligned} \tag{5.7}$$

The second half of the equation for $\Psi(\boldsymbol{f},\boldsymbol{\omega})$ includes regularization terms, $R(\boldsymbol{f})$ and $R(\boldsymbol{\omega})$, that penalize the roughness of the estimated image and field map. The parameter β_1 is chosen to control noise but not to significantly affect the resolution of the problem. For the regularization of the field map, β_2 is chosen to result in a relatively smooth field map, similar to the standard field map estimates after smoothing (see Section 5.1.2). For simplicity, we used a quadratic regularization, $R(\boldsymbol{f})=\frac{1}{2}\|\boldsymbol{Cf}\|^2$ for a matrix $\boldsymbol{C}$ that takes differences between neighboring pixels.

Implementation: nonlinear estimation problem

The minimization problem, Eq. (5.7), requires an iterative algorithm. We alternate between updating $\hat{\boldsymbol{f}}$ and $\hat{\boldsymbol{\omega}}$. First we update the image given the current estimate of the field map, then we update the field map given the new estimate of the image. For updating the image, we exploit the linear relation between the image and the data and apply the iterative conjugate gradient (CG) algorithm for minimization of Eq. (5.7) over $\boldsymbol{f}$. The CG algorithm, along with the fast methods presented in [13], results in a quick convergence to the best fit image for this part of the algorithm. Once we have updated our estimate of the image, $\hat{\boldsymbol{f}}$, we use gradient descent on the cost function Ψ from Eq. (5.7) to update the estimate of the field map, $\hat{\boldsymbol{\omega}}$. The gradient of Ψ with respect to $\boldsymbol{\omega}$ is given by:

$$\begin{aligned}\frac{\partial}{\partial\omega_n}\Psi(\boldsymbol{\omega}) &= \frac{1}{2}\sum_{m=1}^{M}\Big(-it_m {f_n}^{\star}\Phi^{\star}(\boldsymbol{k}(t_m))e^{i(2\pi\boldsymbol{k}(t_m)\cdot\boldsymbol{r}_n+\boldsymbol{\omega}_n t_m)}(y_m-[\boldsymbol{A}(\boldsymbol{\omega})\boldsymbol{f}]_m) \\ &+ it_m f_n\Phi(\boldsymbol{k}(t_m))e^{-i(2\pi\boldsymbol{k}(t_m)\cdot\boldsymbol{r}_n+\boldsymbol{\omega}_n t_m)}(y_m-[\boldsymbol{A}(\boldsymbol{\omega})\boldsymbol{f}]_m)^{\star}\Big) \\ &+ \frac{\partial}{\partial\omega_n}\beta_2 R(\boldsymbol{\omega}). \end{aligned} \tag{5.8}$$

Defining g_n by,

$$g_n(\boldsymbol{\omega}) = -i\sum_{m=1}^{M} t_m {f_n}^{\star}\Phi^{\star}(\boldsymbol{k}(t_m))e^{i(2\pi\boldsymbol{k}(t_m)\cdot\boldsymbol{r}_n+\boldsymbol{\omega}_n t_m)}(y_m-[\boldsymbol{A}(\boldsymbol{\omega})\boldsymbol{f}]_m), \tag{5.9}$$

we can formulate the gradients based on the vector $\boldsymbol{g}$ given by,

$$\boldsymbol{g}(\boldsymbol{\omega}) = -iD(\boldsymbol{f}^{\star})\boldsymbol{A}^{\star}(\boldsymbol{\omega})D(\boldsymbol{t})(\boldsymbol{y}-\boldsymbol{A}(\boldsymbol{\omega})\boldsymbol{f}), \tag{5.10}$$

where $D(\boldsymbol{x})$ denotes a diagonal matrix with the elements of the vector $\boldsymbol{x}$ on its diagonal. Inserting the vector $\boldsymbol{g}$ and using our chosen regularization function $R(\boldsymbol{\omega})$,

we can express the gradient of Ψ with respect to $\boldsymbol{\omega}$ as follows:

$$\begin{aligned} \nabla_{\boldsymbol{\omega}}\Psi &= \frac{1}{2}(\boldsymbol{g}(\boldsymbol{\omega}) + \boldsymbol{g}^{\star}(\boldsymbol{\omega})) + \beta_2 C'C\boldsymbol{\omega} \\ &= \text{Real}\{\boldsymbol{g}(\boldsymbol{\omega})\} + \beta_2 C'C\boldsymbol{\omega}, \end{aligned} \tag{5.11}$$

Using the gradient in Eq. (5.11), we update our estimate of the field map, $\boldsymbol{\omega}^k$, by gradient descent,

$$\boldsymbol{\omega}^{k+1} = \boldsymbol{\omega}^k - \alpha\left(\text{Real}\{\boldsymbol{g}(\boldsymbol{\omega}^k)\} + \beta_2 C'C\boldsymbol{\omega}^k\right). \tag{5.12}$$

The step size α is chosen empirically such that the cost function, Ψ, decreases.

5.1.2 Experimental Methods for Joint Image and Field Map Estimation

In principle, one could apply the estimation method described above to any k-space trajectory. However, the quality of the results will certainly be trajectory dependent. The spiral-in/ spiral-out sequence was chosen because it provides efficient coverage of k-space and a close spacing of echo times. A spiral-in/ spiral-out pulse sequence was used in simulation, phantom, and human experiments with the following parameters: TE/FA/FOV = 30ms/60^o/24cm, Matrix size = 64×64, and a 1 ms gap between the end of the spiral-in part of the pulse sequence and the beginning of the spiral-out portion. All field-corrected image reconstructions were performed using the fast, iterative technique of [13] on the entire spiral-in/ spiral-out data. This was done so that differences in the reconstructed images can only be due to differences in the field maps and not differences in the reconstruction or regularization. The uncorrected images were reconstructed using a fast gridding operation on the spiral-in and spiral-out portions separately. The resulting images were then

combined via a square root of the average of the squares of the images. The computations of $\boldsymbol{Ax}$ and $\boldsymbol{A}^{\star}\boldsymbol{y}$ in Eq. (5.10) were carried out using the NUFFT and time segmentation algorithms described in [13, 35] with $L = 8$ for time segmentation and a 5×5 neighborhood size and two times oversampling for the NUFFT. Standard estimates for the field maps are usually smoothed to reduce noise. We performed a small amount of smoothing of the standard field map estimates within the object being imaged along with extending the field map beyond the object using a penalized weighted least squares smoothing function [78]. A single iteration of our joint estimation algorithm consisted of both an update of the image (15 iterations of CG algorithm) and the field map (4 iterations of gradient descent).

Simulation Study

Simulation data sets were formed from a high resolution brain scan with its associated field map at a matrix size of $256 \times 192 \times 128$ and then reconstructed at a lower resolution, a 64×64 matrix size for the reconstructed slice. Noise was added to the data to give an SNR ($\|\text{data}\|/\|\text{noise}\|$) of approximately 100. Two conditions were tested to ensure that the simultaneous estimation algorithm resulted in stable, accurate estimates of the field map. First, the algorithm was started with an initial estimate of the field map of zero. This was used to test if the algorithm would converge to the correct field map when starting from a distant point. Second, the algorithm was initialized with the standard estimate of the field map. Section 5.1.3 shows that the standard method cannot produce an accurate field map estimate using only the data from a single spiral-in/ spiral-out acquisition. For the standard

estimate, an additional scan had to be simulated at an echo time delayed by 2 ms. We used the average of the standard field maps from the spiral-in sequence at the two echo times and the spiral-out sequence at the two echo times as the standard field map. This convention was used both in the simulations and in the phantom and human experiments. We examined the performance of our joint estimation over iteration using the root-mean-squared (RMS) error from the true field map.

Phantom Study

Next we performed a phantom study using a GE 3T Signa Scanner (GE Medical Systems, Milwaukee, WI). Since the true field map is not known for real data experiments, we obtained a relatively undistorted estimate by acquiring two short echo time four-shot spiral-out images and used the standard field map estimation. This estimate was compared quantitatively to the estimates from the standard estimation and our joint estimation on the spiral-in/ spiral-out data. The resulting images, reconstructed using either the standard field map or the jointly estimated field map were compared qualitatively for reduction in artifact. Since our joint estimation algorithm allows us to estimate a field map for each acquisition, we applied our technique to a time series collected on the phantom using a TR of 2 s and 80 time points. We examined the time course of the field map for a pixel inside the phantom to assess the stability of our estimates.

Human Studies

The human data sets were collected on a GE 3T Signa Scanner in accordance with the Institutional Review Board of the University of Michigan. Three normal

human subjects performed a functional task consisting of 4 cycles of on/off bilateral finger tapping, each cycle lasting 40 seconds. The subjects were instructed to keep their head still during the functional studies. One human study, Subject 1, was performed with a TR of 2 s, yielding 80 time points. Two other human subjects, Subjects 2 and 3, were acquired with a TR of 0.5 s to allow for good resolution of the respiratory waveform which causes small shifts in the field map of axial slices. A respiratory bellows was used to acquire the respiratory waveform for these two subjects. Reconstructions using the dynamic, jointly estimated field maps were qualitatively compared to the reconstructions using the static, standard estimates of the field maps. Also, functional results using the time series of images reconstructed with each field map estimate were compared using the number of active voxels at a given threshold, *i.e.* the number of voxels with a correlation coefficient with the sinusoidal task waveform that exceeded a given threshold. The time series of the field map estimates were also examined for pixels inside the brain. A correlation test was performed to see if the proposed joint estimation method accurately reflected the respiration-induced phase variations.

5.1.3 Results

Simulation Study

Figure 5.2 shows the axial and sagittal slices used in the simulations and their associated field maps. Figures 5.3 and 5.4 show the root-mean square (RMS) error over iteration for the axial study and sagittal study, respectively, for both initialization conditions that were discussed in Section 5.1.2. Both of these sets of curves

show that the simultaneous estimation algorithm converges quickly, in around 50 iterations. Stability of the joint estimation method is also shown by these figures, *i.e.* when the algorithm is started with an estimate close to the local minimum, it stays near that minimum. This suggests that an efficient way to implement the simultaneous estimation algorithm for time series data is to initialize the field map at each time point with the standard, static estimate of the field map and run just a few iterations to account for dynamic changes. When initialized with the standard estimate, Figure 5.4 shows that the local minimum for the simultaneous estimation has slightly higher RMS error than the standard estimate at convergence. This is due to a local minimum. Figure 5.5 shows the map of the error in the estimate. Comparing this error to the sagittal slice in Figure 5.2, we can see that the error occurs near a peak in the field map at the edge of the object. A regularization scheme other than quadratic, such as a Huber penalty [45] or a spatially varying penalty [84], may improve estimation in those regions.

Phantom Study

A phantom data set was collected with 80 time points as described in Section 5.1.2. To estimate the field map with little field-induced distortions, we acquired an extra data set using a 4-shot spiral-out sequence with an echo time of 4.6 ms. The joint estimation algorithm was initialized at each time point with the static, standard estimate of the field map from the spiral-in/ spiral-out data and 50 iterations were performed. Figure 5.6 shows the field map estimated from this 4-shot, short echo time acquisition along with the standard and jointly estimated

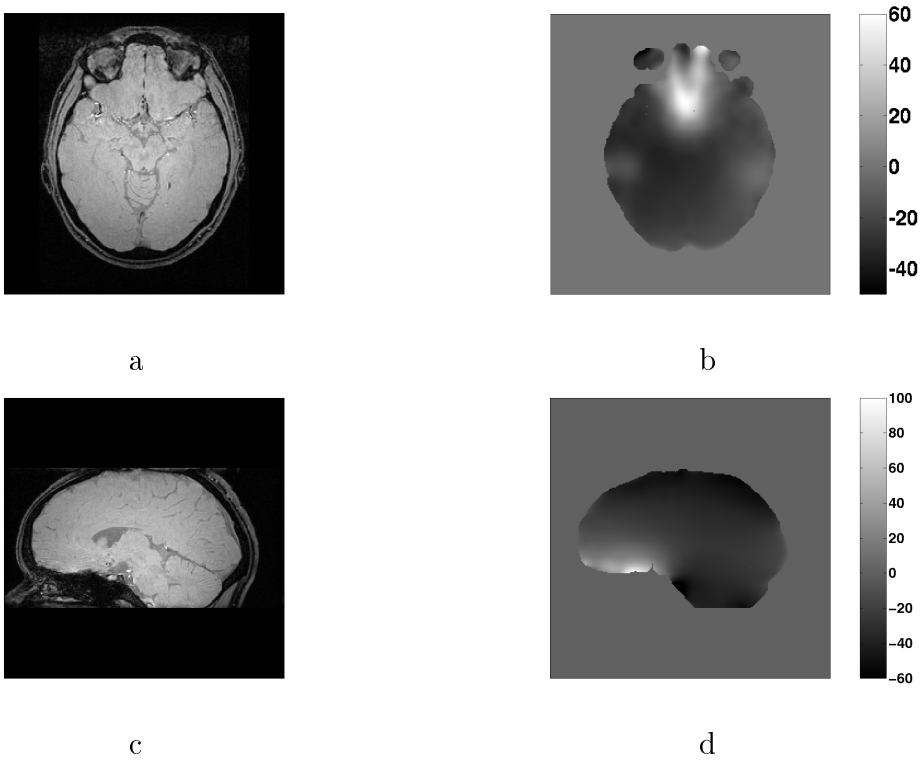

Figure 5.2: Objects used for simulation study. a.) axial slice b.) axial field map (Hz) c.) sagittal slice d.) sagittal field map (Hz)

field maps using the spiral-in/ spiral-out data. In this case, all three estimated field maps should look similar since the phantom is immobile and has no physiologically induced phase variations or motion. For this slice, we calculated root mean squared difference between the 4 shot field map and the estimated field maps over the object region as defined by the 4-shot image. The RMS difference for the standard estimate was 2.9 Hz and for the jointly estimated field map was 4.3 Hz at time point 2. Recall that the standard field map estimate is an average of the field maps determined from the spiral-in and spiral-out portions of the data at both the first and second time points in the acquisition (Section 5.1.2). However, the joint estimation used only the data from a single spiral-in/ spiral-out acquisition, although in this case, we are

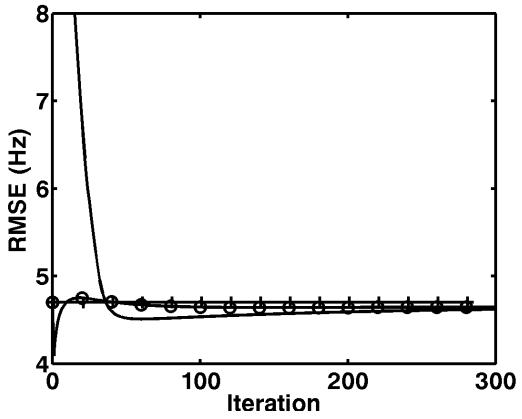

Figure 5.3: RMS error in Hz vs iteration number for the axial slice simulation. Solid line (-) is the simultaneous estimation initialized with a zero field map, Circles (o) are the simultaneous estimation initialized with the standard field map, Plus (+) is the standard field map estimate, which is not iterative but is shown as a constant value vs iteration.

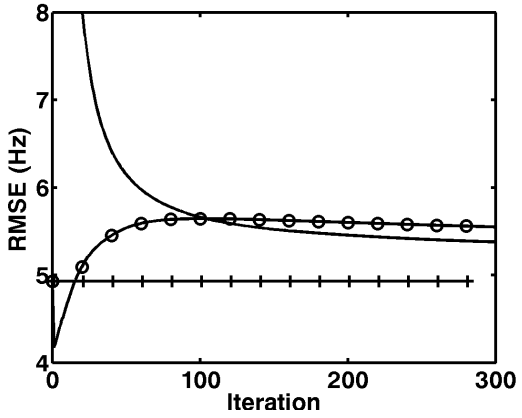

Figure 5.4: RMS error in Hz for the sagittal slice simulation. Solid line (-) is the simultaneous estimation initialized with a zero field map, Circles (o) are the simultaneous estimation initialized with the standard field map, Plus (+) is the standard field map estimate, which is not iterative but is shown as a constant value vs iteration.

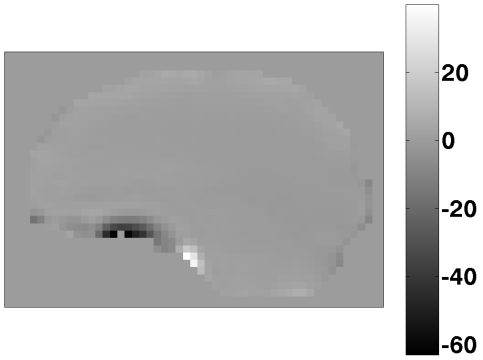

Figure 5.5: Error in Hz for the sagittal slice.

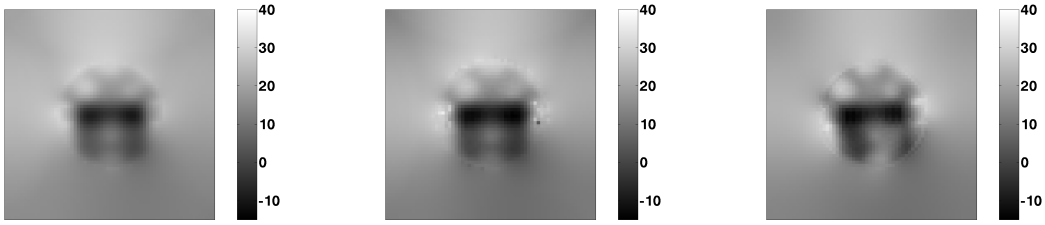

a b c

Figure 5.6: Field maps for the phantom study in Hz: a.) 4-shot short echo time spiral-out with standard field map estimation, b.) standard field map estimate c.) jointly estimated field map.

using the standard estimate to initialize the algorithm. Figure 5.7 shows the resulting images reconstructed with the 4-shot field map, the standard field map and the jointly estimated field map. Since the 4-shot image had a much shorter echo time, it has different T_2^*-weighting. The jointly estimated image and standard image result in similar reconstructions for this phantom study.

We can examine the time course of the dynamic, jointly estimated field map at a pixel of interest to study the variance of our field map estimate and identify any main field drift in the scanner. Figure 5.8 shows the time course of the field map estimate of a point in the interior of the upper region of the phantom. From this

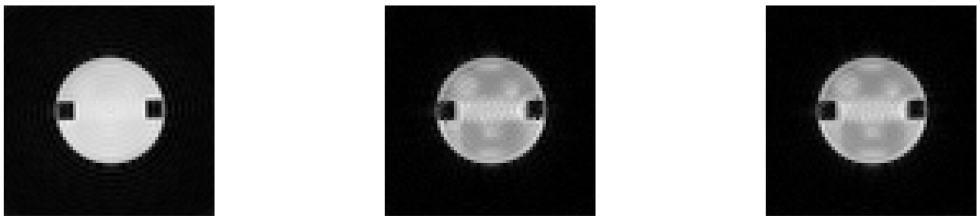

a b c

Figure 5.7: Reconstructions from phantom experiment: a.) 4-shot short echo time spiral-out, b.) spiral-in/ spiral-out using the standard field map estimate c.) spiral-in/ spiral-out using the jointly estimated field map.

plot we can see that there is a smooth drift of the main magnetic field over the course of the time series, around 2.5 Hz over the 160 s scan time. A similar drift in the field map was seen for all pixels inside the phantom. Such field drifts are seen routinely in our stability scans, possibly due to heating of the passive shim coils. If this trend was known a priori, then it could be compensated in the data processing, but the trend may depend on pulse sequence parameters, recent scan history, and environmental factors and may be hard to characterize accurately. After regressing out a second order polynomial fit to the curve, the residual standard deviation of the estimate averaged over the phantom was 0.12 Hz. Thus our estimation algorithm is fairly stable over the course of a time series and dynamic estimation allowed us to track a 1 Hz/min drift in the main field strength.

Human Study

A data set was collected during a functional experiment as described for the human study in Section 5.1.2 with a TR of 2 s and 80 time points (Subject 1). Field inhomogeneity distortions are generally worse for lower slices of the brain that are closer to the air/tissue interfaces of the sinus cavities. We show results for both

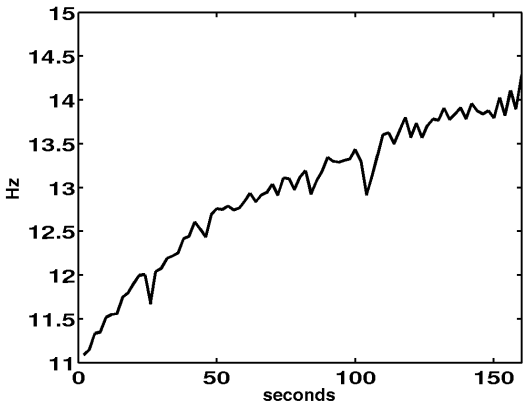

Figure 5.8: Time course of the jointly estimated field map for a pixel inside the phantom.

a slice low in the brain and a slice containing pixels with significant correlation to the motor task. Figure 5.9 shows the uncorrected image, the standard and jointly estimated field maps, and the reconstructions using those field maps for a low axial slice at the tenth time point. The T_1-weighted anatomical scan is given for reference. Although the two field maps look similar, the arrows in the reconstructed images indicate positions at which the images show differences in the degree to which inhomogeneity correction was successful. The image reconstructed with the standard field map shows blurring and signal loss at the indicated positions, whereas the increased accuracy of the jointly estimated field map allows for adequate compensation and artifact reduction.

Figure 5.10 gives the results for the field map estimations and the reconstructed images for a slice containing pixels correlated to the bilateral finger tapping task. The results for the jointly estimated image and field map are shown for the tenth time point. The standard field map differs considerably from the jointly estimated field map for this slice. Along the edge indicated by the arrow, the reconstructed image

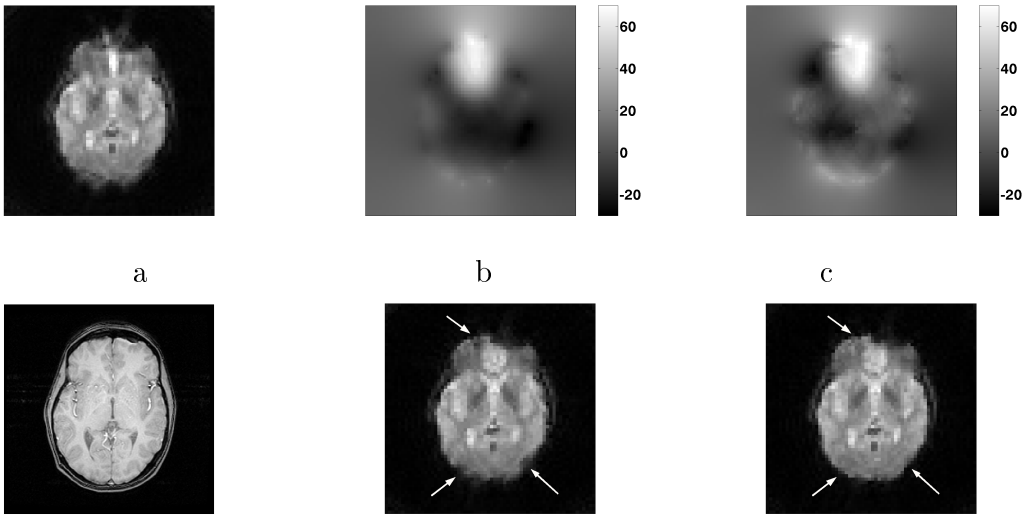

Figure 5.9: Results of reconstruction and estimation on a slice lower in the brain of Subject 1. a.) uncorrected image, b.) standard field map estimate, c.) jointly estimated field map, d.) T_1 anatomical image for reference e.) image reconstructed using the standard field map, f.) image reconstructed using the jointly estimated field map.

with the standard field map shows significant blurring due to field inhomogeneity. The jointly estimated field map and image are largely free of this distortion.

The reduced artifacts using the jointly estimated field map are also evident in the functional results. Figure 5.11 shows the functional results from reconstructions using the standard and dynamic field maps for all three human subjects examined. Panels a.-f. show the functional activation maps thresholded at a correlation coefficient of 0.5. The reference image shown under the functional map is the image reconstructed using the corresponding method. For subject 1 in panels a. and d., both methods show similar activation on the left-hand side, but only the joint-estimation method shows a comparable number of active voxels on the right-hand side. The increased bilateral detection corresponds with the increased artifact correction, see the arrow

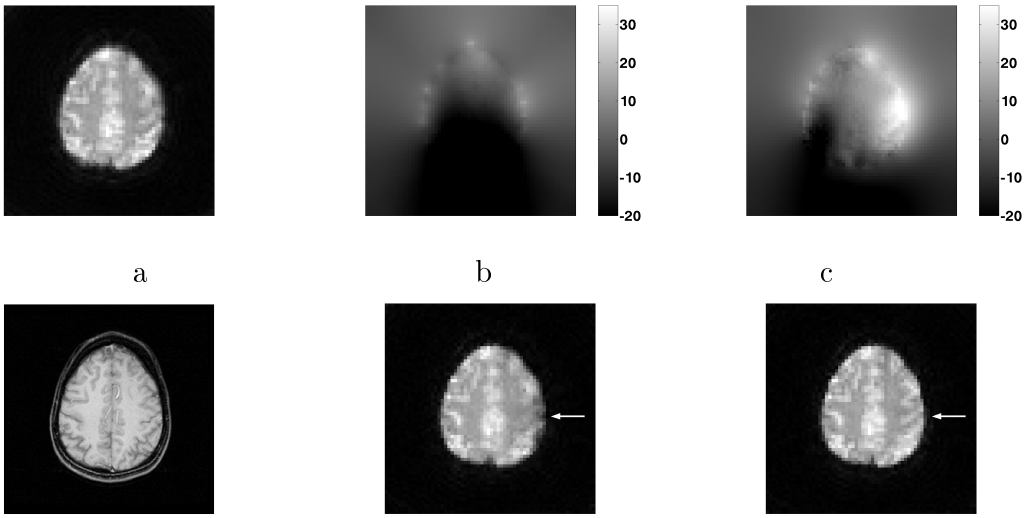

Figure 5.10: Results of reconstruction and estimation on slice of interest for functional study for Subject 1. a.) uncorrected image, b.) standard field map estimate, c.) jointly estimated field map, d.) T_1 anatomical image for reference e.) image reconstructed using the standard field map, f.) image reconstructed using the jointly estimated field map.

in Figure 5.10. Panel g. in Figure 5.11 shows the number of pixels with correlation coefficients higher than various thresholds for the two reconstructions for Subject 1. The trend seen in panels a. and d. for a threshold of 0.5 holds for all the other thresholds examined, *i.e.* a larger number of activated pixels result from correctly compensating for the undistorted, dynamic field map. Panels b. and d. in Figure 5.11 show the functional maps for Subject 2 (TR = 0.5 s) and panels c. and e. show the functional maps for Subject 3 (TR = 0.5 s). All maps were thresholded at a correlation coefficient of 0.5. Again we see with both these subjects that accurate compensation for the dynamic, jointly-estimated field map results in a larger number of activated voxels. The plots of number of active voxels versus threshold level for the two subjects are shown in panels h. and i., respectively.

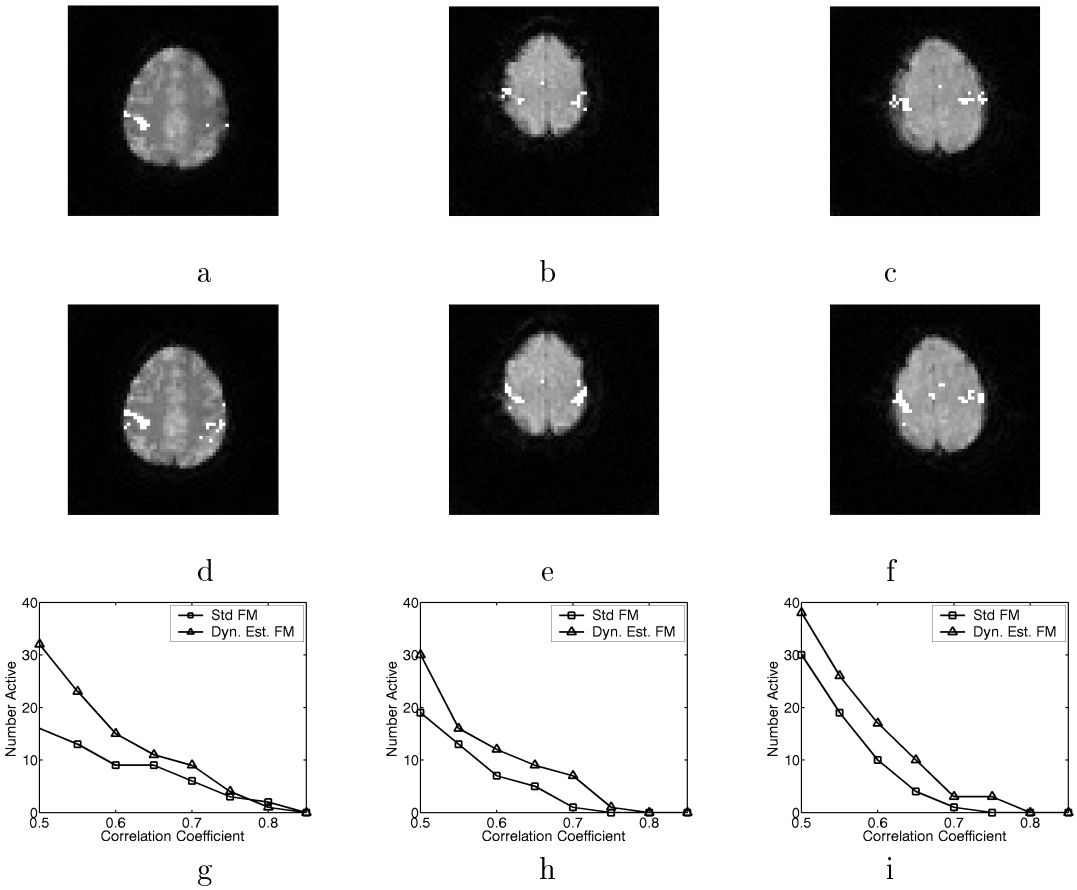

Figure 5.11: Functional results for the two reconstructions for all three human subjects. Reconstruction using the standard field map for: a.) Subject 1, b.) Subject 2, c.) Subject 3. Reconstruction using the jointly estimated field map for d.) Subject 1, e.) Subject 2, f.) Subject 3. Plot of number of pixels with correlation coefficients higher than the threshold for various thresholds for g.) Subject 1, h.) Subject 2, i.) Subject 3.

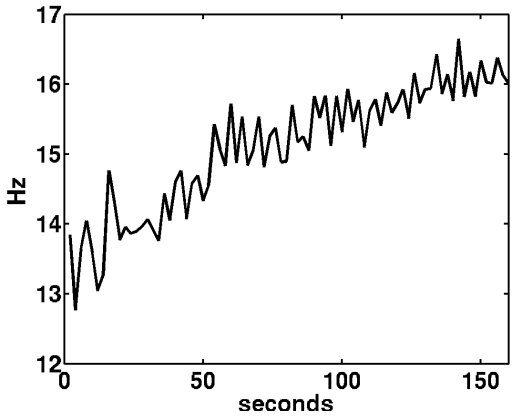

Figure 5.12: Time course of simultaneously estimated field map for a pixel within the brain.

Figure 5.12 shows the estimated field map for a voxel inside the brain over the the course of the functional study for Subject 1. A field drift over the course of the time series exists in the human data that is similar to that from the phantom scan, a positive shift in the field of about 2.5 Hz over the course of the scan. The field map estimates here have higher oscillations than in the phantom study. Regressing out a second order polynomial fit to the time course shown in Figure 5.12 gives a residual standard deviation of 0.33 Hz, averaged over the brain.

The higher variance in the time series of the field map from the human study vs the phantom study (Figure 5.12 vs. 5.8) could be due to respiration-induced field changes during the course of the time series. To examine this effect further, two of the subjects were scanned with a TR of 0.5 s to allow for good resolution of the respiratory effect and a respiratory bellows was used to acquire the respiration waveform, as described in Section 5.1.2. We performed a correlation analysis between the measured respiratory waveform and that from the time course of the estimated field map after regressing out a second order polynomial fit to remove the main

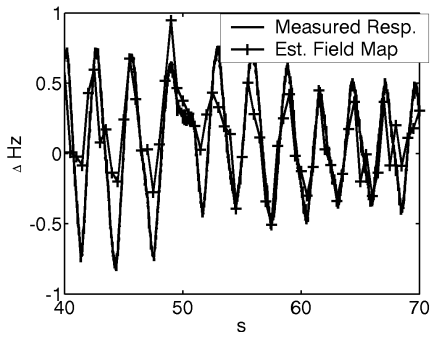

Figure 5.13: Plot of time course of field map for a pixel inside the brain of Subject 3 after regressing out a second order polynomial fit to remove the main field drift component. Shown also for reference is a scaled version of the waveform measured from the respiratory bellows.

field drift component. We found that for Subject 2, there was a mean correlation coefficient of 0.39 over the brain region between the field map values (after removing a second order polynomial fit) and the respiratory waveform. For Subject 3, the mean correlation coefficient over the brain was 0.43. A plot of the time course of the field map for a pixel inside the brain of Subject 3 is shown in Figure 5.13. This pixel was near the center of the brain and had the highest correlation coefficient with the respiratory waveform, 0.80. Also shown in this figure for reference is a scaled version of the respiratory waveform as measured from the respiratory bellows. The variations in the field map values are a good fit to the scaled measurements from the respiratory bellows.

Non-iterative Dynamic Estimation

At first glance, it might appear that a dynamic field map estimate could be formed by first reconstructing uncorrected images from the spiral-in and spiral-out parts of the sequence separately. These acquisitions were spaced by 1 ms in our studies, so the field map could be formed by taking the phase difference of these two

images and dividing by the difference in echo times. Figure 5.14 shows the field maps estimated in this manner for the simulation and phantom experiments. These field maps have shapes that are fairly consistent with the truth (refer to Figures 5.2 and 5.6), but the scaling is wrong, even resulting in phase wraps in the field map. The problem with this non-iterative dynamic method is that the point spread function of a spiral-in sequence with field inhomogeneity differs greatly from that of a spiral-out acquisition. A possible explanation is offered in [34]: gradients in the field map distort the local k-space trajectory which may cause a shift in the timing of the sampling of the center of k-space, the effective echo time, that may differ greatly from the planned echo time. In the usual case, when comparing spiral-out sequences of the same slice at two different echo times, this effective echo time shift is the same for both, keeping the difference in effective echo times the same as the planned echo time delay. However, the time at which the origin of k-space is sampled for spiral-in and spiral-out sequences is affected differently by gradients in the field map. This results in an effective difference in echo time between the spiral-in and spiral-out sequences that varies spatially. Hence, in addition to the usual problems associated with the standard field map estimate discussed in the beginning of this chapter, the field map estimates are also degraded by a space-variant scale factor.

5.1.4 Discussion

The simulation studies show that our joint estimation technique can estimate a field map that is similar in accuracy to the standard field map estimate. The standard field map estimate requires two acquisitions at slightly different echo times

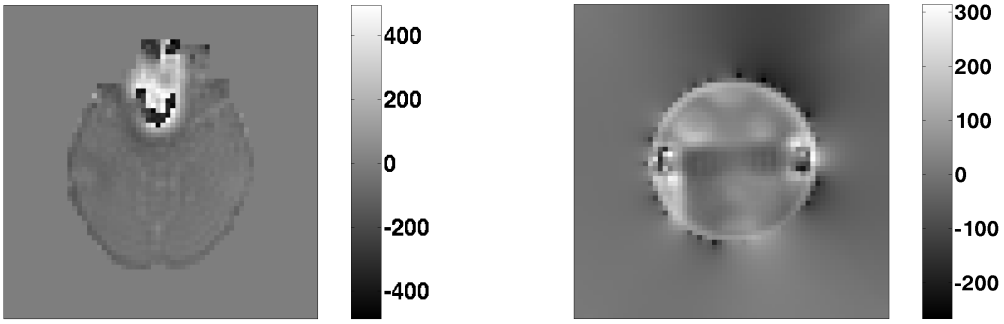

a b

Figure 5.14: Field maps estimated from the phase differences of spiral-in and spiral-out images reconstructed separately. a.) simulation field map (Hz), b.) phantom field map (Hz).

and assumes that the field map remains static over the course of a time series. Our joint estimation technique uses a spiral-in/ spiral-out sequence to estimate an undistorted field map and image at each acquisition. This dynamic estimate was formed using a penalized, least-squares joint-estimation algorithm and a spiral-in/ spiral-out acquisition, which does not decrease the scan efficiency from a spiral-out sequence.

The jointly estimated field map is very stable. For each time point, the dynamic estimation is started with the static, standard estimate of the field map from the first two time points and an initial estimate of zeros for the image. That means that each time point is initialized with the same image and field map and is not dependent on the time points around it. So, by looking at the variance in the time series of the estimated field maps, we can examine the stability of the estimations. In the phantom experiment, the average standard deviation for the time course of the field map was only 0.12 Hz after removing trends to account for the drift of the

magnetic field. The mean standard deviation from the human results was 0.33 Hz. This higher variation resulted from respiration-induced phase variations during the time series. The time series of pixels inside the brain in a slice from two subjects exhibited significant correlation with the respiratory waveform as measured with a respiratory bellows. A mean correlation coefficient of 0.4 was observed for the time course of the field map with the measured respiratory waveform in a slice high in the brain in two subjects. This respiration effect should be even greater for slices lower in the brain.

For this work, the accurate measurement of respiratory effects in the time course of the field map attests to the stability and sensitivity of our method. In subsequent work, the ability of our proposed method to accurately estimate and correct for respiratory noise should be compared to other physiological noise correction schemes. For example, a technique called "dynamic off-resonance in k-space" or DORK assumes that respiration-induced phase is constant over the slice [85]. This assumption essentially restricts the application of DORK to axial slices. Although our method does use spatial regularization, it does not enforce a uniform shift for the slice. Therefore, our method is applicable to any slice orientation.

Besides the fact that the proposed method is able to track dynamic changes in the field map, the human experiments suggest that our method results in a more accurate estimate of a single field map. Although the dynamic changes in the field maps over the time series were relatively small (<5 Hz), the functional results were dramatically different when using the jointly estimated field map instead of the standard field

map. The jointly estimated field map resulted in an image with less artifact and a higher number of activated voxels in the functional studies. The standard field map estimation method suffers from the use of reference images that are distorted by field inhomogeneity effects, physiologically-induced phase differences, and motion between the reference images.

The joint estimation algorithm can accurately and dynamically track and correct for changes in the field map during the course of the functional study. These changes may be due to respiration-induced phase changes, head movement, and drifts in the center frequency of the magnetic field. These effects will become even more significant at higher field strengths, so dynamic estimation of the field map may be crucial for success of fMRI at high fields. In this work, the subject was instructed to hold their head still. In patient and pediatric populations, the subject may not be able to remain still for the time required for a functional study. In these cases, dynamic field map estimation may be necessary for adequate artifact correction and proper estimation of motion-correction parameters. In our future work, we will examine the impact of dynamic field map estimation on motion correction.

Our proposed joint estimation algorithm can be used with any pulse sequence that provides adequate sampling of k-space with a diversity in echo times to give information about phase accrual. It has also been used with a four-echo spiral-out sequence to estimate the image, field map and T_2^* relaxation map [73]. The spiral-in/ spiral-out sequence was chosen for this work because it provides an efficient coverage of k-space and allows for a close spacing of echo times. Sub-sampling strategies,

such as those using variable-density spirals [81] or radial lines [82], may allow for a reduction in the acquisition time.

One drawback to the proposed method is computation time. On a 2 GHz Pentium workstation running Matlab, 50 iterations of the proposed method to estimate an image and a field map took approximately 20 minutes. Recall that one iteration of our proposed method includes 15 iterations of CG on the image and 4 iterations of gradient descent, see Section 5.1.2. Some improvement in computation time will result from optimizing the number of sub-iterations for the image and field map updates. Also, we are using steepest descent for the nonlinear problem of minimizing over the field map, a different minimization algorithm may reduce the total number of iterations required.

5.1.5 Summary

We have presented a method to accurately estimate an undistorted image and field map for each acquisition of a spiral-in/ spiral-out sequence. This method results in stable field map estimates that are able to track field drift and respiration-induced phase variations over the course of an fMRI time series. In addition to producing dynamic estimates, we have shown that our method can result in better single field map estimates in humans than the standard estimation technique, which is sensitive to differences between the reference images due to subject motion and respiration.

5.2 Estimation of T_2^*

Functional imaging using blood-oxygenation level dependent (BOLD) contrast is performed by acquiring T_2^*-weighted images using gradient-echo acquisitions dur-

ing task and rest. Macroscopic changes in tissue T_2^* result in echo time dependent changes in the magnitude of the T_2^*-weighted images. Functional maps can then be formed by correlating the magnitude deviations with task paradigms. Wennerberg et al. [86] point out that using the T_2^*-weighted images results in a functional map whose contrast-to-noise ratio depends on echo time. Posse et al. [87] discuss ways to combine data from T_2^* weighted images at different echo times to try to remove some of this dependence. The results from combinations of data at different echo times may increase statistical significance [87], but they lack a quantitative nature desirable for comparisons between subjects and experiments. The desire for quantitative information from BOLD studies has led to the use of T_2^* mapping (or the inverse of this time constant, R_2^*) as a means of detecting functional activity [86–89].

Methods to measure R_2^* on the same temporal resolution (within a single TR) and spatial resolution as standard gradient echo imaging have been proposed [86,87] using a multiple echo readout. The standard method to form the R_2^* map is to reconstruct the images at each of the multiple echo times and fit an exponential decay to the magnitude of the pixel values [87], assuming that all of the decay occurs at the echo times. The exponential fit gives an initial intensity value, $\boldsymbol{f}_o$, in addition to the R_2^* value. In this section, we will compare our joint estimation method to two standard methods: a nonlinear least-squares fitting and a linear fit to the natural log of the data. The R_2^* maps obtained in this manner can be noisy as the fit is performed on relatively few time points (*i.e.* 2 to 10).

T_2^*-weighted imaging, while sensitive to the BOLD effect, suffers from sensitivity

to macroscopic effects of R_2^* decay and magnetic field inhomogeneity. These effects cause degradations and distortions in single-shot gradient echo images, such as as spiral acquisitions. If uncorrected, the distortions in these images can affect the R_2^* and $\boldsymbol{f}_o$ estimates. Correcting these distortions can lead to more accurate gradient-echo imaging in general, and more accurate R_2^* maps for functional studies.

To account for interactions between the estimates of R_2^*, $\boldsymbol{f}_o$, and field inhomogeneities, in this section we propose to perform a regularized nonlinear least-squares joint estimation of the undistorted $\boldsymbol{f}_o$ image, R_2^* map and field map based on modeling the signal equation with these effects included. In Section 5.2.1 we present a derivation of our joint estimation algorithm. In Section 5.2.3 we will apply our simultaneous estimation method, along with the nonlinear fitting and ln-linear fitting methods, to simulation data to compare their accuracy and ability to detect changes in R_2^*. We then look at the performance on a human functional study.

5.2.1 Theory: Joint Estimation of Image, Field Map, and T_2^* Map

In this section we give the derivation of our nonlinear least-squares joint estimation algorithm and present a method to increase the speed of computation of our algorithm. This development proceeds similar to the development in Section 5.1.1.

Nonlinear Least-Squares Joint Estimation

In MRI the signal equation with T_2^*-relaxation is given by Equation (5.13), refer to (1.25)

$$s(t) = \int f(\boldsymbol{r}) e^{-(i\omega(\boldsymbol{r}) + R_2^*(\boldsymbol{r}))t} e^{-i2\pi(\boldsymbol{k}(t)\cdot\boldsymbol{r})} d\boldsymbol{r}, \tag{5.13}$$

where $s(t)$ is the signal at time t during the readout, $f(\boldsymbol{r})$ is a function of the object's magnetization at location $\boldsymbol{r}$, $\omega(\boldsymbol{r})$ is the field inhomogeneity, $R_2^*(\boldsymbol{r})$ is the R_2^* relaxation, and $\boldsymbol{k}(t)$ is the k-space trajectory. In an MR scan, the raw measurements are noisy samples of this signal,

$$y_i = s(t_i) + \varepsilon_i, \quad i = 1, \ldots, M, \tag{5.14}$$

and from these samples we would like to simultaneously estimate $f(\boldsymbol{r})$ (which is a complex-valued $\boldsymbol{f}_o$), $\omega(\boldsymbol{r})$, and $R_2^*(\boldsymbol{r})$.

This is clearly an ill-posed problem since there is an infinite collection of solutions, $f(\boldsymbol{r})$, $\omega(\boldsymbol{r})$, and $R_2^*(\boldsymbol{r})$, that exactly match the data $\boldsymbol{y} = (y_1, \ldots, y_m)$. Similar to the procedure followed for the iterative reconstruction in Section 2.2, we proceed by parameterizing the object, field map, and R_2^* map in terms of basis functions, $\phi(r)$, so that

$$\begin{aligned} f(\boldsymbol{r}) &\approx \sum_{n=0}^{N-1} f_n \phi_1(\boldsymbol{r} - \boldsymbol{r}_n) \\ \omega(\boldsymbol{r}) &\approx \sum_{n=0}^{N-1} \omega_n \phi_2(\boldsymbol{r} - \boldsymbol{r}_n) \\ R_2^*(\boldsymbol{r}) &\approx \sum_{n=0}^{N-1} \nu_n \phi_3(\boldsymbol{r} - \boldsymbol{r}_n). \end{aligned} \tag{5.15}$$

For this section, we will once again use

$\phi_1(\boldsymbol{r}) = \phi_2(\boldsymbol{r}) = \phi_3(\boldsymbol{r}) = \mathrm{rect}(\boldsymbol{r}_1/\Delta_{\boldsymbol{r}_1}) \cdots \mathrm{rect}(\boldsymbol{r}_P/\Delta_{\boldsymbol{r}_P})$ for the P-dimensional problem, the voxel indicator function. Regardless of what basis one chooses, (5.15) is only an approximation and we explore other choices of basis functions in Chapter 6.

Substituting (5.15) in (5.13), yields

$$s(t) \approx \Phi(\boldsymbol{k}(t_i)) \sum_{n=0}^{N-1} f_n e^{-(\nu_n + i\omega_n)t} e^{-i2\pi(\boldsymbol{k}(t)\cdot\boldsymbol{r}_n)}, \tag{5.16}$$

where $\Phi(u)$ results from the Fourier Transform of $\phi(\boldsymbol{r})$, *i.e.* product of $\mathrm{sinc}(u)$ functions. We express the noisy measured samples of this signal in matrix-vector form as follows

$$\boldsymbol{y} = \boldsymbol{A}(\boldsymbol{\omega}, \boldsymbol{\nu})\boldsymbol{f} + \boldsymbol{\varepsilon}, \tag{5.17}$$

where the elements of the $M \times N$ matrix $\boldsymbol{A}(\boldsymbol{\omega}, \boldsymbol{\nu})$ are written to reflect their dependence on both the parameterized field map and R_2^*-relaxation map.

$$a_{i,j} = \Phi(\boldsymbol{k}(t_i)) e^{-(\nu_j + i\omega_j)t_i} e^{-i2\pi\boldsymbol{k}(t_i)\cdot\boldsymbol{r}_j}. \tag{5.18}$$

Our goal is to estimate the image $\boldsymbol{f}$, the field map $\boldsymbol{\omega}$, and R_2^* map $\boldsymbol{\nu}$ from the k-space data $\boldsymbol{y}$, accounting for the statistics of the noise $\boldsymbol{\varepsilon}$. This will be an ill-posed problem if $N > M$, and is usually ill-conditioned even if $N \leq M$ for non-cartesian trajectories.

Since the dominant noise in MRI is Gaussian, we estimate $\boldsymbol{f}$, $\boldsymbol{\omega}$, and $\boldsymbol{\nu}$ by minimizing the following penalized least-squares cost function,

$$\begin{aligned} \Psi(\boldsymbol{f}, \boldsymbol{\nu}, \boldsymbol{\omega}) &= \frac{1}{2}\|\boldsymbol{y} - \boldsymbol{A}(\boldsymbol{\nu}, \boldsymbol{\omega})\boldsymbol{f}\|^2 + \beta_1 R(\boldsymbol{f}) + \beta_2 R(\boldsymbol{\omega}) + \beta_3 R(\boldsymbol{\nu}) \qquad \text{so that,} \\ \hat{\boldsymbol{f}}, \hat{\boldsymbol{\omega}}, \hat{\boldsymbol{\nu}} &= \arg\min_{\boldsymbol{f},\boldsymbol{\omega},\boldsymbol{\nu}} \Psi(\boldsymbol{f}, \boldsymbol{\omega}, \boldsymbol{\nu}). \end{aligned} \tag{5.19}$$

The second half of the equation for $\Psi(\boldsymbol{f})$ includes a regularization function, R, that penalizes the roughness of the estimated image, field map and R_2^* map. This regularization can be used to decrease the condition number of the image reconstruction

problem and, therefore, control noise. The parameters $\beta_1, \beta_2, \beta_3$ are chosen by examining the point spread function of the estimates [44], β must be small enough not to significantly affect the resolution of the problem for the image reconstruction and R_2^* map. However, smoother field maps are sought to improve conditioning of the joint estimation problem. Once again, a quadratic regularization has been used, $\beta R(\boldsymbol{f}) = \frac{1}{2}\|\boldsymbol{C}\boldsymbol{f}\|^2$ for a matrix $\boldsymbol{C}$ that takes differences between neighboring pixels (for simplicity $\sqrt{\beta}$ has been absorbed into $\boldsymbol{C}$).

Here, just as in Section 5.1.1, the joint estimation is split into 2 parts. First we estimate the image given the current estimates of the R_2^* and ω maps, then we update $\boldsymbol{\nu}$ and $\boldsymbol{\omega}$ given the new estimate of the image, $\boldsymbol{f}$. For the estimation of the image given R_2^* and ω, we take advantage of the linear relation between the image and the data and apply the iterative conjugate gradient (CG) algorithm for minimization of (5.19) over $\boldsymbol{f}$, taking advantage of the fast method presented in [13]. Once we have updated our estimate of the image, $\boldsymbol{f}$, we use gradient descent on the cost function Ψ from (5.19) to update the estimates of $\boldsymbol{\nu}$ and $\boldsymbol{\omega}$. The gradient of Ψ with respect to $\boldsymbol{\nu}_n$ is given by:

$$\begin{aligned}\frac{\partial}{\partial \boldsymbol{\nu}_n}\Psi(\boldsymbol{\omega},\boldsymbol{\nu}) &= \frac{1}{2}\sum_{m=1}^{M}\Big(-it_m {f_n}^{\star}\Phi^{\star}(\boldsymbol{k}(t_m))e^{i(2\pi\boldsymbol{k}(t_m)\cdot\boldsymbol{r}_n+\boldsymbol{\omega}_n t_m)}e^{-\boldsymbol{\nu}_n t_m}(y_m-[\boldsymbol{A}(\boldsymbol{\omega})\boldsymbol{f}]_m) \\ &+ it_m f_n\Phi(\boldsymbol{k}(t_m))e^{-i(2\pi\boldsymbol{k}(t_m)\cdot\boldsymbol{r}_n+\boldsymbol{\omega}_n t_m)}e^{-\boldsymbol{\nu}_n t_m}(y_m-[\boldsymbol{A}(\boldsymbol{\omega})\boldsymbol{f}]_m)^{\star}\Big) \\ &+ \frac{\partial}{\partial \boldsymbol{\nu}_n}\beta_3 R(\boldsymbol{\nu}). \end{aligned} \tag{5.20}$$

And the gradient with respect to the field map is given by:

$$\begin{aligned}\frac{\partial}{\partial \boldsymbol{\omega}_n}\Psi(\boldsymbol{\omega},\boldsymbol{\nu}) &= \frac{1}{2}\sum_{m=1}^{M}\Big(- it_m {f_n}^{\star}\Phi^{\star}(\boldsymbol{k}(t_m))e^{i(2\pi \boldsymbol{k}(t_m)\cdot \boldsymbol{r}_n + \boldsymbol{\omega}_n t_m)}e^{-\boldsymbol{\nu}_n t_m}(y_m - [\boldsymbol{A}(\boldsymbol{\omega})\boldsymbol{f}]_m) \\ &+ it_m f_n \Phi(\boldsymbol{k}(t_m))e^{-i(2\pi \boldsymbol{k}(t_m)\cdot \boldsymbol{r}_n + \boldsymbol{\omega}_n t_m)}e^{-\boldsymbol{\nu}_n t_m}(y_m - [\boldsymbol{A}(\boldsymbol{\omega})\boldsymbol{f}]_m)^{\star}\Big) \\ &+ \frac{\partial}{\partial \boldsymbol{\omega}_n}\beta_2 R(\boldsymbol{\omega}). \end{aligned} \tag{5.21}$$

which is Equation (5.8) with the R_2^*-relaxation term added

Now, if we let g_n be given by,

$$g_n = \sum_{m=1}^{M} t_m {f_n}^{\star} e^{i(2\pi \boldsymbol{k}(t_m)\cdot \boldsymbol{r}_n + \boldsymbol{\omega}_n t_m)}e^{-\boldsymbol{\nu}_n t_m}(y_m - [\boldsymbol{A}(\boldsymbol{\omega},\boldsymbol{\nu})\boldsymbol{f}]_m), \tag{5.22}$$

we can formulate the gradients based on the vector $\boldsymbol{g}$ given by,

$$\boldsymbol{g}(\boldsymbol{\omega},\boldsymbol{\nu}) = -iD(\boldsymbol{f}^{\star})\boldsymbol{A}^{\star}(\boldsymbol{\omega},\boldsymbol{\nu})D(\boldsymbol{t})(\boldsymbol{y} - \boldsymbol{A}(\boldsymbol{\omega},\boldsymbol{\nu})\boldsymbol{f}) \tag{5.23}$$

we can express the gradient of Ψ with respect to $\boldsymbol{\omega}_n$ and $\boldsymbol{\nu}_n$ as follows:

$$\begin{aligned}\nabla_{\boldsymbol{\omega}}\Psi &= \frac{1}{2}(\boldsymbol{g}(\boldsymbol{\omega}) + \boldsymbol{g}^{\star}(\boldsymbol{\omega})) + \beta_2 C' C\boldsymbol{\omega} \\ &= \text{Real}\{\boldsymbol{g}(\boldsymbol{\omega},\boldsymbol{\nu})\} + \beta_2 C' C\boldsymbol{\omega}, \end{aligned} \tag{5.24}$$

and

$$\begin{aligned}\nabla_{\boldsymbol{\nu}}\Psi &= \frac{1}{2}(i\boldsymbol{g}(\boldsymbol{\nu}) - i\boldsymbol{g}^{\star}(\boldsymbol{\nu})) + \beta_2 C' C\boldsymbol{\nu} \\ &= -\text{Imag}\{\boldsymbol{g}(\boldsymbol{\omega},\boldsymbol{\nu})\} + \beta_3 C' C\boldsymbol{\nu}. \end{aligned} \tag{5.25}$$

Given the gradients in (5.24) and (5.25), we can update our estimates of the field and R_2^* maps, with a suitable choice of α, by the following,

$$\begin{aligned}\boldsymbol{\nu}^{n+1} &= \boldsymbol{\nu}^n - \alpha\left(\text{Real}\{\boldsymbol{g}\} + \beta C' C\boldsymbol{\nu}\right) \\ \boldsymbol{\omega}^{n+1} &= \boldsymbol{\omega}^n - \alpha\left(\text{Imag}\{\boldsymbol{g}\} + \beta C' C\boldsymbol{\omega}\right). \end{aligned} \tag{5.26}$$

The step size α is chosen empirically such that the cost function Ψ decreases.

Algorithm Speed

In the CG algorithm for the estimation of the image $\boldsymbol{f}$ and in the gradient descent for the estimation of $\boldsymbol{\nu}$ and $\boldsymbol{\omega}$, we frequently need to evaluate $\boldsymbol{A}(\boldsymbol{\omega},\boldsymbol{\nu})\boldsymbol{f}$ and $\boldsymbol{A}^{\star}(\boldsymbol{\omega},\boldsymbol{\nu})\boldsymbol{y}$, for some $\boldsymbol{f}$ and $\boldsymbol{y}$. Previously, we used the NUFFT and time segmentation to speed the computation for $\boldsymbol{A}(\boldsymbol{\omega})$. We will extend this method here to include R_2^* maps. We computed the min-max temporal interpolator for the case where R_2^* and field maps were included in the signal equation.

5.2.2 Methods

A multi-echo spiral pulse sequence with 4 echo times (TE=4.8/25.28/45.76/66.24 ms TR/FA/FOV=500ms/45/20cm, matrix size=62, 400 time points) was implemented on a GE 3T Signa scanner (GE Medical Systems, Milwaukee, WI). The first readout in the time series had echo times delayed by an additional 2.5ms in order to form a field map in the standard way, using images reconstructed from just the first spiral of the sequence at the two different echo times. This field map was used as an initial estimate in our iterative algorithm and was also used to correct the time-series images, via a time-segmented conjugate phase reconstruction [30,31], for the standard R_2^* estimations.

We used the NUFFT and time segmentation of Chapter 2 to speed up the joint estimation algorithm. The NUFFT parameters were optimized Kaiser-Bessel interpolator with two times oversampling and a neighborhood size of 5×5. The temporal interpolator used eight time segments.

5.2.3 Results

Simulation Study

An ellipsoid object was simulated with a known R_2^* and field inhomogenity to compare the three estimation methods, nonlinear least-squares, log linear fit, and simultaneous estimation. Typical values for gray and white matter R_2^* were used [90]. The resulting estimation errors for using a linear fit on the natural log of the data, a nonlinear fit using the Gauss-Newton method, and our simultaneous estimation method are shown in Figure 5.15. The simultaneous estimation method has reduced the error to around 10% in both R_2^* and $\boldsymbol{f}_o$ by the 100th iteration, which is dramatically better than the standard fit methods, especially for R_2^*. This is further seen in the R_2^* profiles in Figure 5.16, where error in the field map estimation has resulted in overestimation of R_2^*. Figure 5.17 shows the resultant estimations for the simulation study.

The target application for our proposed simultaneous estimation is to estimate R_2^* values from a time series BOLD data set. For computational efficiency, we will use the $\boldsymbol{f}_o$, R_2^*, and field maps estimated from the first time point to initialize our method on all subsequent time points. To determine how many iterations need to be run on all subsequent data points, we increased the R_2^* value on a region of pixels by 10% (from 22 to 24 1/sec) and decreased the field map in the whole image by 10% and ran the estimation on the new data set. Figure 5.18 shows the three R_2^* estimation methods for a pixel inside the R_2^* changed area and for a pixel that didn't get changed. As you can see in this figure, the simultaneous estimation

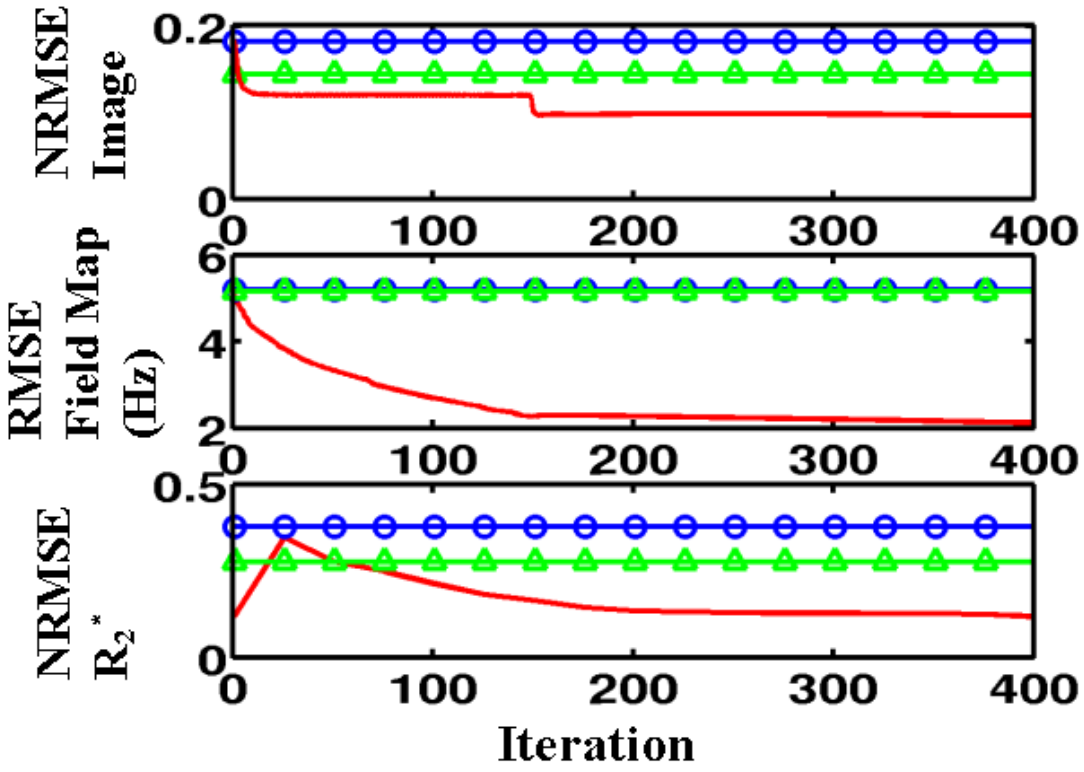

Figure 5.15: NRMSE in R_2^* and $\boldsymbol{f}_o$ maps along with RMS (in Hz) for the field map. The three estimators are shown: log linear (triangles), nonlinear (circles), and simultaneously estimated (solid line). The results from all three estimators are shown in R_2^* and $\boldsymbol{f}_o$, but both the nonlinear and log linear estimators use the standard field map estimate and its error is shown in the middle plot.

procedure accurately estimates the new value within 10 iterations. We chose to run 25 iterations on each update to account for any large changes that may take place during the course of the functional study. Note that the log-linear estimation of R_2^* resulted in underestimating both the changed and unchanged pixels, but did reflect the 10% change in pixel value.

Human Study

A human study was performed according to the paradigm explained in Section 5.2.2. A correlation analysis was performed between the timecourses of each pixel and the task paradigm (block) waveform. The task paradigm was shifted by 5 s to account for the delay in the onset of the BOLD response. The results of the correlation analysis are shown in Figure 5.19 for the log linear R_2^* estimation, the nonlinear R_2^* estimation, the T_2^*-weighted magnitude images from the second and third echos and the simultaneously estimated R_2^* map. The number of activated pixels is given in the title of each image and the simultaneously estimated $\boldsymbol{f}_o$ image is given for reference. The pixel timecourse of the three R_2^* estimation methods is shown in Figure 5.20 for an activated pixel. The estimates given by the standard methods are significantly higher than that given by our simultaneous estimation method. This could be due to the R_2^* decay compensating for error in the field map correction. Notice also that the variance of the standard estimators is higher than that for our simultaneous estimation method. We quantified this variance by regressing out the task waveform and finding the variance of the residual signal. We summed these variance in each pixel inside a mask of the image from the second echo. The values for the variance are 2.6 for log linear fit, 1.7 for the nonlinear fitting and 1.3 for the simultaneous estimation of R_2^*. Our variance is 23% lower than that of the nonlinear fitting procedure.

5.2.4 Discussion

Our regularized nonlinear least-squares joint estimation method shows increased accuracy in determining R_2^*, field map, and $\boldsymbol{f}_o$. The method uses the whole time-course of the k-space acquisition and models the signal equation using current estimates of the parameters. This will aid in accurate quantitation and detection of BOLD R_2^* modulation.

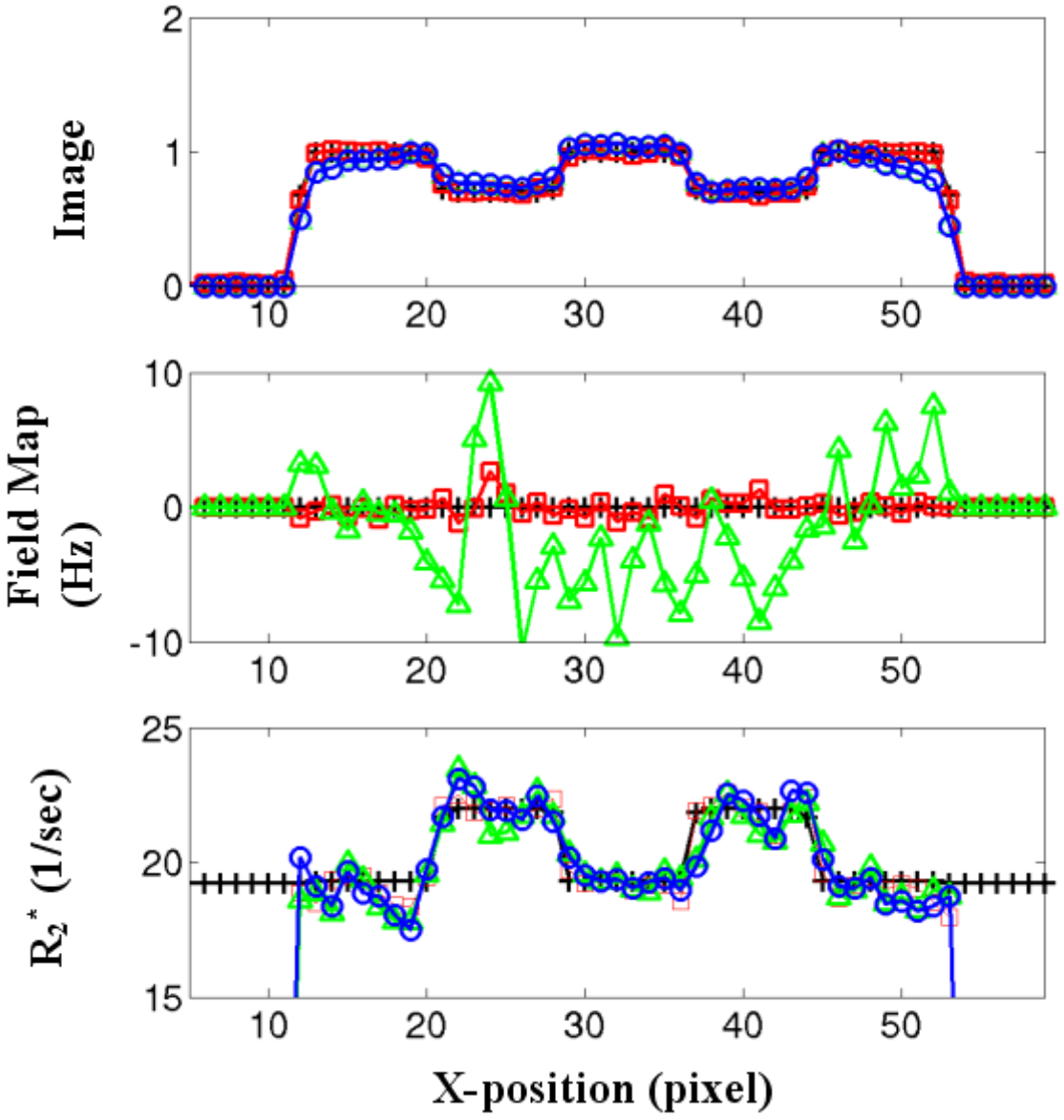

Figure 5.16: Profiles from the simulation study for a horizontal line through the simulated object, field map, and R_2^* map. The three estimators are shown: log linear (green triangles), nonlinear (blue circles), and simultaneously estimated (red square).

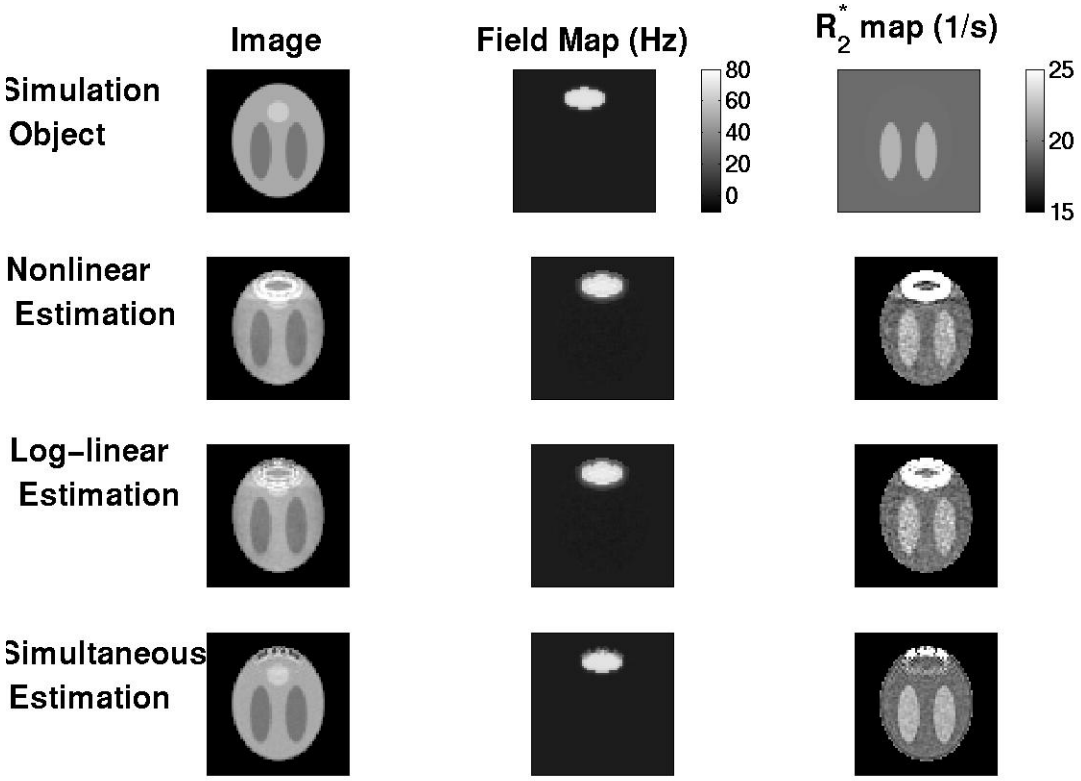

Figure 5.17: Result in $\boldsymbol{f}_o$ R_2^* and field maps from the simulation study for all three estimators. The images, field, and relaxation maps are scaled the same for each estimation method. Colorbar is given only for the simulation objects.

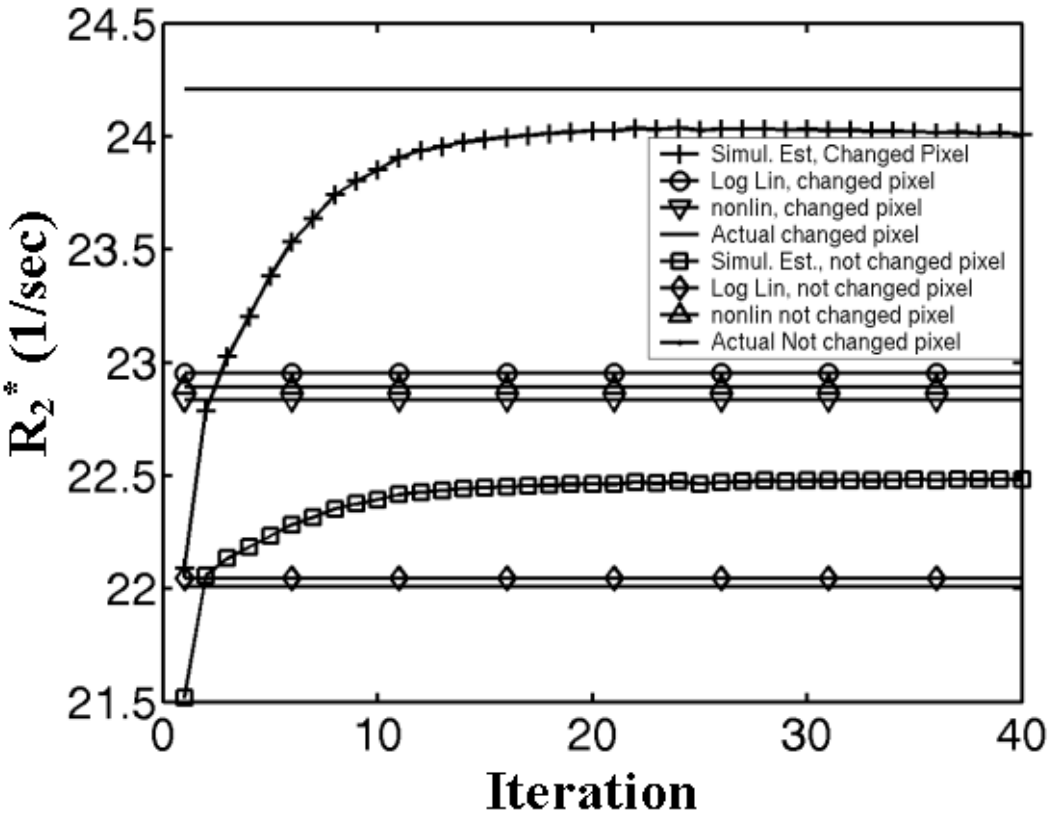

Figure 5.18: Estimation of R_2^* values for two pixels, one was changed from 22 to 24.2 1/sec and the other pixel remained unchanged. The simultaneous estimation method accurately estimates both values.

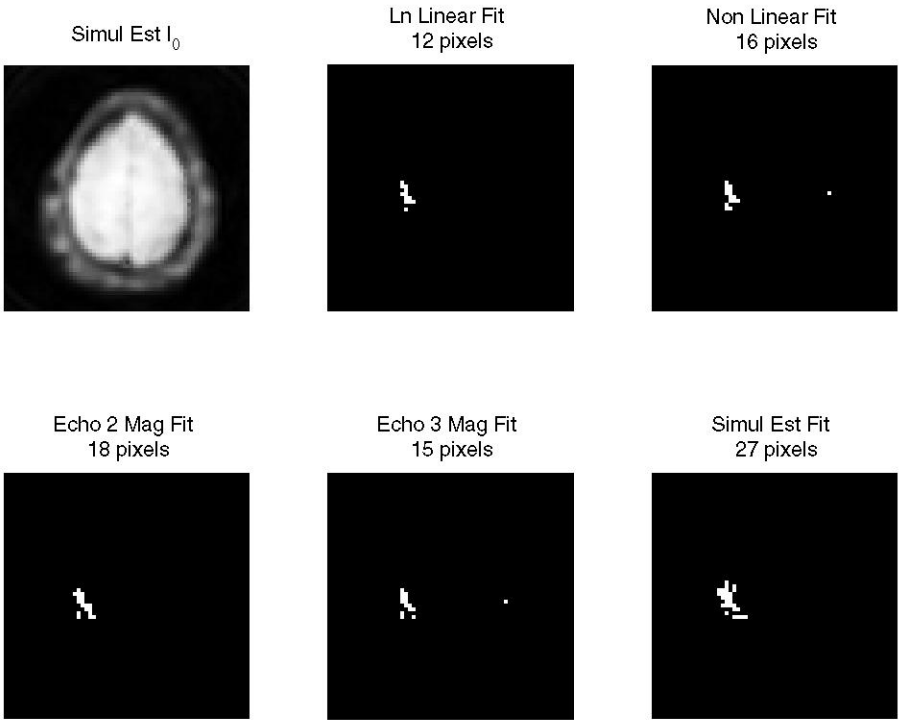

Figure 5.19: Correlation maps of timecourses correlated with the task waveform (block paradigm) using a threshold of 0.5. Shown is the simultaneous estimated $\boldsymbol{f}_o$ for reference. Correlation maps are shown for the log linear, nonlinear estimation procedures, the magnitude images from the second and third echos, and the simultaneously estimated R_2^* map.

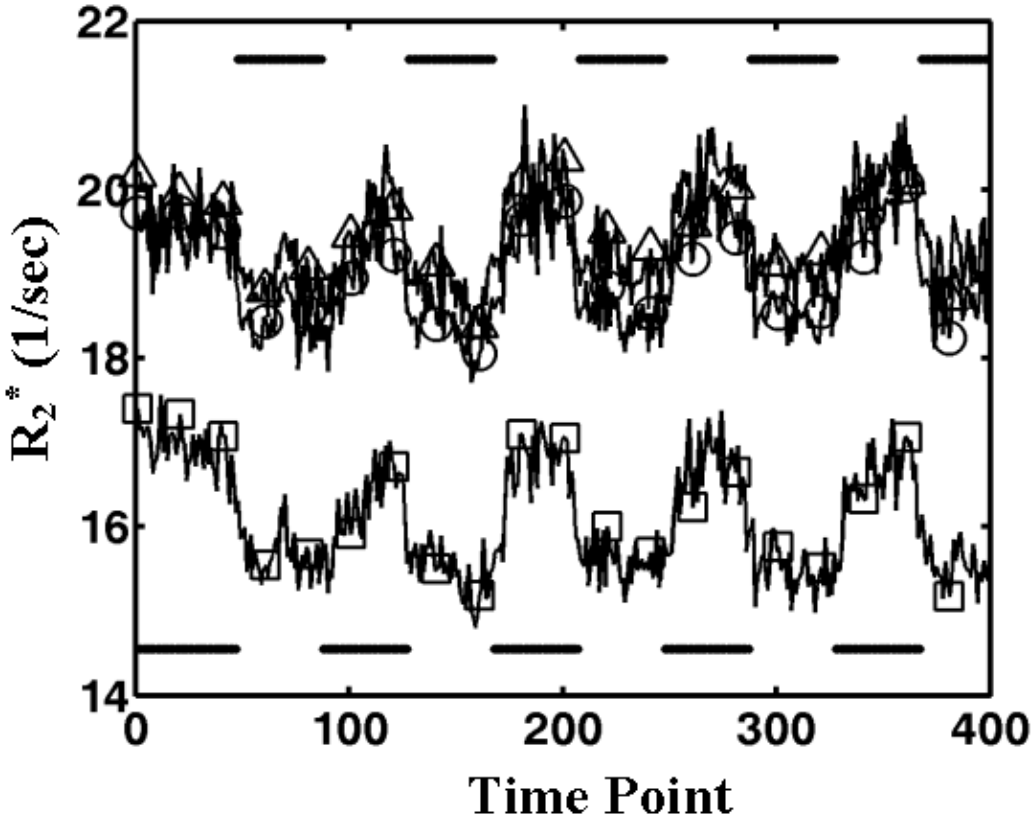

Figure 5.20: R_2^* estimated time courses for the log linear (triangles), nonlinear (circle), and simultaneously estimated (squares). Note that both standard methods estimate higher R_2^* values than the iterative method.

CHAPTER 6

Through Voxel Gradients

6.1 Introduction

In Chapter 2 we parameterized the image and field map with the voxel indicator or "rect" function. This choice is shown graphically in panel a. of 6.1. Although this choice makes sense for the image as it will be displayed as voxels, better choices for the parameterization of the field map exist. By modeling the first-order gradient of the field map between voxels, we can account for some intravoxel dephasing that would otherwise lead to apparent signal loss. Of the possible parameterizations of the object that would include first-order gradient terms, "triangle" basis functions seem like a logical choice. This parameterization is shown graphically in panel b. of Figure 6.1. However, this parameterization of the field map is complicated and does not appear to offer a computationally feasible solution, see Appendix A. Instead, we pursue two alternatives to this approach that are easily included in our iterative reconstruction: piecewise linear basis functions (see panel c. in Figure 6.1 and oversampled "rect" basis functions.

This chapter begins with the continuous signal equation, Equation (2.4), and ex-

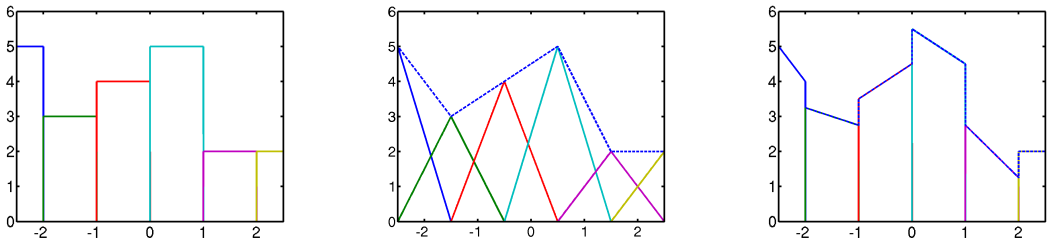

a. b. c.

Figure 6.1: Graphical representations of the basis functions explored for parameterization of the object and field map. a.) "rect" b.) "triangle" c.) piecewise linear. Dashed line for "triangle" basis function is the piece-wise linear continuous object represented by the expansion.

plores various parameterizations of the object and field map, including delta, "rect", piecewise linear, and oversampling. Results are given in Section 6.5 for a simulation and phantom study. These parameterizations can be extended to include T_2^*-relaxation maps by utilizing the complex field map notation of Chapter 5.

6.2 Theory

The two-dimensional signal equation is given in Equation (2.4) as

$$s(t) = \iint f(x,y) e^{-it\omega(x,y)} e^{-i2\pi(k_x(t)x + k_y(t)y)} dxdy, \tag{6.1}$$

where $f(x,y)$ is the object's magnetization at $t = 0$ and $\omega(x,y)$ is the inhomogeneity field map. We would like to replace the continuous time signal with a parameterized model and the continuous space integrals with summations, but we must be careful making these substitutions. To model this continuous function in space, we must discretize the signal by expanding the object and field map using a finite-series. For the object, this expansion is given by:

$$f(x,y) \approx \sum_{n=1}^{N} f_n b\left(\frac{x - x_n}{\Delta_x}, \frac{y - y_n}{\Delta_y}\right), \tag{6.2}$$

where x_n is the x-coordinate of the nth pixel, and y_n is the y-coordinate. The x_n and y_n's define a uniform Cartesian grid with spacing Δ_x and Δ_y, respectively. The basis function $b(\boldsymbol{x})$ can be a simple impulse function, a 2D "rect" function, a triangle function, or something more complicated. Plugging (6.2) into (6.1), we get the following,

$$\begin{aligned} s(t) &\approx \iint \sum_n f_n b\left(\frac{x-x_n}{\Delta_x}, \frac{y-y_n}{\Delta_y}\right) e^{-it\omega(x,y)} e^{-i2\pi(k_x(t)x+k_y(t)y)} dxdy \\ &= \sum_n f_n a_n(t), \end{aligned} \tag{6.3}$$

where

$$a_n(t) = \iint b\left(\frac{x-x_n}{\Delta_x}, \frac{y-y_n}{\Delta_y}\right) e^{-it\omega(x,y)} e^{-i2\pi(k_x(t)x+k_y(t)y)} dxdy. \tag{6.4}$$

If we let $x' = \frac{x-x_n}{\Delta_x}, y' = \frac{y-y_n}{\Delta_y}$, then $x = \Delta_x x' + x_n, y = \Delta_y y' + y_n$ and

$$\begin{aligned} a_n(t) &= \Delta_x \Delta_y \int_{x'} \int_{y'} b(x', y') e^{-it\omega(\Delta_x x'+x_n, \Delta_y y'+y_n)} \\ &\quad \cdot e^{-i2\pi(k_x(t)(\Delta_x x'+x_n)+k_y(t)(\Delta_y y'+y_n))} dx'dy' \\ &= \Delta_x \Delta_y e^{-i2\pi(k_x(t)x_n+k_y(t)y_n)} \alpha_n(t), \end{aligned} \tag{6.5}$$

where,

$$\alpha_n(t) = \iint b(x, y) e^{-it\omega(\Delta_x x+x_n, \Delta_y y+y_n)} e^{-i2\pi(k_x(t)\Delta_x x+k_y(t)\Delta_y y)} dxdy. \tag{6.6}$$

Substituting $a_n(t)$ into (6.3) we get,

$$s(t) \approx \Delta_x \Delta_y \sum_n f_n e^{-i2\pi(k_x(t)x_n+k_y(t)y_n)} \alpha_n(t). \tag{6.7}$$

Now we turn our attention to evaluating $\alpha_n(t)$. If $\omega(x, y) = 0$

$$\alpha_n(t) = B(k_x(t)\Delta_x, k_y(t)\Delta_y), \tag{6.8}$$

where $B(u,v)$ is the Fourier transform of the basis function $b(x,y)$. This gives the familiar form of the signal equation without inhomogeneity effects,

$$s(t) \approx \Delta_x \Delta_y B(k_x(t)\Delta_x, k_y(t)\Delta_y) \sum_n f_n e^{-i2\pi(k_x(t)x_n + k_y(t)y_n)} \tag{6.9}$$

Three main cases with inhomogeneity effects will be considered: an object basis of delta functions with a continuous inhomogeneity function, an object and inhomogeneity basis of "rect" functions, and an object basis of "rect" and a piecewise linear basis for the field map. The parameterization of the object and field map using a "triangle" basis function is considered in Appendix A. It is a complex analysis and does not offer a computationally feasibly solution, hence, it will not be considered here. An approximation to the piecewise linear field map will also be considered, using a high-resolution, oversampled field map with "rect" basis functions for the object and field map.

6.2.1 Object basis is delta functions

With $b(x,y) = \delta(x,y)$, (6.6) becomes,

$$\alpha_n(t) = e^{-it\omega(x_n,y_n)}. \tag{6.10}$$

Using (6.5) and plugging this back into (6.3), we get,

$$s(t) \approx \Delta_x \Delta_y \sum_n f_n e^{-it\omega(x_n,y_n)} e^{-i2\pi(k_x(t)x_n + k_y(t)y_n)}. \tag{6.11}$$

For this object model, the field map $\omega(x,y)$ can be any continuous function.

6.2.2 Object and inhomogeneity basis are "rect" functions

If $b(x,y) = \text{rect}(x,y)$ and

$$\omega(x,y) = \sum_{n'} \omega_{n'} \text{rect}\left(\frac{x - x_{n'}}{\Delta_x}, \frac{y - y_{n'}}{\Delta_y}\right) \tag{6.12}$$

then,

$$\omega(\Delta_x x + x_n, \Delta_y y + y_n) = \sum_{n'} \omega_{n'} \text{rect}(\frac{\Delta_x x + x_n - x_{n'}}{\Delta_x}, \frac{\Delta_y y + y_n - y_{n'}}{\Delta_y}). \tag{6.13}$$

From (6.6) we get the following for $\alpha_n(t)$,

$$\begin{aligned} \alpha_n(t) &= \int_{-1/2}^{1/2} \int_{-1/2}^{1/2} e^{-it \sum_{n'} \omega_{n'} \text{rect}(\frac{\Delta_x x + x_n - x_{n'}}{\Delta_x}, \frac{\Delta_y y + y_n - y_{n'}}{\Delta_y})} \\ &\quad \cdot e^{-i2\pi(k_x(t)\Delta_x x + k_y(t)\Delta_y y)} dxdy \\ &= \int_{-1/2}^{1/2} \int_{-1/2}^{1/2} e^{-it\omega_n} e^{-i2\pi(k_x(t)\Delta_x x + k_y(t)\Delta_y y)} dxdy \\ &= e^{-it\omega_n} \text{sinc}(k_x(t)\Delta_x, k_y(t)\Delta_y). \end{aligned} \tag{6.14}$$

Using (6.5) and plugging this back into (6.3), we get the approximation to the signal equation as,

$$\begin{aligned} s(t) &\approx \Delta_x \Delta_y \text{sinc}(k_x(t)\Delta_x, k_y(t)\Delta_y) \\ &\quad \cdot \sum_n f_n e^{-it\omega_n} e^{-i2\pi(k_x(t)x_n + k_y(t)y_n)}. \end{aligned} \tag{6.15}$$

This model generalizes (6.9) to account for *uniform* within-voxel off-resonance.

6.2.3 Piecewise Linear Field Map

Now we consider the following parameterization of the object and field map:

$$\begin{aligned} f(\boldsymbol{r}) &\approx \sum_{n=0}^{N-1} f_n \text{rect}(\frac{x-x_n}{\Delta_x})\text{rect}(\frac{y-y_n}{\Delta_y}) \\ \omega(\boldsymbol{r}) &\approx \sum_{n=0}^{N-1} \left(\omega_n + X_n \frac{x-x_n}{\Delta_x} + Y_n \frac{y-y_n}{\Delta_y}\right) \\ &\quad \cdot \text{rect}\left(\frac{x-x_n}{\Delta_x}\right) \text{rect}\left(\frac{y-y_n}{\Delta_y}\right), \end{aligned} \tag{6.16}$$

where ω_n is the field map value at $\boldsymbol{r}_n = (x_n, y_n)$ and X_n and Y_n are the x and y gradients of the field map at $\boldsymbol{r}_n$ in units of rad/(pixel·s). This expansion gives a piecewise linear approximation to the field map instead of the piecewise constant approximation used in (6.12). The use of triangular basis functions would give a continuous piecewise linear field map and may be a superior choice, although the analysis is more complicated, see Appendix A. Substituting (6.16) into (6.1) yields:

$$\begin{aligned} s(t) &= \sum_n f_n \iint \text{rect}(\frac{x-x_n}{\Delta_x}, \frac{y-y_n}{\Delta_y}) \\ &\quad \cdot e^{-it\sum_{n'}\left(\omega_{n'} + X_{n'}\left(\frac{x-x_{n'}}{\Delta_x}\right) + Y_{n'}\left(\frac{y-y_{n'}}{\Delta_y}\right)\right)\text{rect}\left(\frac{x-x_{n'}}{\Delta_x}, \frac{y-y_{n'}}{\Delta_y}\right)} \\ &\quad \cdot e^{-i2\pi(k_x(t)x + k_y(t)y)} dxdy \\ &= \sum_n f_n \iint \text{rect}(\frac{x-x_n}{\Delta_x}, \frac{y-y_n}{\Delta_y}) \\ &\quad \cdot e^{-it\left(\omega_n + X_n\left(\frac{x-x_n}{\Delta_x}\right) + Y_n\left(\frac{y-y_n}{\Delta_y}\right)\right)} \\ &\quad \cdot e^{-i2\pi(k_x(t)x + k_y(t)y)} dxdy. \end{aligned} \tag{6.17}$$

If we substitute $x' = (x - x_n)/\Delta_x$ and $y' = (y - y_n)/\Delta_y$

$$\begin{aligned} s(t) &= \sum_n f_n e^{-i2\pi(k_x(t)x_n + k_y(t)y_n)} \int_{-1/2}^{1/2}\int_{-1/2}^{1/2} \Big[\\ &\quad e^{-it\left(\omega_n + X_n x' + Y_n y'\right)} \\ &\quad e^{-i2\pi(k_x(t)x'\Delta_x + k_y(t)y'\Delta_y)}\Big] dx'dy' \\ &= \sum_n f_n e^{-i2\pi(k_x(t)x_n + k_y(t)y_n)} e^{-it\omega_n} \\ &\quad \int_{-1/2}^{1/2}\int_{-1/2}^{1/2} e^{-i\left[(2\pi k_x(t)\Delta_x + X_n t)x + (2\pi k_y(t)\Delta_y + Y_n t)y\right]} dx'dy' \\ &= \sum_n f_n e^{-i2\pi(k_x(t)x_n + k_y(t)y_n)} e^{-it\omega_n} \\ &\quad \mathrm{sinc}((2\pi k_x(t)\Delta_x + X_n t)/2\pi)\mathrm{sinc}((2\pi k_y(t)\Delta_y + Y_n t)/2\pi). \end{aligned} \tag{6.18}$$

Reexpressing this result as:

$$s(t) = \sum_n f_n e^{-it\omega_n} e^{-i2\pi(\boldsymbol{k}(t)\cdot\boldsymbol{r}_n)} \Phi(k_x(t), k_y(t), X_n, Y_n, t), \tag{6.19}$$

where,

$$\Phi(k_x(t), k_y(t), X_n, Y_n, t) \triangleq \mathrm{sinc}((2\pi k_x(t)\Delta_x + X_n t)/2\pi)\mathrm{sinc}((2\pi k_y(t)\Delta_y + Y_n t)/2\pi) \tag{6.20}$$

In [13], the use of voxel indicator function as the basis enabled the development of a fast iterative algorithm. The form of (6.19), however, appears to restrict the application of fast methods since the weighting function $\Phi(k_x(t), k_y(t), X_n, Y_n, t)$ depends on both spatial position and time. Trying to approximate this weighting by a time-segmented interpolation is likely to fail as the term is rapidly varying. Therefore, we will evaluate this method via a slow DFT-like summation. In the next section we

will look at an alternate approach to including sub-voxel gradients that will allow the use of the fast methods.

6.2.4 Through-Plane Gradients

Note that if through-plane gradients of the field map are included in the model, then the parameterization of (6.16) must be replaced with:

$$\begin{aligned} f(\boldsymbol{r}) &\approx \sum_{n=0}^{N-1} f_n \text{rect}(\frac{x-x_n}{\Delta_x})\text{rect}(\frac{y-y_n}{\Delta_y})\text{rect}(\frac{z-z_n}{\Delta_z}) \\ \omega(\boldsymbol{r}) &\approx \sum_{n=0}^{N-1} \left(\omega_n + X_n\frac{x-x_n}{\Delta_x} + Y_n\frac{y-y_n}{\Delta_y} + Z_n\frac{z-z_n}{\Delta_z}\right) \\ &\quad \cdot\text{rect}\left(\frac{x-x_n}{\Delta_x}\right)\text{rect}\left(\frac{y-y_n}{\Delta_y}\right)\text{rect}\left(\frac{z-z_n}{\Delta_z}\right), \end{aligned} \tag{6.21}$$

where Δ_z is the slice thickness and Z_n is the through-plane gradient of the field map at (x_n, y_n). Substituting (6.21) into (6.1) and including the integration over the slice thickness gives,

$$\begin{aligned} s(t) &= \sum_n f_n e^{-i2\pi(k_x(t)x_n + k_y(t)y_n)} e^{-it\omega_n} \\ &\quad \text{sinc}((2\pi k_x(t)\Delta_x + X_n t)/2\pi)\text{sinc}((2\pi k_y(t)\Delta_y + Y_n t)/2\pi)\text{sinc}(Z_n t/2\pi). \end{aligned} \tag{6.22}$$

This result is similar to (6.19), but with an additional scaling factor due to the through-plane gradient. We can redefine Φ from (6.20) as,

$$\begin{aligned} &\Phi(k_x(t), k_y(t), X_n, Y_n, Z_n, t) = \\ &\text{sinc}\left(k_x(t)\Delta_x + X_n t/2\pi\right)\text{sinc}\left(k_y(t)\Delta_y + Y_n t/2\pi\right)\text{sinc}\left(Z_n t/2\pi\right). \end{aligned} \tag{6.23}$$

6.3 Alternative Approach: Oversampling the Field Map

Instead of modeling the through voxel gradients in the field map as piecewise linear, we could simply reconstruct an oversampled slice while enforcing the piecewise

constant constraint imposed by the object parameterization. For example, in the in-plane dimension, we split a single pixel into a $m_1 \times m_2$ block of pixels of uniform intensity, where m_1, m_2 are the oversampling factors in the x and y directions. We then perform the operation $\tilde{\boldsymbol{A}}\boldsymbol{f}$ using a system matrix, $\tilde{\boldsymbol{A}}$, corresponding to the oversampled slice. In matrix-vector form this corresponds to:

$$s(t) \approx \tilde{\boldsymbol{A}}\boldsymbol{H}\boldsymbol{f}, \tag{6.24}$$

where $\boldsymbol{H}$ corresponds to an $m_1 N_1 m_2 N_2 \times N_1 N_2$ matrix and N_1, N_2 is the original reconstructed image size. The entries of $\boldsymbol{H}$ are $\frac{1}{m_1 m_2}$ in the $m_1 m_2$ places corresponding to the parent pixels in the original image, which was placed in lexicographical order as a column vector. The matrix $\tilde{\boldsymbol{A}}$ is the system matrix corresponding to (2.9) for an image that is m_1, m_2 times larger, *i.e.* the field map ω_n is now an oversampled version. The same idea holds for oversampling in the through-plane direction. We can construct a 3-D object by breaking single pixels into $m_1 m_2 m_3$ cubes of pixels and add the signals from each sub-slice together to get the signal from the total slice. Iterative methods also require the complex conjugate transpose of the above operations which are straightforward to build.

Note that formation of the oversampled system matrix $\tilde{\boldsymbol{A}}$ requires knowledge of the high spatial resolution field map and its gradients. For this work, multi-shot spiral sequences were used to keep readout times and field inhomogeneity distortions small on the high resolution reference scans for field map estimation. A better method that includes joint estimation of the high resolution field map from multi-echo multi-shot readouts may give more accurate high-resolution estimates and will be examined in

our future work.

6.4 Methods

Simulation and phantom experiments were performed to examine the benefit of including the piecewise linear field map model in the field-corrected iterative image reconstruction algorithm. We examined both the inclusion of the gradient terms using Equation (6.19) and the fast, upsampled version of Equation (6.24). Specifically, we looked at the slow DFT-like implementation of Equation (6.19) including just the in-plane gradients (xy), just the through-plane gradients (z), and both the in-plane and through-plane gradients (xyz). We also used the oversampling approximation of Equation (6.24), oversampling by factors of 2 and 3 in each dimension.

Simulations were performed using reconstructed magnitude images and acquired field maps from a high resolution scan of a human volunteer. The parameters for the acquired brain data were: FOV = 16.5 × 22 cm, matrix size of 192 × 256, slice thickness = 1 mm. Simulation data was formed by adding Gaussian noise (SNR = 100) to the evaluation of the signal equation using rect basis functions and a single-shot spiral k-space trajectory. Reconstructions were performed on slice thickness of 3 mm at a matrix size of 64×64.

A phantom scan was performed using single-shot spirals with 1.6 mm and 4.8 mm slice thicknesses. Both scans were with a matrix size of 64×64 and FOV 22 cm. The thin slices had an echo time of 10 ms while the thick slices used an echo time of 30 ms. A field map was obtained from the thin slices and this was used to calculate gradients in the in-plane (x, y), and through-plane (z) directions. This field map and

gradient information was used to reconstruct the thick slice data. For the in-plane gradients, differences were taken between neighboring pixels and averaged.

6.5 Results and Discussion

6.5.1 Simulation Study

Data was created as described in 6.4 from 3 slices with the averaged slice and field map shown in Figure 6.2. The reconstructions performed on the data were: no correction for field inhomogeneities, a conjugate phase reconstruction to correct for the average field map across the 3 slices, an iterative reconstruction using rect basis functions and the average field map across the slices (Iter. Rect. basis), an iterative method implemented using Equation (6.19) with in-plane gradients included (Iter. MR wtxy), an iterative method using Equation (6.19) including only the through-plane gradient of the field map (Iter. MR wt z), an iterative method using Equation (6.19) with both in-plane and through-plane gradients of the field map (Iter. MR wt xyz), and an iterative method using the fast reconstruction algorithm of [13] where the image was upsampled in both in-plane directions and in the through-plane direction by a factor of 2 (Iter. fast wt. 2) and upsampled by a factor of 3 (Iter. fast wt. 3). The results of the reconstructions are shown in Figure 6.3. The resulting NRMS errors are given in Table 6.1 along with the reconstruction times of each method. For this simulation object, inclusion of both the in-plane and through-plane gradients for the field map, *i.e.* the slow xyz gradient method and the fast oversampled methods, resulted in lower NRMS errors for both the complex image subtractions and the magnitude subtractions. Those images also show recovery of

signal in the region above the frontal sinus. The fast, oversampled methods performed similar to the slow xyz-gradient method, but took only a fraction of the time.

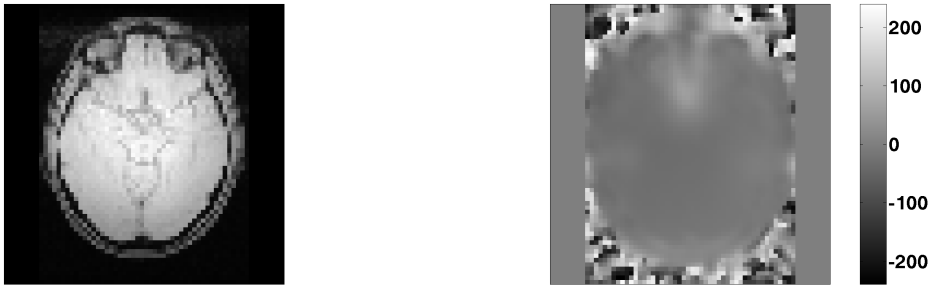

Figure 6.2: Simulation object and field map (Hz) averaged over 3 slices.

Reconstruction Method	**Time (s)**	**NRMSE** (complex)	**NRMSE** (magnitude)
No Correction	0.075	0.338	0.237
Conjugate Phase	0.57	0.338	0.237
Iterative	5.9	0.25	0.279
Iter., XY gradients	357	0.248	0.218
Iter., Z gradient	418	0.253	0.208
Iter., XYZ gradient	421	0.219	0.188
Iter., Fast 2x Oversampled	57.2	0.227	0.190
Iter., Fast 3x Oversampled	147	0.222	0.187

Table 6.1: Computation time and NRMSE between various reconstructions and the simulation object.

6.5.2 Phantom Study

The results for the various reconstructions in the phantom study are shown for one slice in Figure 6.4. The conjugate phase and iterative reconstructions fix some of the field distortions, but signal voids remain in their reconstructions. The iterative reconstruction including only the through-plane, z, gradient does not recover these signal voids. Much of the signal void is recovered when the in-plane gradients are included in the reconstruction as they are for the xy- and xyz-weighted slow iterative

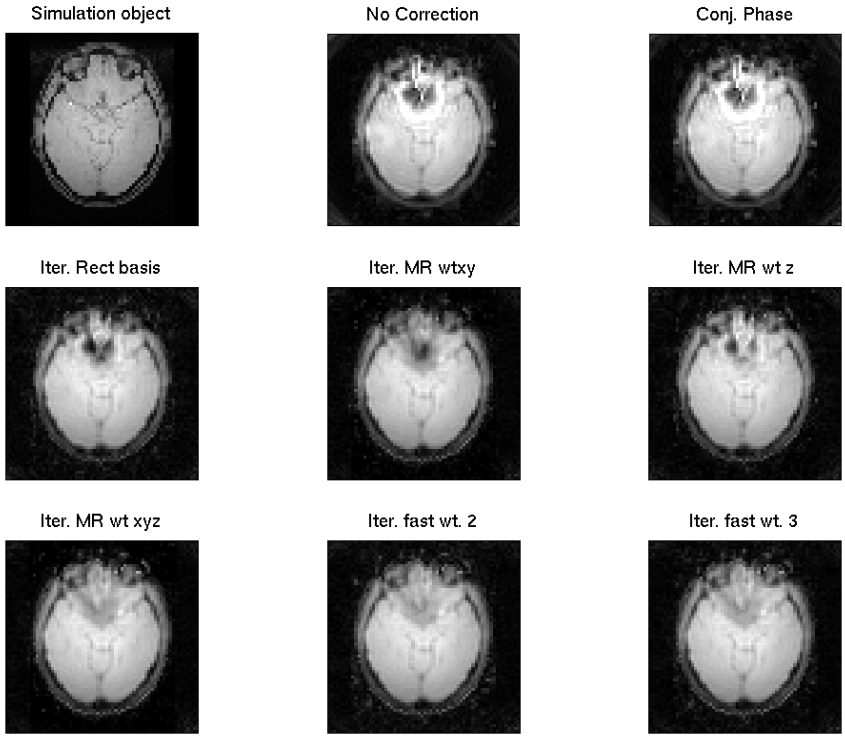

Figure 6.3: Various reconstructions of simulated data.

method and the two and three times fast upsampling iterative methods. Note that a "swirl" artifact exists in the reconstructed images. This could be due to errors in the field map estimate. In our future work, we will explore better methods to estimate the high resolution field map and gradient parameters. This will likely result from a joint estimation algorithm on a multi-shot, multi-echo sequence acquired prior to the low resolution scan to be corrected.

6.6 Summary for Inclusion of the Through-Voxel Gradients

As shown in Table 6.1 for our simulation study, the NRMSE is much lower when both the in-plane and through-plane gradients are taken into account by the system

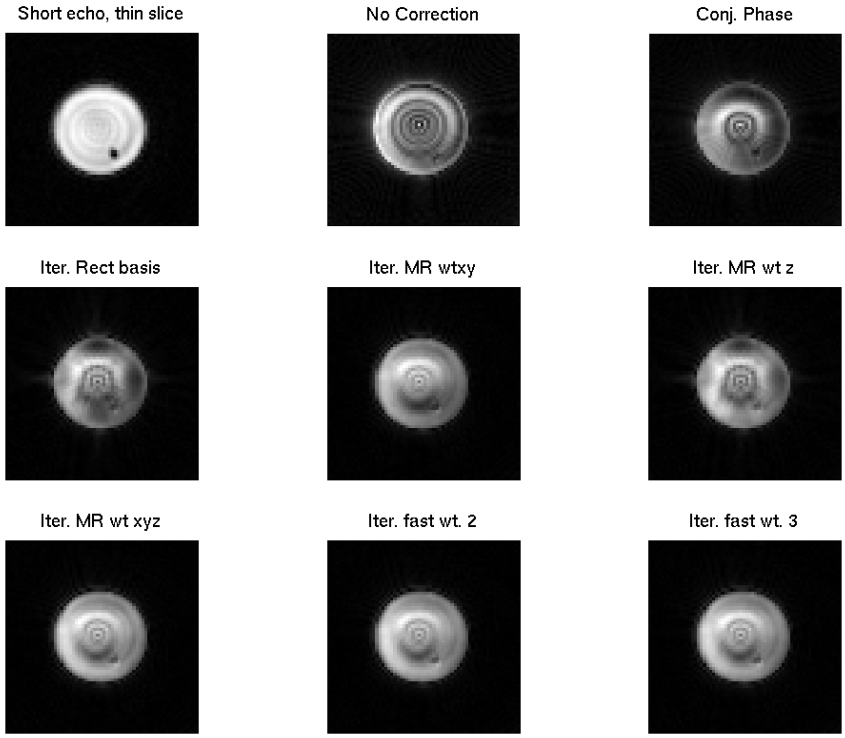

Figure 6.4: Various reconstructions of phantom data.

model. As can be seen in this table, the gains of including these gradient terms are realized by using a fast algorithm that oversamples the field map. Moreover, this fast algorithm takes only a fraction of the computation time of the slow DFT-like implementation required for inclusion of the gradients using Equation (6.19). For the phantom study shown in Figure 6.4, inclusion of the in-plane gradient terms allowed for recovery of signal in the signal void regions remaining after inhomogeneity-corrected reconstruction. Including first order gradients of the field inhomogeneity distribution in the iterative reconstruction model may allow for functional imaging of regions close to air/tissue interfaces that are currently plagued by susceptibility-

induced signal voids.

As higher order terms for the field inhomogeneity variations are included in the system model, more accurate methods will have to be developed to measure the field map and its gradients. Using a joint estimation procedure similar to that in Chapter 5 may result in more accurate estimates.

CHAPTER 7

Summary and Future Work

7.1 Iterative Image Recontruction

As described in Chapter 2, we have developed an iterative image reconstruction framework that allows for easy inclusion of arbitrary k-space trajectories, field inhomogeneity effects, and T_2^*-relaxation. Iterative image reconstruction has some distinct advantages over the standard reconstruction algorithms. First, it does not require density compensation coefficients for non-Cartesian sampling patterns. There is still active research in the area of density compensation, including recent work from our group on spatially-variant density compensation [91]. Another advantage of iterative reconstruction is that the field inhomogeneity is not constrained to be smoothly-varying as it is for the conjugate phase reconstruction. Finally, iterative reconstruction becomes necessary for the complex aliasing patterns of non-Cartesian SENSE reconstructions. In Chapter 3, we included coil sensitivities in our field-corrected iterative image reconstruction framework and showed that, although acquisition time is reduced using SENSE, significant gains still exist from including field-inhomogeneity effects in the SENSE reconstruction.

In answer to the major drawback of iterative methods - computation time, we have developed the non-uniform Fast Fourier Transform and a min-max optimal time segmentation to allow for fast computation of the iterative reconstruction. We examined the stability of the iterative reconstruction in Chapter 4 and concluded that the iterative method is beneficial for reconstructing time-series data from fMRI studies. Iterative image reconstruction resulted in lower residual mean variance, but also lower regression coefficients with the task. Our BOLD SNR measure gave similar results for both iterative and conjugate phase reconstructions. Our iterative method was extended to allow for the simultaneous estimation of the image, field map, and T_2^*-relaxation map in Chapter 5. There was both a static and dynamic component to the improvement using simultaneous estimation of the image and field map. Unlike standard field map estimation methods, the simultaneoues estimation method does not suffer from differences in reference images that are not due to field inhomogeneities, such as respiration-induced phase changes and subject motion. The simultaneous estimation method allowed us to track and correct respiration-induced phase variations and main field drift in the scanner.

Finally, in Chapter 6 we examined the benefits of modeling the effects of the first-order gradients of the field map in the image reconstruction. We showed in simulation and phantom studies that signal can be recovered from signal void regions using a piece-wise linear parameterization of the field map.

7.2 Future Work

The most palpable area of future work for this project is the integration of the components presented. The methods presented in this thesis need to be combined and applied to functional imaging studies in regions of the brain where susceptibility effects and through-voxel gradients are severe. Some specific combinations are:

- Combining SENSE with simultaneous estimation of image, field map, and T_2^*-relaxation may allow for quick, quantitative fMRI experiments.

- The simultaneous estimation algorithm could be extended to estimate the field map and the first order gradients of the field map. Regularization could promote some level of continuity in the piece-wise linear field map.

As mentioned throughout the text, there are many opportunities to extend the iterative image reconstruction framework. I list just a few:

- The signal equation was discretized in time by sampling the ideal expected signal at a time t_i. Including a better model of the temporal sampling into the signal equation could result in more accurate image reconstructions [92]. Such a model could include non-ideal aspects of the acquisition, *i.e.* effects from the anti-aliasing filter, non-linear phase properties of the filters, and a possibly non-constant group delay term.

- Time segmentation was performed in Section 2.3.3 using equally sized time segments. There is no need to space the time segments evenly and allowing this spacing to vary may result in lower approximation error.

- Spatial regularization has been used for the iterative reconstruction throughout this thesis. There may be benefits to regularizing across the temporal domain and should be compared with the temporal filtering of UNFOLD methods [93] or other k-t sampling methods.

- We examined circulant preconditioning to accelerate convergence of the iterative reconstruction. This has been shown to work well for shift-invariant tomographic imaging problems [48], but we have not had much success in the application to field-corrected iterative reconstruction for MRI. Preconditioners have been designed for shift-variant problems [49] and such methods need to be examined for application to MRI.

- The quality of the reconstructions in SENSE experiments depends on the accuracy of sensitivity maps. Methods need to be developed to estimate accurate sensitivity maps while smoothing them and extending them beyond the object without destroying peak information. Also, subject motion could affect the sensitivity of the coils dynamically during an fMRI time series, so auto-focusing methods, such as [94], need to be examined.

- The dynamic estimation scheme of Chapter 5 needs to be optimized in terms of iterative estimation method, number of sub-iterations, and choosing the regularization parameters for the image, field map and R_2^* map automatically. Since joint estimation of image and field map allowed us to track respiration-induced field changes, this method needs to be compared to other physiology-correcting methods, such as DORK [85].

- A goodness measure should be developed to allow for assessment and optimization of k-space trajectory and sequence timing for specific estimation tasks, such as simultaneous estimation of image and field map, and specific coil configurations.

- A better parameterization of the field map to include higher-order terms may be advantageous in regions near air/tissue interfaces, such as just above the frontal sinus. This would include the development of a fast algorithm for including the "triangle" basis functions of Appendix A in the system model. Accurately measuring the parameterized field map becomes very important as more terms are included. It becomes necessary to denoise the field map estimates while preserving the high-frequency information.

APPENDICES

APPENDIX A

Object and inhomogeneity basis are triangle functions

In Chapter 6, we looked at various basis expansions of the continuous object and field map. While a piecewise constant model may be adequate for the object, some gain may be had by taking a different approach with the field map. In regions where the magnetic field is rapidly changing, a piece-wise constant model does not allow for modeling of intravoxel effects. In this appendix, we look at a triangular basis function, $\wedge(x, y)$, in two-dimensions to attempt to find a continuous representation for the field map with first-order gradients.

Let

$$b(x,y) = \wedge(x,y) = \begin{cases} (1-|x|)(1-|y|) & \text{for } x,y \in [-1,1] \\ 0 & \text{else,} \end{cases} \tag{A.1}$$

so that we expand the field inhomogeneity as $\omega(x,y) = \sum_{n',m'} \omega_{n',m'} \wedge \left(\frac{x-x_{n'}}{\Delta_x}, \frac{y-y_{m'}}{\Delta_y} \right)$ and

$$\omega(\Delta_x x + x_n, \Delta_y y + y_m) = \sum_{n',m'} \omega_{n',m'} \wedge (\frac{\Delta_x x + x_n - x_{n'}}{\Delta_x}, \frac{\Delta_y y + y_m - y_{m'}}{\Delta_y}). \tag{A.2}$$

Note that there is a slight change in notation here when compared to Chapter 6, we

are specifically indexing $\omega_{n,m}$ by its x and y indices, n and m. The spatial coordinate $\boldsymbol{r}$ of Chapter 6 is a lexicographical ordering of the x and y indices, so $\boldsymbol{r}_p = (x_n, y_m)$ for $n, m = 1, \ldots, N$ and $p = 1, \ldots, N^2$. This time from (6.6) we get the following for $\alpha_{n,m}(t)$,

$$\begin{aligned}
\alpha_{n,m}(t) &= \int_{-1}^{1}\int_{-1}^{1} (1-|x|)\,(1-|y|) \\
&\quad e^{-i2\pi(k_x(t)\Delta_x x + k_y(t)\Delta_y y)} \exp\Bigg(-it\big(\omega_{n-1,m-1} \wedge (x+1, y+1) \\
&+ \omega_{n-1,m} \wedge (x+1, y) + \omega_{n-1,m+1} \wedge (x+1, y-1) + \omega_{n,m-1} \wedge (x, y+1) \\
&+ \omega_{n,m} \wedge (x, y) + \omega_{n,m+1} \wedge (x, y-1) + \omega_{n+1,m-1} \wedge (x-1, y+1) \\
&+ \omega_{n+1,m} \wedge (x-1, y) + \omega_{n+1,m+1} \wedge (x-1, y-1)\big)\Bigg) dxdy. \qquad \text{(A.3)}
\end{aligned}$$

We expand this in the four quadrants as,

$$
\begin{aligned}
\alpha_{n,m}(t) \;=\; & \int_0^1\int_0^1 (1-x)(1-y)e^{-i2\pi(k_x(t)\Delta_x x + k_y(t)\Delta_y y)} \\
& \exp\Big(-it\big(\omega_{n,m}(1-x)(1-y) + \omega_{n,m+1}(1-x)(y) + \omega_{n+1,m}(x)(1-y) \\
& +\omega_{n+1,m+1}(x)(y)\big)\Big)dxdy \\
+ \; & \int_0^1\int_{-1}^0 (1-x)(1+y)e^{-i2\pi(k_x(t)\Delta_x x + k_y(t)\Delta_y y)} \\
& \exp\Big(-it\big(\omega_{n,m-1}(1-x)(-y) + \omega_{n,m}(1-x)(1+y) + \omega_{n+1,m-1}(x)(-y) \\
& +\omega_{n+1,m}(x)(1+y)\big)\Big)dxdy \\
+ \; & \int_{-1}^0\int_0^1 (1+x)(1-y)e^{-i2\pi(k_x(t)\Delta_x x + k_y(t)\Delta_y y)} \\
& \exp\Big(-it\big(\omega_{n-1,m}(-x)(1-y) + \omega_{n-1,m+1}(-x)(y) + \omega_{n,m}(1+x)(1-y) \\
& +\omega_{n,m+1}(1+x)(y)\big)\Big)dxdy \\
+ \; & \int_{-1}^0\int_{-1}^0 (1+x)(1+y)e^{-i2\pi(k_x(t)\Delta_x x + k_y(t)\Delta_y y)} \\
& \exp\Big(-it\big(\omega_{n-1,m-1}(-x)(-y) + \omega_{n-1,m}(-x)(1+y) + \omega_{n,m-1}(1+x)(-y) \\
& +\omega_{n,m}(1+x)(1+y)\big)\Big)dxdy
\end{aligned}
\tag{A.4}
$$

Now we group the terms in the exponents,

$$\begin{aligned}
\alpha_{n,m}(t) &= \int_0^1\int_0^1 (1-x)(1-y)\exp\Big(-i\big(\omega_{n,m}t + x(2\pi k_x(t)\Delta_x + t(-\omega_{n,m}+\omega_{n+1,m})) \\
&\quad + y(2\pi k_y(t)\Delta_y + t(-\omega_{n,m}+\omega_{n,m+1})) \\
&\quad + xyt(\omega_{n,m}-\omega_{n,m+1}-\omega_{n+1,m}+\omega_{n+1,m+1})\big)\Big)dxdy \\
&+ \int_0^1\int_{-1}^0 (1-x)(1+y)\exp\Big(-i\big(\omega_{n,m}t + x(2\pi k_x(t)\Delta_x + t(-\omega_{n,m}+\omega_{n+1,m})) \\
&\quad + y(2\pi k_y(t)\Delta_y + t(\omega_{n,m}-\omega_{n,m-1})) \\
&\quad + xyt(-\omega_{n,m}+\omega_{n,m-1}+\omega_{n+1,m}-\omega_{n+1,m-1})\big)\Big)dxdy \\
&+ \int_{-1}^0\int_0^1 (1+x)(1-y)\exp\Big(-i\big(\omega_{n,m}t + x(2\pi k_x(t)\Delta_x + t(\omega_{n,m}-\omega_{n-1,m})) \\
&\quad + y(2\pi k_y(t)\Delta_y + t(-\omega_{n,m}+\omega_{n,m+1})) \\
&\quad + xyt(-\omega_{n,m}+\omega_{n,m+1}+\omega_{n-1,m}-\omega_{n-1,m+1})\big)\Big)dxdy \\
&+ \int_{-1}^0\int_{-1}^0 (1+x)(1+y)\exp\Big(-i\big(\omega_{n,m}t + x(2\pi k_x(t)\Delta_x + t(\omega_{n,m}-\omega_{n-1,m})) \\
&\quad + y(2\pi k_y(t)\Delta_y + t(\omega_{n,m}-\omega_{n,m-1})) \\
&\quad + xyt(\omega_{n,m}-\omega_{n,m-1}-\omega_{n-1,m}+\omega_{n-1,m-1})\big)\Big)dxdy. \qquad \text{(A.5)}
\end{aligned}$$

Notice that the x and y terms have a measure of the k-space trajectory plus a gradient of the field map. The xy term has what could be considered the sum of the cross-gradient terms. The integrals in (A.5) can all be expressed in the form,

$$e^{-it\omega_{n,m}}\int_0^1\int_0^1 (1-x)(1-y)e^{-i(Bx+Cy+Dxy)}dxdy. \qquad \text{(A.6)}$$

Note here that B and C can be only two expressions, whereas D can be one of four expressions. Another thing to note is that D is zero for steps in the field map that occur in the x or y direction, it is also zero for ramps in the xy direction. The values

for B, C, and D for the four integrals above are:

$$\begin{aligned}
B_1 &= 2\pi k_x(t)\Delta_x + t(-\omega_{n,m} + \omega_{n+1,m}) \\
C_1 &= 2\pi k_y(t)\Delta_y + t(-\omega_{n,m} + \omega_{n,m+1}) \\
D_1 &= t(\omega_{n,m} - \omega_{n,m+1} - \omega_{n+1,m} + \omega_{n+1,m+1} \\
B_2 &= B_1 \\
C_2 &= -(2\pi k_y(t)\Delta_y + t(\omega_{n,m} - \omega_{n,m-1})) \\
D_2 &= -t(-\omega_{n,m} + \omega_{n,m-1} + \omega_{n+1,m} - \omega_{n+1,m-1}) \\
B_3 &= -(2\pi k_x(t)\Delta_x + t(\omega_{n,m} - \omega_{n-1,m})) \\
C_3 &= C_1 \\
D_3 &= -t(-\omega_{n,m} + \omega_{n,m+1} + \omega_{n-1,m} - \omega_{n-1,m+1}) \\
B_4 &= B_3 \\
C_4 &= C_2 \\
D_4 &= t(\omega_{n,m} - \omega_{n,m-1} - \omega_{n-1,m} + \omega_{n-1,m-1}).
\end{aligned} \tag{A.7}$$

So, $\alpha_{n,m}(t)$ can be evaluated by summing up the results of evaluating (A.6) with all 4 sets of coefficients. The integral in (A.6) can be rearranged as follow,

$$e^{-it\omega_{n,m}} \int_0^1 (1-y) e^{-iCy} \left(\int_0^1 (1-x) e^{-ix(B+Dy)} dx \right) dy. \tag{A.8}$$

Evaluating the integral inside parenthesis, we get,

$$\begin{aligned}
&= e^{-it\omega_{n,m}} \int_0^1 (1-y) e^{-i(Cy)} \left(- \frac{-e^{-i(B+Dy)} - i(B+Dy) + 1}{(B+Dy)^2} \right) dy \\
&= e^{-it\omega_{n,m}} \int_0^1 e^{-i(Cy)} \left(\frac{-e^{-i(B+Dy)} - i(B+Dy) + 1}{(B+Dy)^2} \right) dy \\
&- e^{-it\omega_{n,m}} \int_0^1 y e^{-i(Cy)} \left(\frac{-e^{-i(B+Dy)} - i(B+Dy) + 1}{(B+Dy)^2} \right) dy.
\end{aligned} \tag{A.9}$$

Letting,

$$\begin{aligned}\gamma(y) &= e^{-it\omega_{n,m}}\int_0^1 e^{-i(Cy)}\left(\frac{-e^{-i(B+Dy)}-i(B+Dy)+1}{(B+Dy)^2}\right)dy,\\ &= e^{-it\omega_{n,m}}\int_0^1\left(\frac{-e^{-i(B+(C+D)y)}}{(B+Dy)^2}-i\frac{e^{-iCy}}{B+Dy}+\frac{e^{-iCy}}{(B+Dy)^2}\right)dy \quad \text{(A.10)}\end{aligned}$$

equation (A.9) becomes

$$\begin{aligned}&\gamma(1)-\gamma(0)-\int_0^1 y\gamma'(y)dy\\ &= \gamma(1)-\gamma(0)-\Big[y\gamma(y)-\int\gamma(y)dy\Big]\Big|_{y=0}^{y=1} \quad \text{(A.11)}\end{aligned}$$

Now we turn our attention to evaluating the integral in $\gamma(y)$. We will do this in a term by term fashion as follows,

$$\int\frac{e^{-i(B+(C+D)y)}}{(B+Dy)^2}dy = e^{-iB}\int\frac{e^{-i(C+D)y}}{(B+Dy)^2}dy.$$

Letting $v = B+Dy$, and hence $y=(v-B)/D$,

$$\begin{aligned}&= \frac{e^{-iB}}{D}\int\frac{e^{-i(C+D)(v-B)/D}}{v^2}dv\\ &= \frac{e^{iBC/D}}{D}\int\frac{e^{-i(C+D)v/D}}{v^2}dv\\ &= \frac{e^{iBC/D}}{D}\left[-\frac{e^{-i(C+D)v/D}}{v}-\frac{i(C+D)}{D}\int\frac{e^{-i(C+D)v/D}}{v}dv\right] \quad \text{(A.12)}\end{aligned}$$

From a table of integrals [95], we know that,

$$\begin{aligned}\int\frac{e^{ax}}{x}dx &= \ln(x)+\frac{ax}{1\cdot 1!}+\frac{(ax)^2}{2\cdot 2!}+\frac{(ax)^3}{3\cdot 3!}\\ &= \zeta(a,x). \quad \text{(A.13)}\end{aligned}$$

Returning to our problem, (A.12), and plugging back in $v = B+Dy$,

$$\int\frac{e^{-i(B+(C+D)y)}}{(B+Dy)^2}dy =$$

$$-\frac{e^{-i(B+(C+D)y)}}{D(B+Dy)}-\frac{i(C+D)}{D^2}e^{i(BC/D)}\zeta(-i(C+D)/D, B+Dy). \quad \text{(A.14)}$$

Continuing on with the next term in (A.10), and making the same substitution for v as in (A.12),

$$\begin{aligned} i\int \frac{e^{-iCy}}{B+Dy}dy &= \frac{i}{D}\int \frac{e^{-i(C(v-B)/D}}{v}dv \\ &= \frac{ie^{iBC/D}}{D}\int \frac{e^{-iCv/D}}{v}dv \\ &= \frac{ie^{iBC/D}}{D}\zeta(-iC/D, B+Dy). \end{aligned} \tag{A.15}$$

For the final term in (A.10), we get,

$$\begin{aligned} \int \frac{e^{-iCy}}{(B+Dy)^2}dy &= -\frac{e^{-iCy}}{D(B+Dy)} - i\frac{C}{D}\int \frac{e^{-iCy}}{(B+Dy)}dy \\ &= -\frac{e^{-iCy}}{D(B+Dy)} - i\frac{Ce^{iBC/D}}{D^2}\zeta(-iC/D, B+Dy), \end{aligned} \tag{A.16}$$

where the result for the integral $\int e^{-iCy}/(B+Dy)dy$ was taken from (A.15).

Combining these results,

$$\begin{aligned} \gamma(y) &= e^{-it\omega_{n,m}}\int_0^1 \left(\frac{-e^{-i(B+(C+D)y)}}{(B+Dy)^2} - i\frac{e^{-iCy}}{B+Dy} + \frac{e^{-iCy}}{(B+Dy)^2}\right)dy \\ &= e^{-it\omega_{n,m}}\Bigg(\frac{e^{-i(B+(C+D)y)}}{D(B+Dy)}\frac{i(C+D)}{D^2}e^{i(BC/D)}\zeta(-i(C+D)/D, B+Dy) - \\ &- \frac{ie^{iBC/D}}{D}\zeta(-iC/D, B+Dy) - \frac{e^{-iCy}}{D(B+Dy)} \\ &- i\frac{Ce^{iBC/D}}{D^2}\zeta(-iC/D, B+Dy) + \eta\Bigg) \\ &= e^{-it\omega_{n,m}}\Bigg(\frac{e^{-i(B+(C+D)y)} - e^{-iCy}}{D(B+Dy)} - i\frac{e^{iBC/D}}{D}(1+C/D) \\ &\cdot \quad \Big[\zeta(-i(C+D)/D, B+Dy) - \zeta(-iC/D, B+Dy)\Big] + \eta\Bigg), \end{aligned} \tag{A.17}$$

where η is the constant of integration. Examining (A.17), we can see that the worrisome case of an $x = 0$ in the ln function of (A.13) will cancel out and not cause problems. We now evaluate the integral of $\gamma(y)$ to finish the calculation in

(A.11).

$$\begin{aligned}\int \gamma(y) &= \frac{e^{-it\omega_{n,m}}}{D}\int\left(\frac{e^{-i(B+(C+D)y)}}{B+Dy}-\frac{e^{-iCy}}{B+Dy}+ie^{iBC/D}(1+C/D)\right.\\ &\cdot \left.\Big[\zeta(-i(C+D)/D,B+Dy)-\zeta(-iC/D,B+Dy)\Big]\right)dy\\ &= \frac{e^{-it\omega_{n,m}}e^{iBC/D}}{D^2}\Bigg(\zeta(-i(C+D)/D,B+Dy)-\zeta(-iC/D,B+Dy)\\ &+ i(1+C/D)H(-i(C+D)/D,-iC/D,B+Dy)\Bigg), \qquad (A.18)\end{aligned}$$

where

$$H(\alpha_1,\alpha_2,v)=\frac{(\alpha_1-\alpha_2)v^2}{1\cdot 2!}+\frac{(\alpha_1^2-\alpha_2^2)v^3}{2\cdot 3!}+\cdots. \qquad (A.19)$$

Returning to (A.11), we get the following for the generic integral in (A.6)

$$\begin{aligned}&- \gamma(0)-\gamma(1)+\int_0^1\gamma(y)dy\\ &= e^{-it\omega_{n,m}}\Bigg(-\frac{e^{-iB}-1}{DB}+i\frac{e^{iBC/D}}{D}(1+C/D)\Big[\zeta(-i(C+D)/D,B)-\zeta(-iC/D,B)\Big]\\ &- \frac{e^{-i(B+C+D)}-e^{-iC}}{D(B+D)}\\ &+ i\frac{e^{iBC/D}}{D}(1+C/D)\Big[\zeta(-i(C+D)/D,B+D)-\zeta(-iC/D,B+D)\Big]\Bigg)\\ &+ \frac{e^{-it\omega_{n,m}}e^{iBC/D}}{D^2}\Bigg(\zeta(-i(C+D)/D,B+D)-\zeta(-iC/D,B+D)\\ &+ i(1+C/D)H(-i(C+D)/D,-iC/D,B+D)-\zeta(-i(C+D)/D,B)\\ &+ \zeta(-iC/D,B)-i(1+C/D)H(-i(C+D)/D,-iC/D,B)\Bigg) \qquad (A.20)\end{aligned}$$

We can evaluate the integral in (A.4) by plugging in the appropriate B,C,D entries for each integral.

A.1 Alternative Computation of Triangle basis functions

An alternative way to evaluate the above is as follows:

$$\begin{aligned}\int_0^1 (1-x)e^{-ix(B+Dy)}dx &= \int_{-\infty}^{\infty} \text{rect}(x-1/2) \wedge (x) e^{-ix(B+Dy)}dx \\ &= \left(\text{sinc}(u)e^{-i\pi u} \otimes \text{sinc}^2(u)\right)_{u=(B+Dy)/(2\pi)} \\ &= v\left(\frac{B+Dy}{2\pi}\right), \end{aligned} \tag{A.21}$$

letting $v(u) = \text{sinc}(u)e^{-i\pi u} \otimes \text{sinc}^2(u)$. Returning to (A.8), we get

$$\begin{aligned} & e^{-it\omega_{n,m}} \int_0^1 (1-y) v\left(\frac{B+Dy}{2\pi}\right) e^{-iyC} dy \\ = \; & e^{-it\omega_{n,m}} \int_{-\infty}^{\infty} \text{rect}(y-1/2) \wedge (y) v\left(\frac{B+Dy}{2\pi}\right) e^{-iyC} dy \\ = \; & e^{-it\omega_{n,m}} \left(\text{sinc}(u)e^{-i\pi u} \otimes \text{sinc}^2(u) \otimes V(u)\right)_{u=C/2\pi}, \end{aligned} \tag{A.22}$$

where $V(u)$ is the Fourier Transform of $v\left(\frac{B+Dy}{2\pi}\right)$. Letting $V_1(u)$ be the $V(u)$ associated with B_1 and D_1, and letting $W^1_{n,m}(u) = \text{sinc}(u)e^{-i\pi u} \otimes \text{sinc}^2(u) \otimes V_1(u)$ and likewise $W^2_{n,m}$, $W^3_{n,m}$, and $W^4_{n,m}$, we get the following for $\alpha_{n,m}(t)$,

$$\begin{aligned} \alpha_{n,m}(t) &= e^{-it\omega_{n,m}} \left(W^1_{n,m}(C_1/2\pi) + W^2_{n,m}(C_2/2\pi)\right. \\ &+ \left. W^3_{n,m}(C_3/2\pi) + W^4_{n,m}(C_4/2\pi)\right). \end{aligned} \tag{A.23}$$

Plugging this back into the signal equation (6.7), we get,

$$\begin{aligned} s(t) &\approx \Delta_x \Delta_y \sum_{n,m} f_{n,m} e^{-i2\pi(k_x(t)x_n + k_y(t)y_m} e^{-it\omega_{n,m}} \\ &\cdot \left(W^1_{n,m}(C_1/2\pi) + W^2_{n,m}(C_2/2\pi) + W^3_{n,m}(C_3/2\pi) + W^4_{n,m}(C_4/2\pi)\right) \end{aligned} \tag{A.24}$$

This result is promising and future work may lead to efficient implementations.

A.2 Conclusion

Both of these approaches to analyzing the signal equation with triangle basis functions led to complex expressions that are not easily included in a quick iterative reconstruction algorithm. Future work may lead to approximations or table lookup methods of implementing this expansion.

BIBLIOGRAPHY

BIBLIOGRAPHY

[1] E. M. Haacke, R. W. Brown, M. R. Thompson, and R. Venkatesan. *Magnetic resonance imaging: Physical principles and sequence design.* John Wiley and Sons, New York, 1999.

[2] E. Schneider and G. Glover. Rapid in vivo proton shimming. *Magn. Reson. Med.*, 18:335–347, 1991.

[3] D. C. Noll. Multishot rosette trajectories for spectrally selective MR imaging. *IEEE Trans. Med. Imag.*, 16(4):372–377, 1997.

[4] R. D. Hoge, R. K. S. Kwan, and G. B. Pike. Density compensation functions for spiral MRI. *Magn. Reson. Med.*, 38:117–128, 1997.

[5] J. I. Jackson, C. H. Meyer, D. G. Nishimura, and A. Macovski. Selection of a convolution function for Fourier inversion using gridding. *IEEE Trans. Med. Imag.*, 10(3):473–478, 1991.

[6] H. Sedarat and D. G. Nishimura. On the optimality of the gridding reconstruction algorithm. *IEEE Trans. Med. Imag.*, 19(4):306–317, 2000.

[7] J. G. Pipe. Reconstructing MR images from undersampled data: Data-weighting considerations. *Magn. Reson. Med.*, 43:867–875, 2000.

[8] J. G. Pipe and P. Menon. Sampling density compensation in MRI: Rationale and an iterative numerical solution. *Magn. Reson. Med.*, 41:179–186, 1999.

[9] Y. Qian, J. Lin, and D. Jin. Reconstruction of MR images from data acquired on an arbitrary k-space trajectory using the same-image weight. *Magn. Reson. Med.*, 48:306–311, 2002.

[10] H. Schomberg. Notes on direct and gridding-based Fourier inversion methods. In *Proc. IEEE Int. Symp. Biomed. Im.*, pages 645–648, 2002.

[11] C. H. Meyer, B. S. Hu, D. G. Nishimura, and A. Macovski. Fast spiral coronary artery imaging. *Magn. Reson. Med.*, 28(2):202–213, 1992.

[12] V. Rasche, R. Proksa, R. Sinkus, P. Börnert, and H. Eggers. Resampling of data between arbitrary grids using convolution interpolation. *IEEE Trans. Med. Imag.*, 18(5):385–392, 1999.

[13] B. P. Sutton, D. C. Noll, and J. A. Fessler. Fast, iterative, field-corrected image reconstruction for MRI. *IEEE Trans. Med. Imag.*, 22(2):178–188, 2003.

[14] S. X. Pan and A. C. Kak. A computational study of reconstruction algorithms for diffraction tomography: Interpolation versus filtered backpropagation. *IEEE Trans. Acoustics, Speech, Sig. Proc.*, ASSP-31(5):1262–1275, 1983.

[15] H. Stark, J. W. Woods, I. Paul, and R. Hingorani. An investigation of computerized tomography by direct fourier inversion and optimum interpolation. *IEEE Trans. Biomed. Eng.*, BME-28(7):496–505, 1981.

[16] H. Stark, J. W. Woods, I. Paul, and R. Hingorani. Direct fourier reconstruction in computer tomography. *IEEE Trans. Acoustics, Speech, and Signal Proc.*, ASSP-29(2):237–245, 1981.

[17] D. Rosenfeld. An optimal and efficient new gridding algorithm using singular value decomposition. *Magn. Reson. Med.*, 40:14–23, 1998.

[18] T.-K. Truong, B. D. Clymer, D. W. Chakeres, and P. Schmalbrock. Three-dimensional numerical simulations of susceptibility-induced magnetic field inhomogeneities in the human head. *Magnetic Resonance Imaging*, 20(10):759–770, 2002.

[19] K. Sekihara, M. Kuroda, and H. Kohno. Image restoration from non-uniform magnetic field influence for direct Fourier NMR imaging. *Phys. Med. Biol.*, 29(1):15–24, 1984.

[20] E. Yudilevich and H. Stark. Spiral sampling in magnetic resonance imaging - the effect of inhomogeneities. *IEEE Trans. Med. Imag.*, 6(4):337–345, 1987.

[21] S. Ogawa, D. W. Tank, R. Menon, J. M. Ellerman, S.-G. Kim, H. Merkle, and K. Ugurbil. Intrinsic signal changes accompanying sensory stimulation: Functional brain mapping with magnetic resonance imaging. *Proc Natl Acad Sci*, 89:5951–5955, 1992.

[22] D. G. Nishimura. Principles of magnetic resonance imaging. Department of Electrical Engineering: Stanford University, 1996.

[23] T. H. Le and X. Hu. Retrospective estimation and correction of physiological artifacts in fMRI by direct extraction of physiological activity from MR data. *Magn. Reson. Med.*, 35:290–298, 1996.

[24] T. S. Sumanaweera, G. H. Glover, T. O. Binford, and J. R. Adler. MR susceptibility misregistration correction. *IEEE Trans. Med. Imag.*, 12(2):251–259, 1993.

[25] P. Jezzard and R. S. Balaban. Correction for geometric distortion in echo planar images from B_0 field variations. *Magn. Reson. Med.*, 34:65–73, 1995.

[26] P. J. Reber, E. C. Wong, R. B. Buxton, and L. R. Frank. Correction of off resonance-related distortion in echo-planar imaging using EPI-based field maps. *Magn. Reson. Med.*, 39:328–330, 1998.

[27] Y. M. Kadah and X. Hu. Simulated phase evolution rewinding (SPHERE): A technique for reducing B_0 inhomogeneity effects in MR images. *Magn. Reson. Med.*, 38:615–627, 1997.

[28] D. C. Noll, J. M. Pauly, C. H. Meyer, D. G. Nishimura, and A. Macovski. Deblurring for non-2D Fourier transform magnetic resonance imaging. *Magn. Reson. Med.*, 25:319–333, 1992.

[29] L.-C. Man, J. M. Pauly, and A. Macovski. Improved automatic off-resonance correction without a field map in spiral imaging. *Magn. Reson. Med.*, 37:906–913, 1997.

[30] D. C. Noll, C. H. Meyer, J. M. Pauly, D. G. Nishimura, and A. Macovski. A homogeneity correction method for magnetic resonance imaging with time-varying gradients. *IEEE Trans. Med. Imag.*, 10(4):629–637, 1991.

[31] H. Schomberg. Off-resonance correction of MR images. *IEEE Trans. Med. Imag.*, 18(6):481–495, 1999.

[32] L.-C. Man, J. M. Pauly, and A. Macovski. Multifrequency interpolation for fast off-resonance correction. *Magn. Reson. Med.*, 37:785–792, 1997.

[33] T. B. Harshbarger and D. B. Twieg. Iterative reconstruction of single-shot spiral MRI with off resonance. *IEEE Trans. Med. Imag.*, 18(3):196–205, 1999.

[34] D. C. Noll. Rapid MR image acquisition in the presence of background gradients. In *Proc. IEEE Int. Symp. Biomed. Im.*, pages 725–728, 2002.

[35] J. A. Fessler and B. P. Sutton. Nonuniform fast Fourier transforms using min-max interpolation. *IEEE Trans. Signal Processing*, 51(2):560–574, 2003.

[36] P. Munger, G. R. Crelier, T. M. Peters, and G. B. Pike. An inverse problem approach to the correction of distortion in EPI images. *IEEE Trans. Med. Imag.*, 19(7):681–689, 2000.

[37] L.-C. Man, J. M. Pauly, and A. Macovski. Correcting severe local inhomogeneity blurs by spatially variant deconvolution. In *Proceedings of the SMR, 3rd Scientific Meeting*, volume 2, page 738, 1995.

[38] K.P. Pruessmann, M. Weiger, M. B. Scheidegger, and P. Boesiger. SENSE: Sensitivity encoding for fast MRI. *Magn. Reson. Med.*, 42:952–962, 1999.

[39] K. P. Pruessmann, M. Weiger, P. Börnert, and P. Boesiger. Advances in sensitivity encoding with arbitrary k-space trajectories. *Magn. Reson. Med.*, 46:638–651, 2001.

[40] J. R. Shewchuk. An introduction to the conjugate gradient method without the agonizing pain, edition 1 $\frac{1}{4}$. Technical report, School of Computer Science, Carnegie Mellon University, 1994. http://www-2.cs.cmu.edu/∼jrs/jrspapers.html.

[41] S. Lucidi. Numerical experiences with new truncated newton methods in large scale unconstrained optimization. *Computational Optimization and Applications*, 7:71–81, 1997.

[42] G. H. Golub and C. F. Van Loan. *Matrix Computations*. The Johns Hopkins University Press, Baltimore, third edition, 1996.

[43] R. Van de Walle, H. H. Barrett, K. J. Myers, M. I. Altbach, B. Desplanques, A. F. Gmitro, J. Cornelis, and I. Lemahieu. Reconstruction of MR images from data acquired on a general nonregular grid by pseudoinverse calculation. *IEEE Trans. Med. Imag.*, 19(12):1160–1167, 2000.

[44] J. A. Fessler and W. L. Rogers. Spatial resolution properties of penalized-likelihood image reconstruction methods: Space-invariant tomographs. *IEEE Trans. Image Processing*, 5(9):1346–1358, 1996.

[45] P. J. Huber. *Robust statistics*. Wiley, New York, 1981.

[46] Y.-H. Kao and J. R. MacFall. Correction of MR k-space data corrupted by spike noise. *IEEE Trans. Med. Imag.*, 19(7):671–680, 2000.

[47] Y. M. Kadah and X. Hu. Algebraic reconstruction for magnetic resonance imaging under B_0 inhomogeneity. *IEEE Trans. Med. Imag.*, 17(3):362–370, 1998.

[48] N. H. Clinthorne, T-S. Pan, P-C. Chiao, W. L. Rogers, and J. A. Stamos. Preconditioning methods for improved convergence rates in iterative reconstructions. *IEEE Trans. Med. Imag.*, 12(1):78–83, 1993.

[49] J. A. Fessler and S. D. Booth. Conjugate-gradient preconditioning methods for shift-variant PET image reconstruction. *IEEE Trans. Image Processing*, 8(5):688–699, 1999.

[50] A. Dutt and V. Rokhlin. Fast Fourier transforms for nonequispaced data. *SIAM J on Sci. Comput.*, 14(6):1368–1393, 1993.

[51] A. Dutt and V. Rokhlin. Fast Fourier transforms for nonequispaced data, II. *Applied and Computational Harmonic Analysis*, 2:85–100, 1995.

[52] G. Beylkin. On the fast Fourier transform of functions with singularities. *Applied and Computational Harmonic Analysis*, 2:363–381, 1995.

[53] C. Anderson and M. D. Dahleh. Rapid computation of the discrete Fourier transform. *SIAM J on Sci. Comput.*, 17(4):913–919, 1996.

[54] G. Steidl. A note on fast Fourier transforms for nonequispaced grids. *Advances in Computational Mathematics*, 9:337–352, 1998.

[55] A. F. Ware. Fast approximate Fourier transforms for irregularly spaced data. *SIAM Review*, 40(4):838–856, 1998.

[56] Q. H. Liu and N. Nguyen. An accurate algorithm for nonuniform fast Fourier transforms (NUFFT's). *IEEE Microwave and Guided Wave Letters*, 8(1):18–20, 1998.

[57] N. Nguyen and Q. H. Liu. The regular Fourier matrices and nonuniform fast Fourier transforms. *SIAM J on Sci. Comput.*, 21(1):283–293, 1999.

[58] A. J. W. Duijndam and M. A. Schonewille. Nonuniform fast Fourier transform. *Geophysics*, 64(2):539–551, 1999.

[59] S. A. R. Kannengießer, J. M. Pauly, and R. K. Butts. Fast image reconstruction for sensitivity encoded spiral imaging. In *ISMRM Ninth Scientific Meeting*, page 1800, 2001.

[60] B. Sutton, J. A. Fessler, and D. Noll. A min-max approach to the nonuniform N-dimensional FFT for rapid iterative reconstruction of MR images. In *ISMRM Ninth Scientific Meeting*, page 763, 2001.

[61] T. Strohmer. Computationally attractive reconstruction of bandlimited images from irregular samples. *IEEE Trans. Image Processing*, 6(4):540–548, 1997.

[62] T. Strohmer. Numerical analysis of the non-uniform sampling problem. *J. Comp. Appl. Math.*, 122(1-2):297–316, 2000.

[63] J. A. Fessler and B. P. Sutton. A min-max approach to the multidimensional nonuniform FFT: Application to tomographic image reconstruction. In *Proc. IEEE Intl. Conf. on Image Processing*, volume 1, pages 706–709, 2001.

[64] D. C. Noll. *Reconstruction techniques for magnetic resonance imaging.* PhD thesis, Stanford, CA, 1991.

[65] P. Irarrazabal, C. H. Meyer, D. G. Nishimura, and A. Macovski. Inhomogeneity correction using an estimated linear field map. *Magn. Reson. Med.*, 35:278–282, 1996.

[66] B. Sutton, J. A. Fessler, and D. Noll. Field-corrected imaging using joint estimation of image and field map. In *ISMRM Tenth Scientific Meeting*, page 737, 2002.

[67] B. Sutton, J. A. Fessler, and D. Noll. Iterative MR image reconstruction using sensitivity and inhomogeneity field maps. In *ISMRM Ninth Scientific Meeting*, page 771, 2001.

[68] A. W. Song, E. C. Wong, and J. S. Hyde. Echo-volume imaging. *Magn. Reson. Med.*, 32:668–671, 1994.

[69] M. A. Bernstein, X. J. Zhou, J. A. Polzin, K. F. King, A. Ganin, N. J. Pelc, and G. H. Glover. Concomitant gradient terms in phase constrast MR: Analysis and correction. *Magn. Reson. Med.*, 39:300–308, 1998.

[70] K. F. King, A. Ganin, X. J. Zhou, and M. A. Bernstein. Concomitant gradient field effects in spiral scans. *Magn. Reson. Med.*, 41:103–112, 1999.

[71] M. I. Miller, T. J. Schaewe, C. S. Bosch, and J. J. H. Ackerman. Model-based maximum likelihood estimation for phase- and frequency-encoded magnetic-resonance-imaging data. *Journal of Magnetic Resonance, Series B*, 107:210–221, 1995.

[72] B. P. Sutton, D. C. Noll, and J. A. Fessler. Simultaneous estimation of image and inhomogeneity field map. In *ISMRM Workshop on Min. MR Data Acquisition Methods: Making More with Less*, pages 15–18, 2001.

[73] B. Sutton, S. J. Peltier, J. A. Fessler, and D. Noll. Simultaneous estimation of I_o, R_2^*, and field map using a multi-echo spiral acquisition. In *ISMRM Tenth Scientific Meeting*, page 1323, 2002.

[74] S. J. Peltier, B. Sutton, J. A. Fessler, and D. Noll. Simultaneous estimation of I_o, R_2^*, and field map using a multi-echo spiral acquisition. In *Human Brain Mapping*, page 10081, 2002.

[75] P Kellman, F. H. Epstein, and E. R. McVeigh. Adaptive sensitivity encoding incorporating temporal filtering (TSENSE). *Magn. Reson. Med.*, 45:846–852, 2001.

[76] P. Kellman and E. R. McVeigh. Method for combining UNFOLD with SENSE or SMASH. In *ISMRM Eighth Scientific Meeting*, page 1507, 2000.

[77] B. Madore. Using UNFOLD to remove artifacts in parallel imaging and in partial-Fourier imaging. *Magn. Reson. Med.*, 48:493–501, 2002.

[78] J. A. Fessler. Penalized weighted least-squares image reconstruction for positron emission tomography. *IEEE Trans. Med. Imag.*, 13(2):290–300, 1994.

[79] B. P. Sutton, D. C. Noll, and J. A. Fessler. Dynamic field map estimation using a single spiral in/ spiral out acquisition. In *ISMRM Eleventh Scientific Meeting*, page 479, 2003.

[80] S. J. Peltier and D. C. Noll. Physiological noise in multi-shot functional MRI. In *ISMRM Tenth Scientific Meeting*, page 118, 2002.

[81] K. S. Nayak, C.-M. Tsai, C. H. Meyer, and D. G. Nishimura. Efficient off-resonance correction for spiral imaging. *Magn. Reson. Med.*, 45:521–524, 2001.

[82] K. S. Nayak and D. G. Nishimura. Automatic field map generation and off-resonance correction for projection reconstruction imaging. *Magn. Reson. Med.*, 43:151–154, 2000.

[83] G. H. Glover and C. S. Law. Spiral in/out BOLD fMRI for increased SNR and reduced susceptibility artifacts. *Magn. Reson. Med.*, 46:515–522, 2001.

[84] J. W. Stayman and J. A. Fessler. Regularization for uniform spatial resolution properties in penalized-likelihood image reconstruction. *IEEE Trans. Med. Imag.*, 19(6):601–615, 2000.

[85] J. Pfeuffer, P.-F. Van de Moortele, K. Ugurbil, X. Hu, and G. H. Glover. Correction of physiologically-induced global off-resonance effects in dynamic echo-planar and spiral functional imaging. *Magn. Reson. Med.*, 47:344–353, 2002.

[86] A. B. A. Wennerberg, T. Jonsson, H. Forssberg, and T.-Q. Li. A comparative fMRI study: T_2^*-weighted imaging versus R_2^* mapping. *NMR in Biomedicine*, 14:41–47, 2001.

[87] S. Posse, S. Wiese, D. Gembris, K. Mathiak, C. Kessler, M.-L. Grosse-Ruyken, B. Elghahwagi, T. Richards, S. R. Dager, and V. G. Kiselev. Enhancement of BOLD-contrast sensitivity by single-shot multi-echo functional MR imaging. *Magn. Reson. Med.*, 42:87–97, 1999.

[88] O. Speck and J. Hennig. Functional imaging by I_0- and T_2^*- parameter mapping using multi-image EPI. *Magn. Reson. Med.*, 40:243–248, 1998.

[89] V. G. Kiselev, S. Wiese, and S. Posse. Distinction of activation and noise in fMRI by multi-echo sampling. In *ISMRM Seventh Scientific Meeting*, 1999.

[90] J. P. Wansapura, S. K. Holland, R. S. Dunn, and Jr. W. S. Ball. NMR relaxation times in the human brain at 3.0 tesla. *Journal of Magnetic Resonance Imaging*, 9:531–538, 1999.

[91] D. C. Noll. Conjugate phase reconstruction with spatially variant sample density correction. In *ISMRM Eleventh Scientific Meeting*, page 476, 2003.

[92] V. Vondra, F. Wajer, J. Halámek, and D. van Ormondt. Influence of digital audio filters on image reconstruction in MRI. *Magnetic Resonance Materials in Biology, Phyics and Medicine*, 6:70–76, 1998.

[93] B. Madore, G. H. Glover, and N. J. Pelc. Unaliasing by Fourier-encoding the overlaps using the temporal dimension (UNFOLD), applied to cardiac imaging and fMRI. *Magn. Reson. Med.*, 42:813–828, 1999.

[94] C. A. McKenzie, E. N. Yeh, M. A. Ohliger, M. D. Price, and D. K. Sodickson. Self-calibrating parallel imaging with automatic coil sensitivity extraction. *Magn. Reson. Med.*, 47:529–538, 2002.

[95] M. R. Spiegel and J. Liu. *Mathematical handbook of formulas and tables*. Schaum's outline series. McGraw-Hill, New York, 1999.

ABSTRACT

Physics Based Iterative Reconstruction for MRI: Compensating and Estimating Field Inhomogeneity and T_2^* Relaxation

by

Bradley P. Sutton

Chairs: Jeffrey A. Fessler and Douglas C. Noll

Functional magnetic resonance imaging (fMRI) using the Blood-Oxygenation Level Dependent (BOLD) effect relies on microscopic susceptibility differences between oxygenated and deoxygenated blood to image functional organization in the brain. Higher magnetic field strengths and single-shot acquisitions give fMRI higher BOLD contrast and better temporal resolution, but these same parameters make the scans more sensitive to susceptibility-induced image distortions. Several noniterative image reconstruction methods are currently used to compensate for field inhomogeneities, but these methods assume that the field map that characterizes the off-resonance frequencies is spatially smooth, an assumption that is violated in areas near air/tissue interfaces in the brain. In this thesis, I develop an iterative, inverse problem approach to image reconstruction for MRI that takes into account field inhomogeneity and T_2^*-relaxation during the signal acquisition, receiver coil sensitivities, arbitrary k-space

trajectories, and within-voxel gradients in the field map. The iterative reconstruction is not limited by the smoothly-varying field map assumption and does not require the sample density compensation of the non-iterative methods for non-Cartesian trajectories. The iterative reconstruction was extended to simultaneously estimate the image, field map, and T_2^* map for quantitative fMRI experiments. Also, using undersampled k-space trajectories and multiple receiver coils, the iterative reconstruction was applied to SENSitivity Encoding (SENSE) experiments. In simulation, phantom, and human experiments, I compare the quality and accuracy of the field-corrected reconstructions using the iterative method versus the standard field-corrected method of conjugate phase. I also examine the stability of the iterative method for reconstructing time-series images from an fMRI study. I conclude that the iterative method results in stable image reconstructions for time series data and results in more accurate reconstructions when non-smooth field inhomogeneities are present. Using the joint estimation algorithm during a fMRI time series, respiration-induced phase variations and main field drift were accurately tracked and compensated. The increased accuracy of the jointly estimated field maps resulted in a larger number of activated voxels detected.